INAUGURAL - DISSERTATION

zur
Erlangung der Doktorwürde
der
Naturwissenschaftlich-Mathematischen
Gesamtfakultät
der
Ruprecht-Karls-Universität
Heidelberg

vorgelegt von
Dipl.-Phys. Andreas Wetscherek
geboren in Bayreuth

Tag der mündl. Prüfung: 10. Juli 2013

Magnetic Resonance Diffusion Weighted Imaging: Flow Compensated Intravoxel Incoherent Motion Imaging as a Tool to Probe Microvasculature

Gutachter: Prof. Dr. Uwe Oelfke
Prof. Dr. Lothar Rudi Schad

Diffusionsgewichtete Magnetresonanztomographie: Flusskompensierte Bildgebung der Inkohärenten Blutbewegung zur Untersuchung der Mikrogefäße. Um die charakteristische Zeitskala der inkohärenten Blutbewegung zu bestimmen, welche eine biexponentielle Abnahme des diffusionsgewichteten Signals verursacht, werden flusskompensierte und monopolare Diffusionsgradienten unterschiedlicher Dauer eingesetzt. Zu diesem Zweck wird eine Pulssequenz für die diffusionsgewichtete Magnetresonanztomographie entwickelt, welche es erlaubt, die Flusswichtung der Bildgebungsgradienten zu unterdrücken. Außerdem reduziert das Design der Sequenz den Einfluss zusätzlicher nichtlinearer Maxwellfelder. Die Sequenz wird am Phantom und am gesunden Probanden eingesetzt, wobei in Leber und Bauchspeicheldrüse unterschiedliche Signalverläufe für flusskompensierte und monopolare Diffusionswichtung gemessen werden, sowie eine Abhängigkeit von der Gesamtzeit des Diffusionsexperimentes festgestellt wird. Um die experimentell beobachteten Signalabschwächungen zu beschreiben, wird ein Modell entwickelt, welches es erlaubt, die durch die inkohärente Blutbewegung bedingte Signalabnahme für beliebige Diffusionsgradienten zu beschreiben. Basierend auf normalisierten Phasenverteilungen kann eine Anpassung der Modellparameter an die experimentellen Daten durchgeführt werden. Für die gemittelten Signalkurven der Probanden wird die charakteristische Zeitskala der inkohärenten Blutbewegung zu $\tau = 184 \pm 64$ ms für die Bauchspeicheldrüse und zu $\tau = 156 \pm 22$ ms für die Leber bestimmt. Um eine pixelweise Auswertung und die Erstellung von Karten der Modellparameter zu ermöglichen, wird eine auf der Hauptachsentransformation basierende Methode zur Rauschunterdrückung implementiert. Diese ermöglicht die Reduzierung des Einflusses von pseudo-zufälligen Signalstörungen, so dass höherwertige Parameterkarten basierend auf nur 33% der ursprünglich aufgenommenen Daten erstellt werden können.

Magnetic Resonance Diffusion Weighted Imaging: Flow Compensated Intravoxel Incoherent Motion Imaging as a Tool to Probe Microvasculature. Flow compensated and monopolar diffusion weighting gradients are employed to determine the characteristic time scale of the incoherent blood motion causing the biexponential signal decay. A pulse sequence for diffusion weighted magnetic resonance imaging is developed, which allows one to suppress velocity encoding of imaging gradients and which is designed such that the influence of concomitant fields is reduced. It is tested with phantoms and healthy volunteers, revealing different signal attenuation curves for flow compensated and monopolar diffusion gradients in liver and pancreas. Furthermore, a dependence on the total duration of the applied diffusion gradient profile is measured. To describe the experimentally observed signal attenuation curves, a model is developed, which allows one to calculate the signal attenuation due to incoherent blood motion for arbitrary diffusion gradient profiles. Precalculated normalized phase distributions allow one to fit the model to the experimental data. For the signal attenuation curves averaged over test subjects, the characteristic timescale of the blood motion is found to be $\tau = 184 \pm 64$ ms in pancreas and $\tau = 156 \pm 22$ ms in liver. To facilitate a pixel-wise evaluation and the creation of parameter maps, a denoising algorithm based on principal component analysis is implemented. The denoising reduces the effect of pseudo-random signal contributions allowing one to obtain parameter maps from only 33% of the originally acquired data, which are less affected by noise than the original ones.

Contents

1 Introduction

Magnetic resonance imaging (MRI) is a well established tool in medical diagnostics. Its high soft-tissue contrast and the benefits arising from the avoidance of the use of ionizing radiation have classically been the main supporting arguments. Nowadays it however becomes clear that its full potential can be unleashed by combining it with other imaging modalities, such as X-ray computed tomography (CT), position emission tomography (PET) and ultrasound. The field of MRI applications is very large, due to the fact that the precession of the nuclear spins is subject to a lot of different effects. By the use of accordingly tailored pulse sequences, it is not only possible to image morphology, but also functionality. While the use of contrast agents can reveal active tumors, it also enables investigation of perfusion by dynamic contrast-enhanced MRI. Exchange rates can be assessed with chemical exchange saturation transfer (CEST) imaging and the distribution of sodium can be imaged. At the time of writing, the most recently developed method is magnetic resonance fingerprinting [1], which simultaneously assesses a multitude of different properties to create a tissue fingerprint with many potential applications. Early indication of diseases is only one among them.

A parameter that is non-invasively only accessible by MRI is the diffusion of water molecules. Its main application area is the detection of ischemic regions caused by strokes, which was demonstrated first in 1990 [2]. While most research in the area of diffusion imaging targets the human brain, aiming to reconstruct orientation and connectivity of different bundles of nerve fibers from diffusion weighted MRI data, other application areas emerge as well. Whole-body diffusion weighted MRI has been found well suited to assess tumor infiltration in bone marrow for diagnose and therapy response [3] and can potentially supplement or even substitute an expensive whole-body PET/CT.

The work at hand was driven by recent findings, implying that intravoxel incoherent motion (IVIM) imaging [4,5] can be used for disease characterization in strongly perfused organs. By fitting a biexponential model to the diffusion weighted MRI data, it is possible to differentiate normal and cirrhotic liver tissue [6] and even distinguish pancreatitis from pancreatic carcinoma [7]. One of the parameters, namely the pseudo-diffusion coefficient D^*, which contains basically all the information on the incoherent motion, is however very delicate to measure.

The goal of this work is to develop methods to characterize the incoherent motion using diffusion weighted MRI. It particularly aims at measuring characteristic timescale and velocity of the incoherent blood motion. To this extent, development of pulse sequences for diffusion weighted MRI and of a microscopic model of the incoherent motion is

necessary. A secondary aim is to improve the reproducibility of IVIM measurements, in particular of measures similar to the D^* used in the biexponential model, which is a current research topic [8].

After a discussion of the fundamental principles of diffusion weighted MRI (chapter 2), details on the development of the used flow compensated pulse sequence are provided (chapter 3). Chapter 4 is devoted to describe the developed framework, which allows one to calculate the signal attenuation in the presence of incoherent motion for arbitrary diffusion gradient profiles. The experimental MRI data acquired using the flow compensated pulse sequence and the results from applying the developed framework are discussed in chapter 5. The results from applying a denoising algorithm based on principal component analysis to the MRI data to reduce the effects of pseudo-random signal contributions are shown in chapter 6, before the work is completed by a discussion (chapter 7).

2 Methods: Fundamentals of Diffusion Weighted MRI

After a short review of the fundamental physics (section 2.1) associated with the phenomenon of nuclear magnetic resonance (NMR), the basic techniques which enable magnetic resonance imaging (MRI) are presented (section 2.2). Subsequently the effects of diffusion on the MRI signal and how they enable measurement of the diffusion coefficient are discussed (section 2.3). While most of the content presented in this chapter is well known to the experienced researcher in the field of MRI, concomitant fields, which are discussed in section 2.2.4, can be neglected for most applications in MRI and a brushing-up of knowledge might prove helpful to follow the choice of discussed gradient profiles and their respective implementation into a MRI pulse sequence in chapters 3 and 4.

2.1 Nuclear Magnetic Resonance

This section starts with a discussion of properties of the total angular momentum of an atomic nucleus and its relation to the magnetic moment of the nucleus (section 2.1.1). It is shown how interaction between the latter and an external magnetic fields drives formation of a macroscopic magnetization (section 2.1.2). While being based on the quantum interactions of individual spins, basically all physics relevant for proton MRI can be treated in the thermodynamic limit by discussing classical magnetization vectors. The time evolution of those is governed by the Bloch equations, which are introduced in section 2.1.3 concluding the short overview on NMR.

2.1.1 Total Angular Momentum and Magnetic Moment

The total angular momentum $\boldsymbol{I}$ of an atomic nucleus is the sum of orbital and spin angular momentum of its fermionic components. Its relation to the magnetic moment $\boldsymbol{\mu}$ of the nucleus (eq. (2.1)) defines the gyromagnetic ratio γ, which is characteristic for each isotope.

$$\boldsymbol{\mu} = \gamma \boldsymbol{I} \tag{2.1}$$

While a variety of different isotopes found use in nuclear magnetic resonance imaging or spectroscopy, clinical MRI uses almost exclusively protons as nuclei for imaging, which is mainly due to their uncontestedly large natural abundance in biological tissue. The

gyromagnetic ratio of hydrogen ^{1}H is typically stated as $\frac{\gamma}{2\pi} = 42.576\ \frac{\text{MHz}}{\text{T}}$, values for other nuclei can be found in [9], p. 960.

In quantum mechanics the total angular momentum is described by the operator $\hat{\boldsymbol{I}} = \left(\hat{I}_x, \hat{I}_y, \hat{I}_z\right)$. It obeys the laws for angular momentum operators, in particular the commutation relation regarding its components given by eq. (2.2a), where $[\hat{A}, \hat{B}] = \hat{A}\hat{B} - \hat{B}\hat{A}$ defines the commutator of two quantum mechanic operators, $\hbar$ denotes the Planck constant divided by 2π, ε_{ijk} is the Levi-Civita symbol and $i, j, k \in \{x, y, z\}$. Eq. (2.2b) follows from the commutator's definition and eq. (2.2a).

$$\left[\hat{I}_i, \hat{I}_j\right] = i\hbar\varepsilon_{ijk}\hat{I}_k \tag{2.2a}$$

$$\left[\hat{\boldsymbol{I}}^2, \hat{I}_i\right] = 0 \tag{2.2b}$$

As a consequence of eq. (2.2b) the operators $\hat{\boldsymbol{I}}^2$ and $\hat{I}_z$ share a complete set of common eigenfunctions, the *spherical harmonics*. The eigenvalues for this common set of eigenfunction are given by eq. (2.3a) and (2.3b) and can be expressed with the quantum numbers I and m.

$$\hat{\boldsymbol{I}}^2 \mid I, m\rangle = \hbar^2 I(I+1) \mid I, m\rangle \tag{2.3a}$$

$$\hat{I}_z \mid I, m\rangle = \hbar m \mid I, m\rangle \tag{2.3b}$$

The *nuclear spin* I is characteristic for an isotope[1]. It is an integer for nuclei with even atomic mass number and a half-integer for odd mass numbers. In the ground state of a nucleus with both even number of proton and even number of neutrons, the nuclear spin vanishes ($I = 0$). Therefore the carbon and oxygen isotopes ^{12}C and ^{16}O cannot be used for MRI. As will be shown in the next section, a nuclear spin in an external magnetic field can occupy $2I + 1$ different energy states characterized by the magnetic quantum number m, which can take the values $-I, -I+1, \ldots, I$.

2.1.2 Influence of External Magnetic Fields

The interaction between an external magnetic field $\boldsymbol{B}$ and a magnetic moment $\boldsymbol{\mu}$ is described by the Hamiltonian $\hat{H}$ given by eq. (2.4).

$$\hat{H} = -\boldsymbol{\mu} \cdot \boldsymbol{B} \tag{2.4}$$

For a nucleus in a stationary magnetic field of strength B_0, the orientation of which can without loss of generality be chosen to be the z-axis ($\boldsymbol{B} = (0, 0, B_0)$), the Hamiltonian simplifies with the help of eq. (2.1) to $\hat{H} = -\gamma\hat{I}_z B_0$. The common eigenfunctions of $\hat{\boldsymbol{I}}^2$ and $\hat{I}_z$, given by eq. (2.3a) and (2.3b), are thus simultaneous eigenfunctions of $\hat{H}$.

[1] It can however differ for nuclear isomers in metastable states as a result of nuclear reactions

This allows one to calculate the energy levels E_m of the system, which are given by the solutions of the time-independent Schrödinger equation (2.5a) and are found to be linear in m (eq. (2.5b)).

$$\hat{H} \mid I, m\rangle = E_m \mid I, m\rangle \tag{2.5a}$$

$$E_m = -\gamma\hbar m B_0 \tag{2.5b}$$

The energy difference between the states is given by $\Delta E = \hbar\omega_0$, where the Larmor frequency ω_0 was introduced. ω_0 is directly proportional to the strength B_0 of the applied magnetic field (eq. (2.6)).

$$\omega_0 = \gamma B_0 \tag{2.6}$$

The existence of different energy states in the presence of an external magnetic field accounts for different occupation probabilities p_m, which are in thermal equilibrium determined by the Boltzmann distribution. The fraction of spins occupying a state with quantum number m is given by eq. (2.7), where $Z(T)$ denotes the partition function and T the temperature. For $|B_0| > 0$ the states are not degenerated, thus $Z(T) = \sum_{m=-I}^{I} \mathrm{e}^{\frac{\hbar m\omega_0}{kT}}$.

$$\frac{N_m}{N} = \frac{\mathrm{e}^{\frac{\hbar m\omega_0}{kT}}}{Z(T)} \tag{2.7}$$

The relative difference in occupation of the two energy levels in case of hydrogen ^{1}H ($I = \frac{1}{2}$) evaluates at $T = 310$ K (body temperature) for $B_0 = 1.5$ T to $\frac{\Delta N}{N} = \tanh(\frac{\gamma\hbar B_0}{2kT}) = 4.94 \cdot 10^{-6}$. This value appears to be small, but due to the large number of atoms, a measurable macroscopic magnetization $\boldsymbol{M}$ builds up according to eq. (2.8).

$$\boldsymbol{M} = \frac{1}{V}\sum_{k=1}^{N} \langle \hat{\boldsymbol{\mu}}_{\boldsymbol{k}} \rangle = \frac{\gamma}{V}\sum_{k=1}^{N} \left\langle \hat{\boldsymbol{I}}_{\boldsymbol{k}} \right\rangle \tag{2.8}$$

The magnetization in the equilibrium state is aligned with the external magnetic field ($\boldsymbol{B} = (0, 0, B_0)$), since the eigenstates of $\hat{I}_x$ and $\hat{I}_y$ are degenerated and thus occupied equally. Its magnitude is given by eq. (2.9), where in the last step the high-temperature approximation $\mathrm{e}^{\frac{\hbar m\omega_0}{kT}} \approx 1 + \frac{\hbar m\omega_0}{kT}$ was used ($\hbar\omega_0 \ll kT$).

$$M_0 = \frac{\gamma}{V}\sum_{k=1}^{N} \left\langle \hat{I}_z \right\rangle = \frac{\gamma\hbar N}{VZ(T)} \sum_{m=-I}^{I} m\mathrm{e}^{\frac{\hbar m\omega_0}{kT}} \approx \frac{N}{V}\frac{\gamma^2\hbar^2 I(I+1)B_0}{3kT} \tag{2.9}$$

While in the following section the time-evolution of $\boldsymbol{M}$ is derived in the formalism of quantum mechanics, it should be noted that in *proton* (^{1}H) MRI, most applications only need to take into account the macroscopic picture, which is described by the Bloch equations.

2.1.3 Bloch Equations

According to the Ehrenfest theorem, the time-evolution of the magnetization $\hat{\boldsymbol{\mu}}$ is given by eq. (2.10), since $\hat{\boldsymbol{\mu}}$ is not an explicit function of t ($\frac{\partial \hat{\boldsymbol{\mu}}}{\partial t} = 0$).

$$\frac{\mathrm{d}\hat{\boldsymbol{\mu}}}{\mathrm{d}t} = \left\langle \frac{i}{\hbar}\left[\hat{H}, \hat{\boldsymbol{\mu}}\right] \right\rangle = \frac{i\gamma^2}{\hbar}\left\langle \hat{\boldsymbol{I}}(\hat{\boldsymbol{I}}\cdot\boldsymbol{B}) - (\hat{\boldsymbol{I}}\cdot\boldsymbol{B})\hat{\boldsymbol{I}} \right\rangle \tag{2.10}$$

Using Einstein notation, the expression in brackets can be evaluated component-wise, yielding a cross product (eq. 2.11).

$$\hat{I}_k\hat{I}_l B_l - \hat{I}_l B_l \hat{I}_k = B_l(\hat{I}_k\hat{I}_l - \hat{I}_l\hat{I}_k) = B_l\left[\hat{I}_k, \hat{I}_l\right] = i\hbar B_l \hat{I}_m \varepsilon_{klm} = i\hbar\left(\boldsymbol{B}\times\hat{\boldsymbol{I}}\right)_k \tag{2.11}$$

The time-evolution of the macroscopic magnetization can thus be obtained by summation (eq. (2.12)).

$$\frac{\mathrm{d}\boldsymbol{M}}{\mathrm{d}t} = \frac{1}{V}\sum_{k=1}^{N}\left\langle \frac{\mathrm{d}\hat{\boldsymbol{\mu}}_{\boldsymbol{k}}}{\mathrm{d}t} \right\rangle = \frac{\gamma}{V}\sum_{k=1}^{N}\langle\hat{\boldsymbol{\mu}}_{\boldsymbol{k}}\rangle \times \boldsymbol{B} = \gamma\boldsymbol{M}\times\boldsymbol{B} \tag{2.12}$$

Empirically, Bloch found similar equations [10] for a magnetic field along the z-axis, which are given in eq. (2.13a) - (2.13c).

$$\frac{\mathrm{d}M_x(t)}{\mathrm{d}t} = \gamma\left(\boldsymbol{M}(t)\times\boldsymbol{B}(t)\right)_x - \frac{M_x(t)}{T_2} \tag{2.13a}$$

$$\frac{\mathrm{d}M_y(t)}{\mathrm{d}t} = \gamma\left(\boldsymbol{M}(t)\times\boldsymbol{B}(t)\right)_y - \frac{M_y(t)}{T_2} \tag{2.13b}$$

$$\frac{\mathrm{d}M_z(t)}{\mathrm{d}t} = \gamma\left(\boldsymbol{M}(t)\times\boldsymbol{B}(t)\right)_x - \frac{M_z(t)-M_0}{T_1} \tag{2.13c}$$

In the following the solutions of the Bloch equations for two relevant cases are discussed.

Free induction decay (FID) If the magnetic field $\boldsymbol{B} = (0, 0, B_0)$ is static, the solution of the Bloch equations are given by eq. (2.14a) and (2.14b), where the transversal magnetization $M_{xy} = M_x + iM_y$ was introduced. Since the measured MRI signal is found proportional to M_{xy}, the time evolution of the magnetization in case of a static magnetic field bears the name *free induction decay* referring to eq. (2.14b).

$$M_z(t) = M_0 - (M_0 - M_z(0))\ \mathrm{e}^{-\frac{t}{T_1}} \tag{2.14a}$$

$$M_{xy}(t) = M_{xy}(0)\ \mathrm{e}^{i\omega_0 t}\mathrm{e}^{-\frac{t}{T_2}} \tag{2.14b}$$

The return of the *longitudinal* magnetization M_z to its equilibrium value is determined by the *spin-lattice-relaxation time* T_1. Movements due to thermal energy of the molecules cause fluctuating magnetic fields with spectral components at the frequency ω_0. This

induces transitions between the energy levels, allowing the magnetization to return to its equilibrium state.

The time evolution of the transversal magnetization is governed by the *spin-spin-relaxation time* T_2. Fluctuating magnetic fields (causing fluctuations in ω_0) originating from dipole-dipole interactions lead to an irreversible dephasing of the magnetization. Further dephasing, leading to an increased signal decay, which is described by the time constant T_2', is caused by inhomogeneities of the magnetic field and local variations in susceptibility resulting in pertubating magnetic fields B_P. Those additional dephasing can however be compensated for in MRI using refocusing pulses (introduced in section 2.2.3) exploiting that the additional fields B_P are time-independent. The overall decay of the transversal magnetization can thus be described by the time constant T_2^*, given by eq. (2.15).

$$\frac{1}{T_2^*} = \frac{1}{T_2} + \frac{1}{T_2'} \tag{2.15}$$

Magnetic Resonance Now the following case is considered: In addition to the static magnetic field a circular polarized radio-frequency field $\boldsymbol{B_1}(t)$ of frequency ω_1, given by eq. (2.16) is applied.

$$\boldsymbol{B_1}(t) = (B_1(t)\cos(\omega_1 t), -B_1(t)\sin(\omega_1 t), 0) \tag{2.16}$$

It is further assumed that the time during which $\boldsymbol{B_1}(t)$ is active is short such that magnetization decay can be neglected ($T_1, T_2 \to \infty$). To solve the Bloch equations, the system is viewed in the rotating coordinate frame, $\boldsymbol{x'} = \boldsymbol{R_z^T}(\omega_1 t)\boldsymbol{x}$, where $\boldsymbol{R_z}(\theta)$ is the matrix performing a counter-clockwise rotation by an angle θ around the z-axis and is given by eq. (2.17).

$$\boldsymbol{R_z}(\theta) = \begin{pmatrix} \cos\theta & \sin\theta & 0 \\ -\sin\theta & \cos\theta & 0 \\ 0 & 0 & 1 \end{pmatrix} \tag{2.17}$$

The time evolution of the magnetization $\boldsymbol{M'}$ in the rotating reference frame is thus given by eq. (2.18).

$$\begin{aligned} \frac{\mathrm{d}\boldsymbol{M'}(t)}{\mathrm{d}t} &= \boldsymbol{R_z^T}(\omega_1 t)\frac{\mathrm{d}\boldsymbol{M}(t)}{\mathrm{d}t} + \frac{\mathrm{d}\boldsymbol{R_z^T}(\omega_1 t)}{\mathrm{d}t}\boldsymbol{M}(t) \\ &= \gamma\left(\boldsymbol{R_z^T}(\omega_1 t)\underline{\underline{\boldsymbol{B}}}(t)\boldsymbol{R_z}(\omega_1 t) + \frac{1}{\gamma}\frac{\mathrm{d}\boldsymbol{R_z^T}(\omega_1 t)}{\mathrm{d}t}\boldsymbol{R_z}(\omega_1 t)\right)\boldsymbol{M'}(t) \end{aligned} \tag{2.18}$$

The symbol $\underline{\underline{\boldsymbol{B}}}$ denotes the matrix representation of the cross product with $\boldsymbol{B}$ and is given in eq. (2.19a). Similarly the expression in parenthesis in eq. (2.18) describes the cross product with the magnetic field effective in the rotating reference frame $\boldsymbol{B_{\mathrm{eff}}}$,

which evaluates to eq. (2.19b).

$$\underline{\underline{\boldsymbol{B}}}(t) = \begin{pmatrix} 0 & B_0 & B_1(t)\sin(\omega_1 t) \\ -B_0 & 0 & B_1(t)\cos(\omega_1 t) \\ -B_1(t)\sin(\omega_1 t) & -B_1(t)\cos(\omega_1 t) & 0 \end{pmatrix} \tag{2.19a}$$

$$\underline{\underline{\boldsymbol{B}_{\mathbf{eff}}}}(t) = \begin{pmatrix} 0 & B_0 - \frac{\omega_1}{\gamma} & 0 \\ -B_0 + \frac{\omega_1}{\gamma} & 0 & B_1(t) \\ 0 & -B_1(t) & 0 \end{pmatrix} \tag{2.19b}$$

The time evolution of the magnetization in the rotating frame of reference can thus be expressed by a cross product with an effective magnetic field $\boldsymbol{B}_{\mathbf{eff}}(t) = (B_1(t), 0, B_0 - \frac{\omega_1}{\gamma})$. If the difference between the Larmor frequency and the frequency of the applied radio frequency field is denoted by $\Delta\omega = \gamma B_0 - \omega_1$, the time evolution of the different components of $\boldsymbol{M'}$ is given by eq. (2.20a) - eq.(2.20c).

$$\frac{\mathrm{d}M'_x(t)}{\mathrm{d}t} = M'_y(t)\Delta\omega \tag{2.20a}$$

$$\frac{\mathrm{d}M'_y(t)}{\mathrm{d}t} = \gamma M'_z(t)B_1(t) - M'_x(t)\Delta\omega \tag{2.20b}$$

$$\frac{\mathrm{d}M'_z(t)}{\mathrm{d}t} = -\gamma M'_x(t)B_1(t) \tag{2.20c}$$

If the resonance condition $\omega_0 = \omega_1$ is met, the magnetization starts precessing around the x'-axis. Assuming that the magnetization was initially in the equilibrium state, when the radio frequency field was switched on, the time-dependence of the so called *flip angle* α between $\boldsymbol{M'}$ and the z'-axis is given by eq. (2.21).

$$\alpha(t) = \gamma \int_0^t B_1(t')\mathrm{d}t' \tag{2.21}$$

This effect is used in magnetic resonance imaging to create a transversal magnetization component. For off-resonance spins, the time-evolution of the transversal magnetization is described by (2.22a), which has (assuming $M'_z(t)$ is known and $M'_{xy}(0) = 0$) the solution given by eq. (2.22b) [11].

$$\frac{\mathrm{d}M'_{xy}(t)}{\mathrm{d}t} = i\gamma {M'}_z(t)B_1(t) - i\Delta\omega {M'}_{xy}(t) \tag{2.22a}$$

$$M'_{xy}(t) = i\gamma \mathrm{e}^{-i\Delta\omega t} \int_0^t M'_z(t')B_1(t')\mathrm{e}^{i\Delta\omega t'}\mathrm{d}t' \tag{2.22b}$$

$$\tag{2.22c}$$

In case of small flip angles the longitudinal magnetization remains approximately in its equilibrium state and the off-resonance flip angle $\alpha(\Delta\omega)$ can be approximated by the

Fourier transform of the envelope function $B_1(t)$ of the radio frequency field (eq. (2.23)).

$$|\alpha(\Delta\omega)| \approx |\sin(\alpha(\Delta\omega))| = \frac{|M'_{xy}(t,\Delta\omega)|}{M_0} \approx \gamma \left| \int_0^t B_1(t') \mathrm{e}^{i\Delta\omega t'} \mathrm{d}t' \right| \tag{2.23}$$

With the fundamental principles behind the phenomenon of nuclear magnetic resonance being discussed, the following section will focus on how those can be put to use to spatially resolve the distribution of nuclear spins and create a magnetic resonance image.

2.2 Magnetic Resonance Imaging

This section is structured as follows. First it is shown how the magnetization is related to the signal picked up by receive coils and how magnetic field gradients can be used to encode locations via spectral wave vectors (section 2.2.1). Then the concept of k-space and techniques to acquire the required data for reconstructing an MRI image are discussed (section 2.2.2). After explaining how the magnetization can be selectively excited and refocused (section 2.2.3), a short comment on the existence of concomitant fields, which inevitably accompany linear magnetic field gradients, is made (section 2.2.4).

2.2.1 Gradient and Receive Coils

Gradient coils are an essential hardware component in a MRI system, that allow one to overlay the static magnetic field $\boldsymbol{B} = (0, 0, B_0)$ with a spatially dependent magnetic field. Typically a set of several coils is used, which allows one to create a linear gradient field[2] along the z-axis, which is characterized by the magnetic field gradient $\boldsymbol{g}$ specified in eq. (2.24).

$$\boldsymbol{g} = \nabla B_z = \left(\frac{\partial B_z}{\partial x}, \frac{\partial B_z}{\partial y}, \frac{\partial B_z}{\partial z} \right) \tag{2.24}$$

The change in the total magnetic field strength, which is caused by the gradient field, leads to a spatial dependence of the Larmor frequency given by eq. (2.25).

$$\omega(\boldsymbol{x}) = \gamma B_z(\boldsymbol{x}) = \gamma B_0 + \gamma \boldsymbol{x} \cdot \boldsymbol{g} \tag{2.25}$$

Since the relative change in the total magnetic field strength due to an applied gradient field is rather small (typically $< 1\%$), the equilibrium magnetization can be assumed constant and thus the time-evolution of the longitudinal component of the magnetization is unaffected by the gradient field. The transversal magnetization M'_{xy} measured in the rotating reference frame does however accumulate a spatially dependent phase $\phi'(\boldsymbol{x}, t)$ due to the difference in Larmor frequency in the presence of a magnetic field gradient

[2] The existence of such gradient fields does however not comply with Maxwell's equations, which leads to the formation of concomitant fields (for details see section 2.2.4).

(eq. (2.26a) and (2.26b)). Magnetization decay due to T_2-relaxation is neglected in eq. (2.26a).

$$M'_{xy}(\boldsymbol{x}, t) = M'_{xy}(\boldsymbol{x}, 0)\mathrm{e}^{-i\phi'(\boldsymbol{x},t)} \tag{2.26a}$$

$$\phi'(\boldsymbol{x}, t) = \gamma \boldsymbol{x} \cdot \int_0^t \boldsymbol{g}(t')\mathrm{d}t' \tag{2.26b}$$

Note that the spatial coordinates $\boldsymbol{x}$ used in the remainder of this chapter always refers to the location in the laboratory frame even if complex properties measured at those locations are given in the frame of reference rotating with ω_0 (denoted by the prime $'$).

Receive Coils are another important component of an MRI system picking up the signal which is induced by the precessing magnetization. According to Haacke *et al.* [12], p. 101, the signal $S(t)$ which is induced in the coil is given by eq. (2.27), where $\phi(\boldsymbol{x}, t)$ denotes the phase of the transversal magnetization in the laboratory frame and $\phi_B(\boldsymbol{x})$ is the phase of the transverse component B_{xy} of the receive coil B_1 field, both phases measured with respect to the x-axis.

$$S(t) \propto \int_V |M_{xy}(\boldsymbol{x}, t)|\,|B_{xy}(\boldsymbol{x}, t)| \sin\left(\phi(\boldsymbol{x}, t) - \phi_B(\boldsymbol{x})\right) \mathrm{d}^3\boldsymbol{x} \tag{2.27}$$

Following [9], p. 370ff., the frequency offset caused by Lamor precession is removed by the MRI receiver resulting in a demodulated signal $S'(t)$, which is the signal that would be measured in the rotating reference frame. A quadrature detection is further performed, allowing to obtain the complex signal $S'_{xy}(t)$ from the real valued signal $S'(t)$. $S'_{xy}(t)$ can be expressed by the transversal magnetization M'_{xy} and the transversal component B'_{xy} of the B_1 field in the rotating reference frame. Assuming the receive coil is tuned to the Larmor frequency, $B'_{xy}(\boldsymbol{x})$ doesn't change with time and $S'_{xy}(t)$ is given by eq. (2.28).

$$S'_{xy}(t) \propto \int_V M'_{xy}(\boldsymbol{x}, t) B'_{xy}(\boldsymbol{x}) \mathrm{d}^3\boldsymbol{x} \tag{2.28}$$

Recalling the time evolution of the transversal magnetization in the presence of a magnetic field gradient (eq. (2.26a)) and using the definition of the wave vector $\boldsymbol{k}(t)$ given by eq. (2.29a), eq. (2.29b) is obtained.

$$\boldsymbol{k}(t) = \frac{1}{2\pi}\nabla\phi'(\boldsymbol{x}, t) = \frac{\gamma}{2\pi}\int_0^t \boldsymbol{g}(t')\mathrm{d}t' \tag{2.29a}$$

$$S'_{xy}(\boldsymbol{k}(t)) \propto \int_V M'_{xy}(\boldsymbol{x}, 0) B'_{xy}(\boldsymbol{x}) \mathrm{e}^{-2\pi i \boldsymbol{k}(t)\cdot\boldsymbol{x}} \mathrm{d}^3\boldsymbol{x} \tag{2.29b}$$

The signal obtained after demodulation and quadrature detection is thus equivalent to the Fourier transform of the weighted magnetization $M'_B(\boldsymbol{x}) = M'_{xy}(\boldsymbol{x}, 0)B'_{xy}(\boldsymbol{x})$. Also note that S'_{xy} is a function of the spatial wave vector $\boldsymbol{k}$ and only implicitly dependent on

time, if a magnetic field gradient is active while the signal is measured. The sensitivity profile $B'_{xy}(\boldsymbol{x})$ of the receive coil (magnitude and phase) is typically known or can be measured. The spatially resolved transverse magnetization without applied magnetic field gradients $M'_{xy}(\boldsymbol{x}) = M'_{xy}(\boldsymbol{x}, 0)$ can thus be directly obtained from $M'_B(\boldsymbol{x})$ after an inverse Fourier transform of $S'_{xy}(t)$ along the domain of spatial frequencies is performed (eq. 2.30).

$$M'_{xy}(\boldsymbol{x}) \propto \frac{1}{B'_{xy}(\boldsymbol{x})} \int_{V_{\boldsymbol{k}}} S'_{xy}(\boldsymbol{k}) \mathrm{e}^{2\pi i \boldsymbol{k}\cdot\boldsymbol{x}} \mathrm{d}^3\boldsymbol{k} \tag{2.30}$$

Having derived this equation, the following section will be devoted to techniques that allow sampling of $S'_{xy}(\boldsymbol{k})$ such that an image of the desired property $M'_{xy}(\boldsymbol{x})$ can be obtained.

2.2.2 Frequency and phase encoding to sample k-space

Since digital signal processing only allows for discrete sampling, $S'_{xy}(\boldsymbol{k})$ can only be measured at a finite number of distinct $\boldsymbol{k}$. While in principle all three spatial dimensions could be encoded with the help of spatial frequencies $\boldsymbol{k}$, the MRI sequences used in this work apply selective slice excitation (see section 2.2.3) to achieve spatial resolution along the z-axis. Since the discrete Fourier transform can be readily performed for equidistantly sampled signals, a typical fully sampled two-dimensional k-space would consist of $S'_{xy}(k_x, k_y)$ measured for the distinct points in k-space depicted in Fig. 2.1. If we assume a two-dimensional field of view with dimensions FoV_x and FoV_y the application of a magnetic field gradient of magnitude g along the respective axis would cause a spread in Larmor frequency by $\pm\Delta\omega$ with respect to the Larmor frequency at the center of the field of view, where $\Delta\omega$ is given by eq. (2.31).

$$\Delta\omega = \gamma g \frac{\mathrm{FoV}}{2} \tag{2.31}$$

The change of the spatial frequency Δk inherent to the application of a gradient g is linked to the application time Δt of the gradient via eq. (2.32), which is a special case of eq. (2.29a).

$$\Delta k = \frac{\gamma}{2\pi} g \Delta t \tag{2.32}$$

This allows us to use the Shannon-Nyquist sampling theorem [13], which is given by eq. (2.33a) to derive the k-space sampling theorems given by eq. (2.33b) and (2.33c). $\Delta x = \frac{\mathrm{FoV}}{N}$ is the spatial resolution, if the size of the image matrix is N points along the respective axis. The highest sampled spatial frequency $k_{\max}$ is given for a symmetric

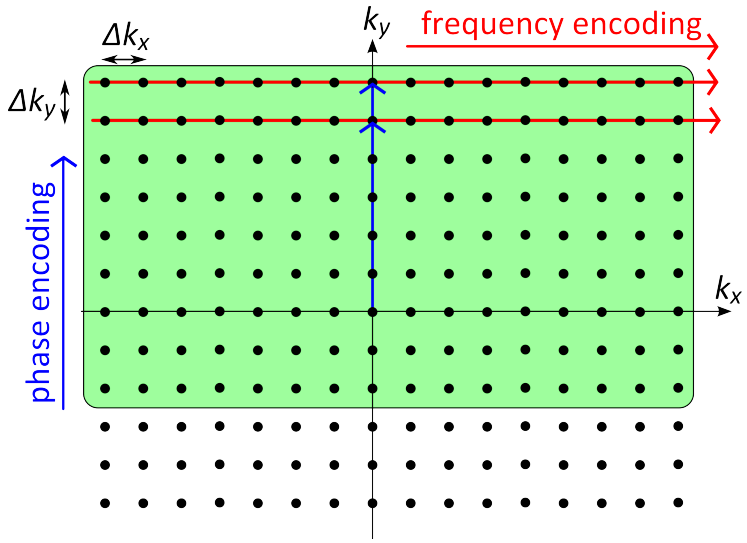

Figure 2.1: Typical sampling of k-space in 2D. While k_y is encoded into the phase of the magnetization, frequency encoding is used to encode k_x. By using symmetry of $S(\boldsymbol{k})$ the necessary sampling points can be reduced. The partial Fourier factor specifies the acquired fraction which is for PF $= 0.75$ depicted by the green rectangle.

sampling of k-space by $k_{\max} = \frac{N\Delta k}{2}$.

$$\Delta t \leq \frac{1}{2\Delta\nu} = \frac{\pi}{\Delta\omega} \tag{2.33a}$$

$$\Delta k \leq \frac{1}{\mathrm{FoV}} \tag{2.33b}$$

$$k_{\max} \geq \frac{1}{2\Delta x} \tag{2.33c}$$

The structure of k-space, respectively the points at which S'_{xy} needs to be measured, is thus determined by the field of view and the desired spatial resolution Δx. Two generally remarks are made before sampling of k-space using frequency and phase encoding is discussed.

Partial Fourier From eq. (2.29b) the symmetry property of k-space given by eq. (2.34) becomes apparent, where the star * denotes the complex conjugate.

$$S'_{xy}(-\boldsymbol{k}) = S'^{*}_{xy}(\boldsymbol{k}) \tag{2.34}$$

Due to the fact that $S'_{xy}(-\boldsymbol{k})$ is a complex quantity, sampling of full k-space yields redundant information and using the symmetry stated in eq. (2.34), only half of the k-space data points need to be acquired. Due to constraints inflicted by signal-to-noise ratio

and phase stability, it however is often desired to acquire some redundant information. The partial Fourier factor gives the sampled fraction of k-space, which is depicted for the value 0.75 in Fig. 2.1 by the green rectangle.

Sampling of k-space center For phase correction and since the signal energy is highest in the k-space center, it is desirable to acquire S'_{xy} at the point $k_x = k_y = 0$, resulting in an asymmetric sampling scheme similar to the one shown in Fig. (2.1) for even N.

Phase encoding One of the strategies to encode $\boldsymbol{k}$ into the magnetization is to apply a magnetic field gradient before the signal acquisition. This way the location of a spin packet is encoded into the phase difference to the rotating reference frame due to the different precession frequency during the magnetic field gradient. This technique however entails the problem of *aliasing*. If objects lie outside the field of view along the direction in which phase encoding gradients are applied, they are associated with higher frequencies, that cannot be resolved due to the Nyquist criterion and fold over artifacts are the result. Therefore phase encoding is typically chosen along the shortest dimension of the imaged subject, to be able to include the entire subject into the field of view.

Frequency encoding Another possibility is the application of a magnetic field gradient during the measurement of the signal. The location of the spin packets is thus encoded into the precession frequency during the acquisition process. If the signal is sampled while a gradient is active, the $\boldsymbol{k}$ value accumulates with time and a line in k-space is sampled as depicted in Fig. 2.1. The discretization of the signal is achieved by measuring the signal integrated over the dwell time t_{dwell}. Typically, oversampling is performed along the acquired line, where the dwell time is specified by the oversampling factor β and the so called bandwidth per pixel $\frac{\text{BW}}{\text{px}}$ via eq. (2.35a). $\frac{\text{BW}}{\text{px}}$ is related to the full bandwidth $2\Delta\nu$ by eq. (2.35b), which also determines the necessary amplitude of the *readout gradient*.

$$t_{\text{dwell}} = \frac{1}{\beta N \frac{\text{BW}}{\text{px}}} \tag{2.35a}$$

$$\frac{\text{BW}}{\text{px}} = \frac{2\Delta\nu}{\beta N} = g\,\frac{\gamma \text{FoV}}{2\pi\beta N} \tag{2.35b}$$

According to [9], p. 370, frequency encoding allows the use of an anti-aliasing filter prior to sampling, such that wide-band noise or higher frequency components from outside the specified field of view do not cause image artifacts. Frequency encoding can thus be used along a direction in which not the whole subject can be included into the field of view.

2.2.3 Selective Slice Excitation

Another possibility to spatially resolve the MRI signal is the selective excitation of e.g. only a slice of thickness Δz. This can be achieved by applying a slice selection gradient of amplitude g_s while the radio frequency pulse is active. This causes a dispersion $\Delta\omega$ of the precession frequencies along the axis of the applied gradient given by eq. (2.36a). Recalling the derived frequency dependence of the flip angle (eq. (2.23)), which is restated below (eq. (2.36b)), it becomes apparent that if $B_1(t)$ could be chosen such that its Fourier transform would correspond to a rectangular profile of width $\Delta\omega$, only the magnetization in the slice of thickness Δz would be excited.

$$\Delta\omega = \gamma g_s \Delta z \tag{2.36a}$$

$$|\alpha(\Delta\omega)| \approx |\sin(\alpha(\Delta\omega))| = \frac{|M'_{xy}(t,\Delta\omega)|}{M_0} \approx \gamma \left| \int_0^t B_1(t') \mathrm{e}^{i\Delta\omega t'} \mathrm{d}t' \right| \tag{2.36b}$$

According to [9], p. 39ff., an envelope function $B_1(t)$, the Fourier transform of which would yield the desired profile, is given by eq. (2.37a), where A is the amplitude, which can be varied independently of the temporal profile. Since the radio frequency pulse can however only be applied for a finite duration, Hamming ($\alpha = 0.46$) and Hanning ($\alpha = 0.5$) apodization windows are used to suppress ringing effects in the flip angle profile. The resulting pulse shapes are described by eq. (2.37b), where $N = \max(N_\mathrm{L}, N_\mathrm{R})$ is the larger number of zero-crossings left N_L and right N_R to the central peak.

$$B_1(t) = A \, \frac{\sin\left(t\frac{\Delta\omega}{2}\right)}{t\frac{\Delta\omega}{2}} \tag{2.37a}$$

$$B_1(t) = A \, \frac{\sin\left(t\frac{\Delta\omega}{2}\right)}{t\frac{\Delta\omega}{2}} \left[(1-\alpha) + \alpha\cos\left(t\frac{\Delta\omega}{2N}\right)\right] \tag{2.37b}$$

The number of zero-crossings for a sinc-pulse is determined by the total duration T of the pulse and a property called time-bandwidth product (TBP), which corresponds to the number of zero-crossings (eq. (2.38)).

$$\mathrm{TBP} = \frac{T\Delta\omega}{2\pi} = N_\mathrm{L} + N_\mathrm{R} \tag{2.38}$$

Due to the application of a magnetic field gradient, a phase dispersion is encoded into the magnetization, corresponding to the spatial wave vector k_s. The exact amount of k_s that needs to be compensated for using a rephasing gradient subsequently to the refocusing pulse, is dependent on the timing of the slice selection gradient and the isodelay t_I of the excitation pulse by eq. (2.39), where r is the time after the application of the pulse in which the gradient is still active (*ramp down time*).

$$k_s = \frac{\gamma}{2\pi} \int_{T-t_I}^{T+r} g_s(t)\mathrm{d}t \tag{2.39}$$

While for the pulses used in this work, the isodelay point is well approximated by the center of the pulse, thus $t_I = \frac{T}{2}$, this is not true in general [9], p. 76f.

Refocusing pulses Sinc pulses are typically used to excite the magnetization out of the equilibrium state by a flip angle $\alpha \leq 90°$. The approximation made to derive eq. (2.36b), namely $M_z'(t') \approx M_0$, is only valid for small flip angles and the effects arising from the non-linearity of the Bloch equations become too large for flip angles $> 90°$. While sinc pulses with some adjustments can be used for flip angles of $\alpha = 180°$ [9], p. 42, those are typically realized by Shinnar-Le Roux (SLR) pulses [14,15]. In this work 180° pulses are used for refocusing and eliminating the $T2'$-decay due to magnetic field inhomogeneities. A 180°-pulse applied at time $\frac{\mathrm{TE}}{2}$ to flip the magnetization along an axis in the $x'y'$-plane causes an inversion of the relative phase differences caused by the perturbation field B_P. Assuming that those inhomogeneities are not time-dependent, between $\frac{\mathrm{TE}}{2}$ and the *echo time* TE, the same relative phase differences are acquired and are canceling out the ones acquired before the 180° pulse. Formation of a *spin echo* is the result [16].

2.2.4 Concomitant Fields

In this section it will be shown following [9], p. 293ff., that a linear magnetic field gradient of B_z, as desired for MRI, cannot exist alone, but is accompanied by additional gradients of B_x and B_y, which are not always negligible. According to Maxwell's equations [17], a magnetic field $\boldsymbol{B}$ must satisfy Gauß's law for magnetism (2.40a) and Ampère's law (2.40b), where μ_0 and ε_0 denote vacuum permeability and permittivity.

$$\nabla \cdot \boldsymbol{B} = 0 \tag{2.40a}$$

$$\nabla \times \boldsymbol{B} = \mu_0 \boldsymbol{J} + \mu_0 \varepsilon_0 \frac{\partial \boldsymbol{E}}{\partial t} \tag{2.40b}$$

If the current densities in eq. (2.40b) are negligible and we keep the notation of $\boldsymbol{g} = \nabla B_z$ from section 2.2.1 we get the dependencies of the partial derivatives of the components of the magnetic field $\boldsymbol{B}$ given by eq. (2.41a) - (2.41e), where the transverse gradient term $g_\perp$, defined by eq. (2.41a) and the symmetry parameter α_s, defined by eq. (2.41d)

are introduced.

$$g_\perp = \frac{\partial B_x}{\partial y} = \frac{\partial B_y}{\partial x} \tag{2.41a}$$

$$g_x = \frac{\partial B_z}{\partial x} = \frac{\partial B_x}{\partial z} \tag{2.41b}$$

$$g_y = \frac{\partial B_z}{\partial y} = \frac{\partial B_y}{\partial z} \tag{2.41c}$$

$$\alpha_s g_z = \alpha_s \left(\frac{\partial B_z}{\partial z}\right) = -\frac{\partial B_x}{\partial x} \tag{2.41d}$$

$$(1-\alpha_s) g_z = (1-\alpha_s) \left(\frac{\partial B_z}{\partial z}\right) = -\frac{\partial B_y}{\partial y} \tag{2.41e}$$

Neglecting higher order terms, the components of the magnetic field are thus given by eq. (2.42).

$$\begin{pmatrix} B_x \\ B_y \\ B_z - B_0 \end{pmatrix} = \begin{pmatrix} -\alpha_s g_z & g_\perp & g_x \\ g_\perp & (\alpha_s - 1) g_z & g_y \\ g_x & g_y & g_z \end{pmatrix} \begin{pmatrix} x \\ y \\ z \end{pmatrix} \tag{2.42}$$

This equation implies that even if $\boldsymbol{g}$ and $\boldsymbol{B_0}$ are applied along the z-axis, there are still non-zero components B_x and B_y possible. The total amplitude of the magnetic field, which determines the Larmor frequency, is thus given by eq. (2.43a). The additional concomitant field B_c can be identified by a Taylor expansion of eq. (2.43a) to the second order as performed in [18]. For typically used cylindrical gradient coils $g_\perp \approx 0$ and $\alpha_s \approx 0.5$ hold and a relatively simple expression for B_c can be derived (eq. 2.43b).

$$B(x,y,z) = \sqrt{B_x^2 + B_y^2 + B_z^2} = B_0 + x g_x + y g_y + z g_z + B_c(x,y,z) \tag{2.43a}$$

$$B_c(x,y,z) \approx \frac{1}{2B_0} \left[\left(z g_x - \frac{x g_z}{2} \right)^2 + \left(z g_y - \frac{y g_z}{2} \right)^2 \right] \tag{2.43b}$$

Note that B_c always has the same sign as B_0 such that the concomitant fields caused by gradients of opposite polarity will not cancel out. While the concomitant field associated with applied magnetic field gradients can often be neglected, gradients of very long duration and amplitude, such as diffusion gradients, can accumulate sufficient phase dispersion to cause signal voids.

2.3 Diffusion Weighted MRI

After the properties of the free diffusion process are discussed in 2.3.1, the dependence of the MRI signal on the diffusion parameters is discussed in 2.3.2.

2.3.1 The Free Diffusion Process

Adolf Fick was the first one to give a quantitative description of the diffusion process [19]. His first law, as stated in eq. (2.44) defines the diffusion coefficient by the relation between a concentration gradient ∇n and the diffusion flux $\boldsymbol{j}$ it causes.

$$\boldsymbol{j} = -D\nabla n \tag{2.44}$$

Together with the continuity equation (eq. (2.45a)) Fick's second law, which is also known as diffusion equation (eq. (2.45b)) arises.

$$\frac{\partial n(\boldsymbol{x},t)}{\partial t} + \nabla \boldsymbol{j}(\boldsymbol{x},t) = 0 \tag{2.45a}$$

$$\frac{\partial n(\boldsymbol{x},t)}{\partial t} = D\Delta n(\boldsymbol{x},t) \tag{2.45b}$$

If particles would initially be located at a position $\boldsymbol{x'}$, thus distributed as $n(\boldsymbol{x},0) = \delta(\boldsymbol{x}-\boldsymbol{x'})$ as shown in Fig. 2.2(a), the solution to eq. (2.45b) in three-dimensional space is given by eq. (2.46).

$$n(\boldsymbol{x},t) = \frac{1}{(4\pi Dt)^{-3/2}}\ \mathrm{e}^{-\frac{-(\boldsymbol{x}-\boldsymbol{x'})^2}{4Dt}} \tag{2.46}$$

If only the distribution along one coordinate axis x is considered, one yields a Gaussian distribution of the projections $P_S(x)$ with standard deviation σ_x, as depicted in Fig. 2.2(b).

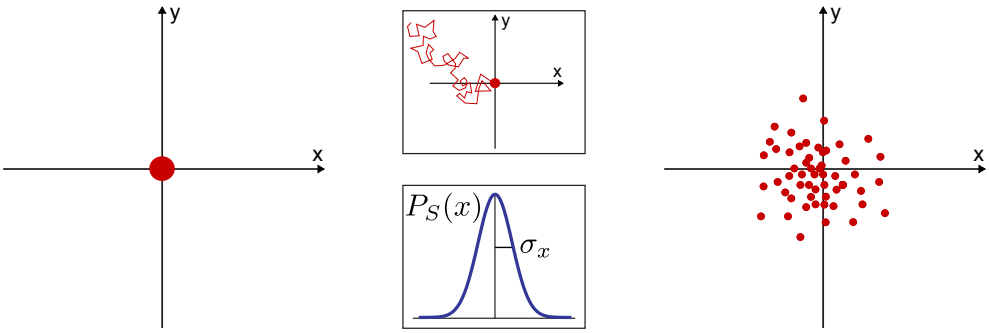

Figure 2.2: Particles initially located at a common location (a) undergo diffusive motion as depicted in (b). The displacement of the particles after a time t projected on one of the coordinates follows a Gaussian distribution $P_S(x)$ with standard deviation σ_x (after [20]).

The mean square displacement of the particle locations after a time t, which have spread out according to the diffusion equation (Fig. 2.2(c)), is thus given by the Einstein

equation (eq. 2.47) [21].

$$\langle x^2 \rangle = 2Dt \tag{2.47}$$

In the following section it will be derived, how a magnetic field gradient applied during the diffusive motion can be used to encode the displacement into the MRI signal.

2.3.2 Bloch-Torrey equations

The influence of diffusive motion on the signal measured in magnetic resonance experiments can be described by adding a diffusion term to the Bloch equations (eq. (2.13a)-(2.13c)), yielding the Bloch-Torrey equations [22], which for an isotropic diffusion coefficient D are given by (eq. 2.48).

$$\frac{\mathrm{d}\boldsymbol{M}}{\mathrm{d}t} = \gamma \boldsymbol{M} \times \boldsymbol{B} - \begin{pmatrix} 1/T_2 & 0 & 0 \\ 0 & 1/T_2 & 0 \\ 0 & 0 & 1/T_1 \end{pmatrix} (\boldsymbol{M} - \boldsymbol{M_0}) + D\Delta \boldsymbol{M} \tag{2.48}$$

To derive the time-evolution of the transverse magnetization in the presence of both diffusion and a magnetic field gradient $B_z = B_0 + \boldsymbol{x} \cdot \boldsymbol{g}$, we follow [23] and substitute the transversal magnetization to eliminate Larmor precession and T_2 signal decay by $M_{xy}(\boldsymbol{x}, t) = m_{xy}(\boldsymbol{x}, t)\ \mathrm{e}^{-i\gamma B_0 t - \frac{t}{T_2}}$, which yields eq. (2.49).

$$\frac{\partial m_{xy}(\boldsymbol{x}, t)}{\partial t} = -i\gamma m_{xy}(\boldsymbol{x}, t)\boldsymbol{x} \cdot \boldsymbol{g} + D\Delta m_{xy}(\boldsymbol{x}, t) \tag{2.49}$$

Recalling the definition of $\boldsymbol{k}$ (eq. 2.29a), we can separate magnitude and phase of m_{xy} using the substitution $m_{xy}(\boldsymbol{x}, t) = M(t)\ \mathrm{e}^{-2\pi i \boldsymbol{x} \cdot \boldsymbol{k}(t)}$, yielding eq. (2.50a). The solution for $M(t)$ is thus given by eq. (2.50b).

$$\frac{\partial M(t)}{\partial t} = M(t) D \mathrm{e}^{2\pi i \boldsymbol{x} \cdot \boldsymbol{k}(t)} \Delta \mathrm{e}^{-2\pi i \boldsymbol{x} \cdot \boldsymbol{k}(t)} = -4\pi^2 D M(t) \boldsymbol{k}(t) \cdot \boldsymbol{k}(t) \tag{2.50a}$$

$$\frac{M(t)}{M(0)} = \exp\left(-4\pi^2 D \int_0^t \boldsymbol{k}(t') \cdot \boldsymbol{k}(t') \mathrm{d}t'\right) \tag{2.50b}$$

Since the expression on the right hand side is equivalent to the ratio of the signal amplitudes with and without ($\boldsymbol{k} = 0$) applied gradients, the diffusion sensitivity of an MRI pulse sequence is typically described by the b-value, given by eq. (2.51a). For free isotropic diffusion, the attenuation of the diffusion weighted signal $S(b)$ is thus given by a simple exponential (eq. (2.51b)), where S_0 denotes the unweighted signal.

$$b = \gamma^2 \int_0^T \left(\int_0^t \mathbf{g}(t') \mathrm{d}t' \right)^2 \mathrm{d}t \tag{2.51a}$$

$$\frac{S(b)}{S_0} = \mathrm{e}^{-bD} \tag{2.51b}$$

In biological tissues, however, diffusion can seldom be considered free. Hindering cell membranes reduce the displacement and thus the measured apparent diffusion coefficient. Brain tissue, where properties of diffusion are often anisotropic [24], has been studied thoroughly after the initial discovery by Moseley *et al.* that ischemic regions can be detected in diffusion weighted MRI less than one hour after the onset of ischemia [2].

The focus of this work however is to investigate the biexponential signal decay, which is observed in strongly perfused organs. As will be shown in the following chapter, the presence of blood motion can cause the measured apparent diffusion coefficients to be larger than the free diffusion coefficient.

3 Methods: Development of pulse sequences for diffusion weighted MRI

After a short overview of selected pulse sequence techniques that are particularly relevant for diffusion sequences (section 3.1), the steps leading to the development of the diffusion weighted MRI sequence, which was used for the experiments presented in chapters 5and 6, are presented. The results of the first attempts, which consisted of integrating oscillating gradients into a manufacturer pulse sequence (section 3.2), indicated, that it would be necessary to flow compensate the imaging gradients. To be able to have full control over the applied pulses and gradients, a flow compensated diffusion sequence was programmed (section 3.3). To achieve higher b-values and higher effective diffusion times, bipolar and flow compensated gradients were chosen instead of sine and cosine gradients. However signal voids due to the presence of concomitant fields were observed for flow compensated gradients, when very high amplitudes for the diffusion gradients were used. Only by choosing a symmetric diffusion weighting scheme and thus compensating for Maxwell-currents (section 3.4), it was possible to overcome the signal voids and increase the diffusion time to 100 ms and more.

3.1 Concepts in pulse sequence programming

Most diffusion MRI experiments are performed using echo planar imaging. After introducing this pulse sequence type and motivating its use for diffusion imaging (section 3.1.1), the concept of gradient moment nulling is explained and discussed for both diffusion weighting and imaging gradients (section 3.1.2). A formalism which allows one to discuss the diffusion weighted signal in terms of characteristic frequencies of the diffusion process is afterwards discussed (section 3.1.3).

3.1.1 Echo planar imaging

In the field of MRI, a large spectrum of different pulse sequences is used. A sequence which is widely used and which combines the basic pulse sequence elements that were introduced in section 2.2, is the fast low-angle shot (FLASH) sequence [25, 26]. Its basic sequence timing is depicted in Fig. 3.1. It should be noted that slice rephasing gradient, phase encoding (PE) and the dephasing gradient for the readout (to start measuring at one end of the k-space line to acquire) are applied simultaneously and are separated

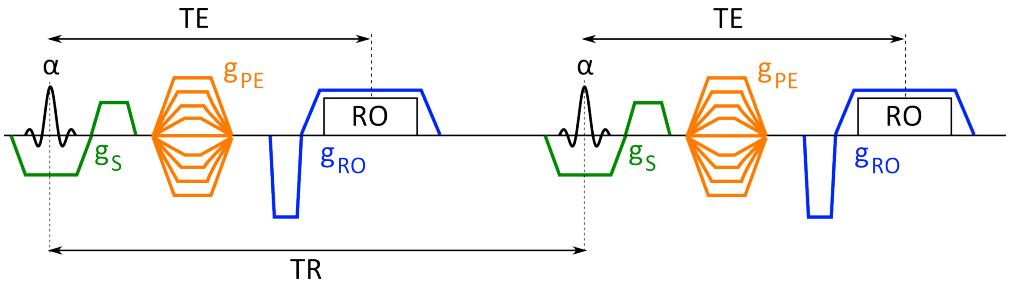

Figure 3.1: Two repetitions of the basic FLASH sequence. After excitation by the flip angle α, phase encoding (PE) gradients are applied and the signal for a line in k-space is acquired. The echo time TE is the time between excitation and center of the readout (RO), the repetition time TR is the time between two subsequent excitation pulses.

in Fig. 3.1 for illustration purposes. The use of small flip angles has the advantage, that the time necessary for the M_z magnetization to recover, and thus the repetition time TR, can be kept very short. If, for example, 128 lines in k-space are acquired for TR = 15 ms, the acquisition time for the total image is $\approx$ 2 s. However, if additional diffusion gradients shall be applied between excitation and readout, the echo time needs to be increased such that the T_2^*-decay gets more pronounced and larger flip angles would be appreciated. For large flip angles, TR needs to be chosen in the order of $\approx$ 1 s, which leads to acquisition times in the order of minutes. While efforts are made to accumulate b-value over several repetitions and keeping low flip angles and short repetition times [27], the typical approach used in diffusion weighted MRI is to acquire several k-space lines for one diffusion preparation. Fig. 3.2(a) shows the timing of the echo planar imaging (EPI) readout, while the acquisition order of k-space is illustrated in Fig. 3.2(b). Originally proposed by Mansfield [28], the k-space is either acquired as a whole (singleshot) or separated over several repetitions (segmented). To reduce the effect of T_2^*-decay during the echo train and to increase the available signal at the readout, refocusing pulses are employed which typically are timed such that the spin echo forms when the k-space center is acquired.

Parallel imaging is an umbrella term for techniques which uses simultaneously acquired signals from several coils to accelerate acquisition in k-space by undersampling the data and reconstructing the missing information. In this work the algorithm called generalized autocalibrating partially parallel acquisitions (GRAPPA) [30] is used. Undersampling is performed along the phase encoding direction such that except for reference lines around the k-space center, only every second line is acquired. The number of k-space lines, which need to be acquired (and thus the length of the echo train and possible geometric distortions due to field inhomogeneities) can further be reduced by exploiting

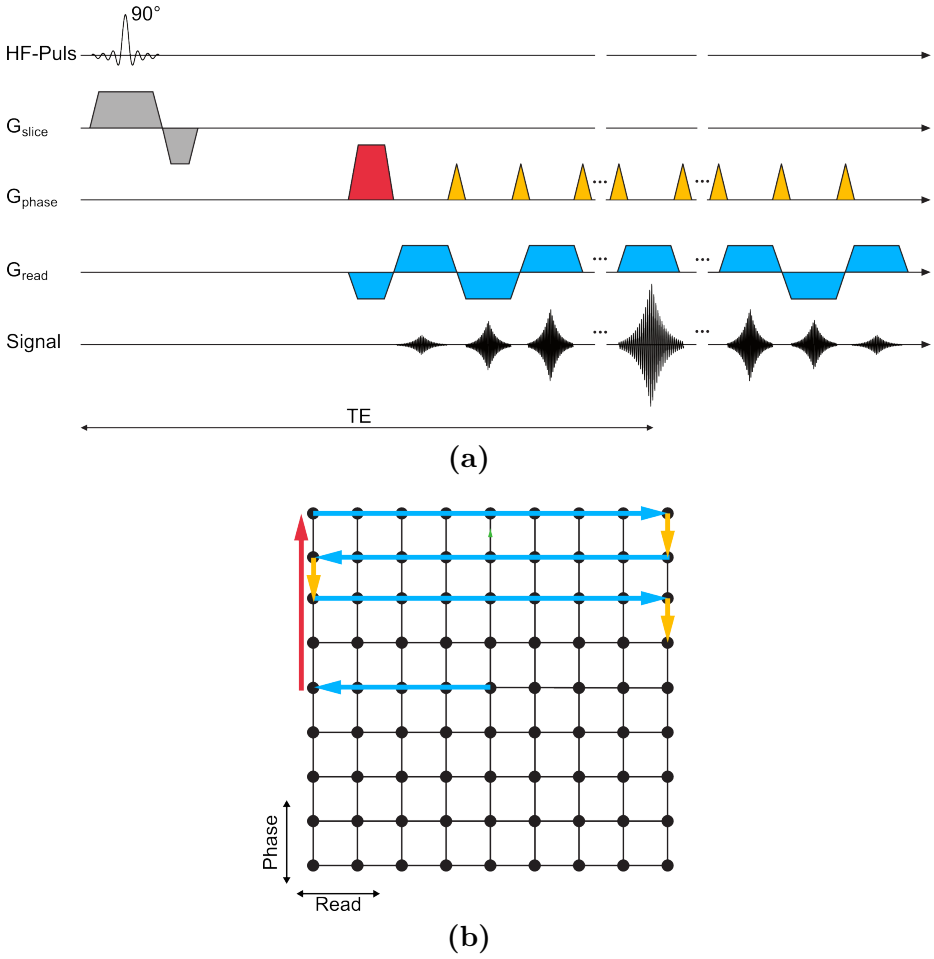

Figure 3.2: (a) Timing of an echo planar imaging (EPI) readout. The *prephasing* (red) and *dephasing* (first blue lobe) gradients select one of the *corner* points of k-space. After one line is acquired, a short phase encoding *blip* is played out, before the subsequent line is acquire in opposite direction (sign inversion of the frequency encoding gradient). (b) shows the order in which the signal in k-space is acquired. Modified after [29].

the k-space symmetry (eq. (2.34)) with partial Fourier (see section 2.2.2).

Residual eddy currents can be caused by switching the diffusion gradients on or off. If eddy currents are assumed to decay exponentially with a time constant that is of the order of several 10 ms, the eddy currents caused by switching a much shorter gradient on and off approximately cancel out. For longer gradients, such as diffusion gradients, the eddy currents caused by the onset of the gradient are already decayed and eddy currents from the ramp down of the gradient continue to exist as residual eddy currents. By using a twice-refocused spin echo sequence, such as the one used as a starting point in section 3.2, it is however possible to reduce the residual eddy currents active during the readout and thus the distortions caused [31, 32].

3.1.2 Gradient moment nulling

The phase that a particle acquires due to applied magnetic field gradients can be discussed with the help of gradient moments. Following [9], p. 336ff., the time-evolution of the location $\boldsymbol{x}(t)$ of a particle can be written as a Taylor series (eq. 3.1, where $\boldsymbol{x_0}$ denotes the initial location, $\boldsymbol{v_0}$ the initial velocity and $\boldsymbol{a_0}$ the initial acceleration.

$$\boldsymbol{x}(t) = \boldsymbol{x_0} + t\boldsymbol{v_0} + \frac{t^2}{2}\boldsymbol{a_0} + \cdots \tag{3.1}$$

The phase of the magnetization (recalling eq. (2.26b)) can then be expanded into gradient moments (eq. (3.2a)), where the n^{th} gradient moment $\boldsymbol{m_n}$ is given by eq. (3.2b).

$$\phi(t) = \gamma \int_0^t \boldsymbol{x}(t') \cdot \boldsymbol{g}(t')\mathrm{d}t' = \gamma \left(\boldsymbol{x_0} \cdot \boldsymbol{m_0}(t) + \boldsymbol{v_0} \cdot \boldsymbol{m_1}(t) + \frac{1}{2}\boldsymbol{a_0} \cdot \boldsymbol{m_2}(t) + \cdots \right) \tag{3.2a}$$

$$\boldsymbol{m_n}(t) = \int_0^t (t')^n \boldsymbol{g}(t')\mathrm{d}t' \tag{3.2b}$$

For many imaging gradients, such as rephasing, dephasing or phase encoding gradients, the 0^{th} gradient moment is determined by the imaging parameters, the exact shape of the gradient however can be chosen as desired. Similarly, a diffusion gradient profile typically has the constraints that the total 0^{th} gradient moment must be zero (rephasing condition), such that imaging is not disturbed and that the diffusion gradients must cause the signal attenuation specified by the b-value. The term *flow compensated* refers to the condition when the $^{\text{st}}$ gradient moment equals zero. For a detailed discussion of different gradient schemes, it shall be referred to section 4.4. Here it shall be only noted, that a cosine gradient profile and the flow compensated profiles used in the remainder of this chapter yield a total $\boldsymbol{m_1} = 0$, whereas the sine and bipolar profile are not flow compensated, thus $|\boldsymbol{m_1}| > 0$. Generally spoken, a gradient waveform with zero net area ($\boldsymbol{m_0}(t) = 0$), which is symmetric with respect to time, thus $\boldsymbol{g}\left(\frac{t}{2} - t'\right) = \boldsymbol{g}\left(\frac{t}{2} + t'\right)$ yields

$\boldsymbol{m_1}(t) = 0$. Also, it can be desirable to calculate the first moment $\tilde{\boldsymbol{m}}_{\boldsymbol{1}}(\Delta t)$, that a gradient waveform applied during t_1 and t_2 causes at time $t = t_1 + \Delta t$. Its relation to the the zeroth and first moment of the gradient waveform is given by eq. (3.3).

$$\tilde{\boldsymbol{m}}_{\boldsymbol{1}}(\Delta t) = \int_{t_1}^{t_2} -(t_1 + \Delta t - t')\boldsymbol{g}(t')\mathrm{d}t' = \int_0^{t_2-t_1} -(\Delta t - t')\boldsymbol{g}(t' + t_1)\mathrm{d}t' = -\Delta t \boldsymbol{m_0} + \boldsymbol{m_1} \tag{3.3}$$

For the sequence developed in section 3.3, eq. (3.3) is used to calculate the gradient waveforms that need to be used such that imaging gradients yield zero net first moment.

3.1.3 Temporal diffusion spectroscopy

The term temporal diffusion spectroscopy was introduced by the group around Does [33]. They showed that using oscillating gradient profiles of varying oscillation frequency for diffusion weighting can potentially yield information on intra-cellular structures as the size of cell nucleus [34, 35]. The idea of using oscillating gradients was first brought up by Stepišnic [36], who related the signal attenuation of the diffusion weighted signal to the Fourier transform $\tilde{D}_{xx}(\omega)$ of the velocity autocorrelation function along the axis x of the applied diffusion gradients. The relation between velocity autocorrelation function and spectrum $\tilde{D}_{xx}(\omega)$ is given by eq. (3.4), whereas the symmetry of the velocity autocorrelation function $\langle v_x(0)v_x(-t)\rangle = \langle v_x(0)v_x(t)\rangle$ is used. The brackets $\langle \cdots \rangle$ denote the average over all particles in the ensemble.

$$\tilde{D}_{xx}(\omega) = \frac{1}{2}\int_{-\infty}^{\infty} \langle v_x(0)v_x(t)\rangle \mathrm{e}^{i\omega t}\mathrm{d}t = \int_0^{\infty} \langle v_x(0)v_x(t)\rangle \cos(\omega t)\mathrm{d}t \tag{3.4}$$

The exponent $\alpha(t)$ of the attenuation of the diffusion weighted signal, which is in case of free diffusion given by $\alpha(t) = -bD$ (compare with eq. (2.51b)), can be rewritten using $\tilde{D}_{xx}(\omega)$ [36] as shown in eq. (3.5a). The weighting function $S_x(\omega, t)$ can be calculated from the Fourier transform of the gradient profile as given by eq. (3.5b).

$$\alpha(t) = \frac{\gamma^2}{2\pi}\int_{-\infty}^{\infty} \tilde{D}_{xx}(\omega) S_x(\omega, t)\mathrm{d}\omega \tag{3.5a}$$

$$S_x(\omega, t) = \frac{\left|\int_0^t g_x(t')\mathrm{e}^{-i\omega t'}\mathrm{d}t'\right|^2}{\omega^2} \tag{3.5b}$$

The weighting functions for sine and cosine profiles with typical parameters are shown in Fig. 3.3. In the top row, the effective magnetic field gradients (sign inversion upon a refocusing pulse) for 5 oscillations and an oscillation period of 5 ms are depicted. The corresponding weightings $S(\omega, t)$ are shown in the bottom row. While the sine profile is most sensitive to low frequency components and has additional lobes at $\pm\omega_0$ (here $\omega_0 = \frac{2\pi}{T} \approx 1.26$ kHz) as can be inferred from Fig. 3.3(c), the cosine profile misses the central

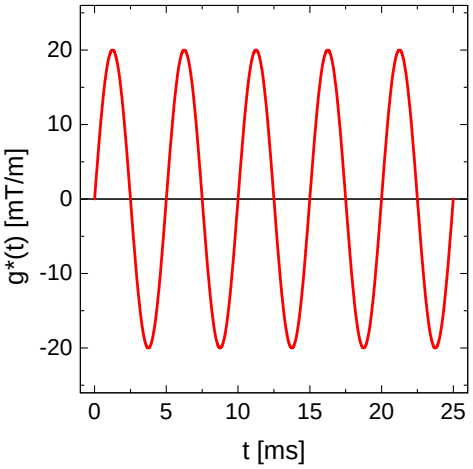

(a) Sine gradient profile.

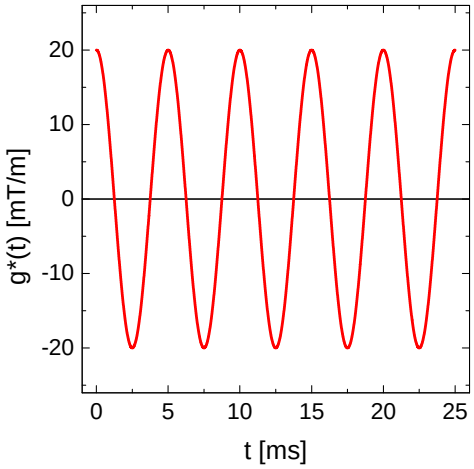

(b) Cosine gradient profile.

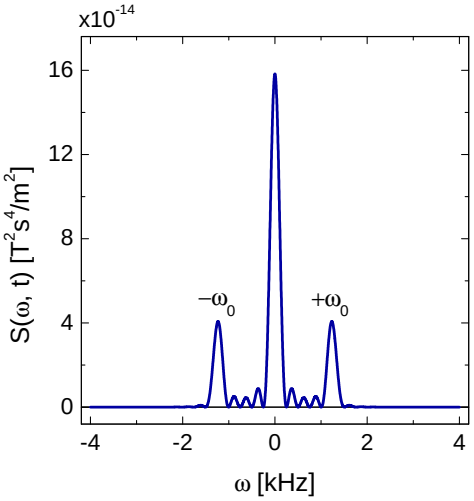

(c) Spectral weighting for sine gradients in (a).

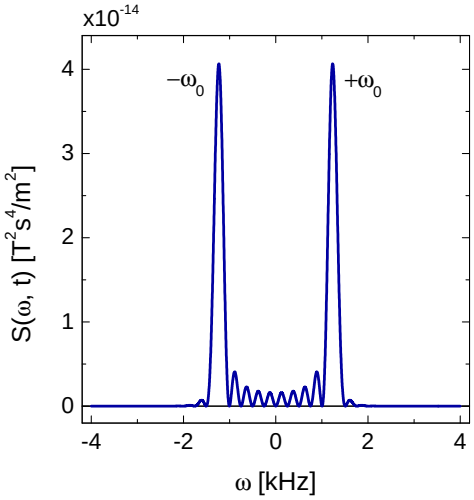

(d) Spectral weighting for cosine gradients in (b).

Figure 3.3: Sine and cosine gradient profiles (top row) and their respective spectral weightings $S(\omega, t)$ (bottom row), where $t = 25$ ms. Both spectral weightings show peaks at the oscillation frequency $\pm\omega_0$. The cosine profile misses the central lobe at $\omega = 0$, which can be explained by its temporal symmetry and thus its flow compensation.

lobe (Fig. 3.3(d)), which is a property inherent to all flow compensated gradient profiles. The fact that the net area under the $S(\omega, t)$ curve for cosine gradients is much less than for sine gradients, also reflects in the b-value. For free diffusion (uncorrelated particle movements) the velocity autocorrelation function is given by $\langle v_x(0)v_x(t)\rangle = 2D\delta(t)$ yielding $\tilde{D}(\omega) = D$. Thus the b-value is given by eq. (3.6a), yielding the formulas for sine (eq. 3.6b) and cosine (eq. 3.6c) gradients, where N is the number of oscillations, T the total time the diffusion gradient profile is applied and g is the maximum amplitude of the magnetic field gradient.

$$b(t) = \frac{\gamma^2}{2\pi}\int_{-\infty}^{\infty} S(\omega, t)\mathrm{d}\omega \tag{3.6a}$$

$$b_{\sin} = \frac{3\gamma^2 g^2 T^3}{8\pi^2 N^2} \tag{3.6b}$$

$$b_{\cos} = \frac{\gamma^2 g^2 T^3 (1 + \frac{1}{4N})}{8\pi^2 N^2} \tag{3.6c}$$

IVIM model A brief derivation of the diffusion spectrum in the IVIM model is given here to motivate the use of oscillating gradients. The model is in detail discussed in chapter 4. Particles are assumed to travel with a characteristic velocity v and change their direction after a characteristic time τ. If movement before and after a directional change is assumed uncorrelated, the velocity autocorrelation function is given by $\langle v_z(0)v_z(t)\rangle = \langle v_z(0)^2\rangle \left(1 - \frac{|t|}{\tau}\right)\Theta(\tau - |t|)$, where $\Theta(t)$ denotes the heaviside function [37]. Using that for isotropically distributed velocity directions $\langle v_z(0)^2\rangle = \frac{v^2}{3}$ and introducing the pseudo-diffusion coefficient $D^* = \frac{v^2\tau}{6}$, $\tilde{D}(\omega)$ is given by eq. (3.7).

$$\tilde{D}(\omega) = \frac{v^2}{3}\int_0^{\tau}\left(1 - \frac{t}{\tau}\right)\cos(\omega t)\mathrm{d}t = 2D^*\frac{1 - \cos(\tau\omega)}{\tau^2\omega^2} \tag{3.7}$$

Fig. 3.4 shows that $\tilde{D}(\omega)$ normalized on D^* has a characteristic dependence on the product $\tau\omega$. This implies, that if $\tilde{D}(\omega)$ could be probed at different frequencies using oscillating gradients of known ω, it would be possible to obtain information on the characteristic timescale τ of the incoherent motion.

3.2 Implementation of oscillating gradients in product sequence

The sequence into which the oscillating gradients were inserted, was a twice-refocusing diffusion EPI sequence. The timing of the refocusing pulses was such that eddy current elimination for a time constant $\tau = 70$ ms was achieved [31]. The original diffusion

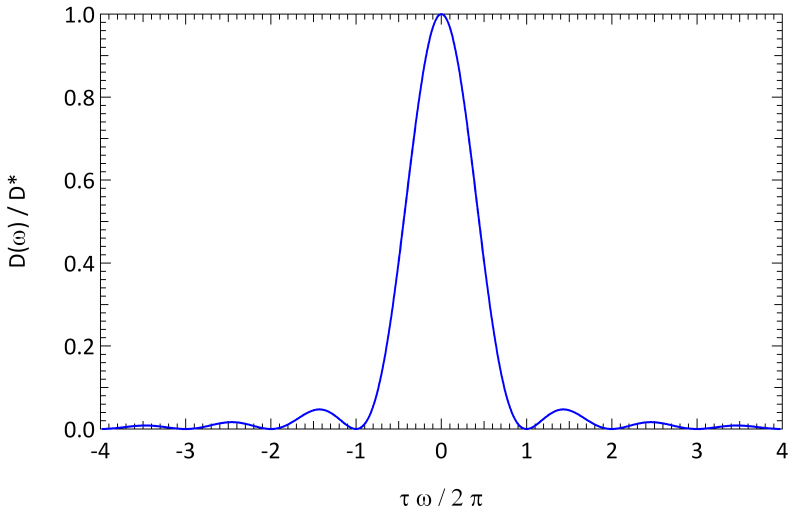

Figure 3.4: Normalized spectrum of the velocity autocorrelation function for the IVIM model discussed in chapter 4. Probing the spectrum using oscillating gradients would allow one to obtain information on the characteristic timescale τ of the incoherent motion.

gradients were replaced by oscillating gradients between the two refocusing pulses as shown in Fig. 3.5. The sequence was tested using a homogeneous spherical water phantom and a flow phantom, which was developed in the course of a bachelor thesis [29]. The flow phantom consisted of a tube of inner diameter 4 mm, which was wound around a paper roll such that the water would flow circularly around the paper roll. Two striking findings based on the data measured in those experiments, however, leaded to a discontinuation of the work with this pulse sequence.

Signal increase for flow and cosine gradients Fig. 3.6 shows the diffusion coefficients obtained by a two-point exponential fit from measurements using a flow-phantom as described in [29]. Signal attenuation and thus diffusion coefficients obtained by an exponential fit are larger for sine than for cosine gradients, which is expected, since cosine gradients are flow compensated. In case of cosine gradients, however, for some of the oscillation frequencies an increase of the diffusion weighted signal compared to the unweighted signal is found. The most likely explanation of this phenomenon was that the supposedly unweighted signal is in fact strongly attenuated by flow, since the pulse sequence itself is not flow-compensated. While the addition of cosine gradients, which are flow-compensated by themselves and should thus not change the overall m_1 of the sequence, cannot explain the increase in signal, it was found that the directions of the crusher gradients, which need to be applied in combination with refocusing pulses (for

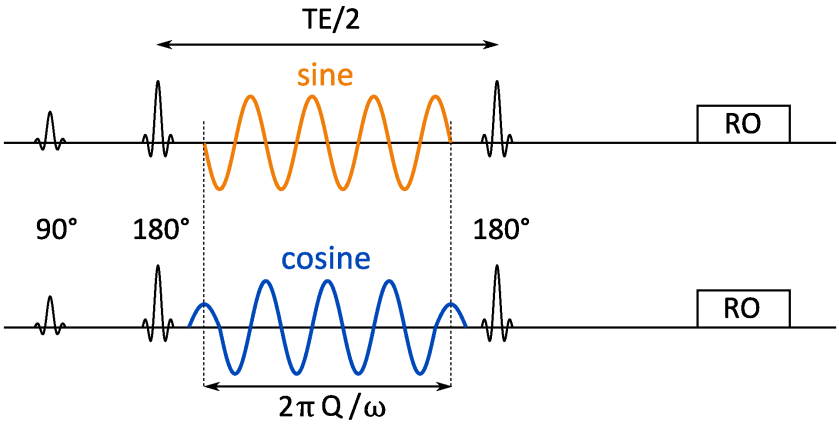

Figure 3.5: Sequence timing of modified diffusion EPI manufacturer sequence. Instead of the original diffusion gradients the user can choose between sine (top) or cosine gradients (bottom), which were inserted between the two refocusing pulses.

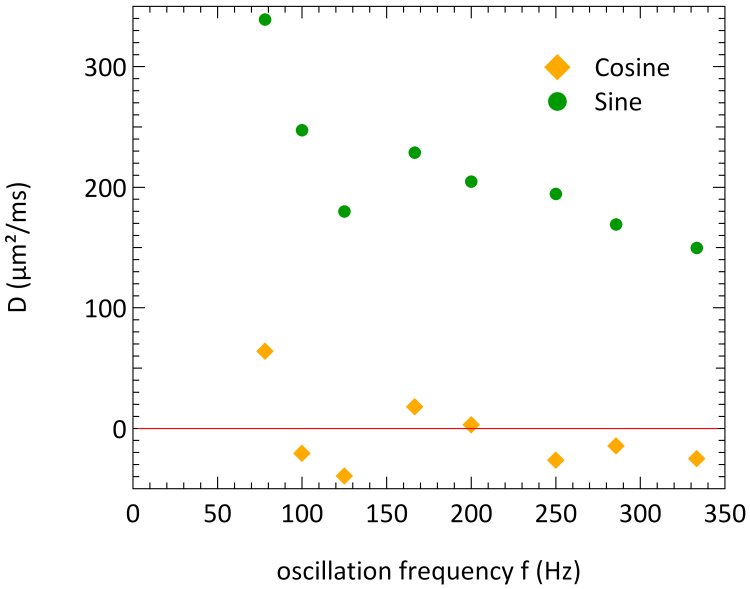

Figure 3.6: Diffusion coefficients measured using the phantom described in [29]. Gradients were applied simultaneously in slice selection and readout direction, where flow was directed in readout direction with $v \approx 35$ cm/s. Signal attenuation for sine gradients is larger than for cosine gradients, as expected. For cosine gradients, however, signal also increases compared to the unweighted reference image (negative D).

details, see [9], p. 305) are applied by the manufacturer sequence with different signs for weighted and unweighted acquisition, which could explain changes in the the first moment and thus the velocity encoding of the sequence. To have full control over the imaging gradients, it was decided to build a diffusion EPI sequence from scratch.

Signal attenuation increases with oscillation frequency Fig. 3.7 shows the diffusion coefficients, which were measured in a spherical phantom, which in other experiments showed to contain a solution in which water molecules exhibit free diffusion with $D \approx 2.15\ \mu\mathrm{m}^2/\mathrm{ms}$. While this is approximately the value that was measured for low oscillation

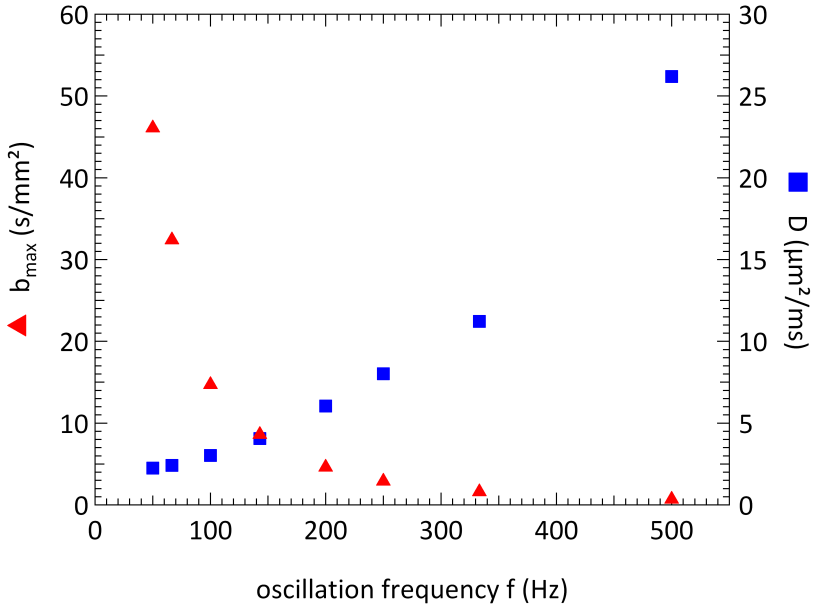

Figure 3.7: Measured diffusion coefficients for the modified EPI manufacturer sequence with inserted cosine gradients. Due to gradient system limitations, the maximum achievable b-value is proportional to ω^{-2}. However, this alone cannot explain the increase in the measured diffusion D.

frequencies, the cosine signal decays much stronger with increasing frequency. The reason for this behavior could not be clarified with ultimate certainty. One problem is, that the maximum achievable b-value, which is also shown in Fig. 3.7, is basically limited by the maximum achievable gradient amplitude of the scanner, which nominally was 40 mT/m per axis. According to eq. (3.6c), the b-value for cosine is proportional to N^{-2} and thus to ω^{-2}. This leads to the fact, that for large ω and thus the small achievable b-values the diffusion coefficient can only be determined with small accuracy. However the absolute value should not be affected as much as in the experiments. Apart from the gradient

system operating at its limits in terms of amplitude and slew rate for large oscillation frequencies and thus the really applied gradients might differ from the intended ones, it is also possible that concomitant fields caused by the oscillating gradients contributed to the increased signal decay.

3.3 Development of a flow compensated diffusion sequence

The basic sequence design of the flow compensated diffusion sequence was inspired by the manufacturer sequence used in the previous section. To be able to achieve higher b-values while having the possibility to use two different diffusion gradient profiles, one of which being flow compensated and the other not, it was chosen to move from oscillating gradients back to bipolar and flow compensated gradients as shown in Fig. 3.8. Bipolar

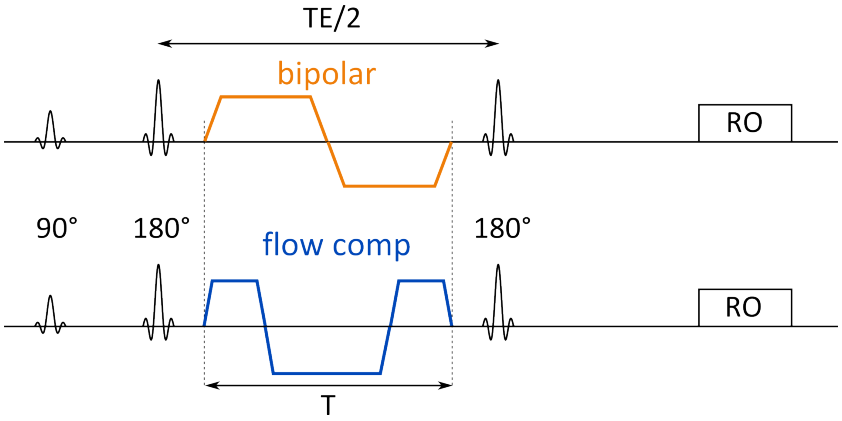

Figure 3.8: Basic sequence timing of the self-written diffusion EPI sequence. Diffusion gradients were inserted between the two refocussing pulses. The timescale τ of the incoherent motion could be probed by varying the total duration T of the diffusion weighting gradients.

and flow compensated gradient schemes could be considered as rectangularized versions of just 1 oscillation of sine, respectively cosine gradients, where the *frequency* could be varied by changing the total time T of the diffusion experiment. The b-values for bipolar and flow compensated gradients are given by eq. (3.8a) and (3.8b), where ramp times (which were of course considered in sequence programming) are neglected.

$$b_{\text{bip}} = \frac{\gamma^2 g^2 T^3}{12} \tag{3.8a}$$

$$b_{\text{fc}} = \frac{\gamma^2 g^2 T^3}{48} \tag{3.8b}$$

As can be inferred from those equations, twice the gradient amplitude of the bipolar profile is needed to obtain the same b-value using the flow compensated profile at the same diffusion time T.

Apart from the low b-values that can be obtained on a clinical MRI scanner for oscillating gradients, the other main reason to move away form the manufacturer sequence used in section 3.2 was to be able to control and flow-compensate the imaging gradients. A basic search algorithm was implemented to solve the flow-compensation problem, which is described in section 3.3.1. It is then used to calculate the necessary gradients for slice selection, phase encoding and readout.

3.3.1 Basic flow compensation problem

The basic flow compensation problem is illustrated in Fig. 3.9. The typically used

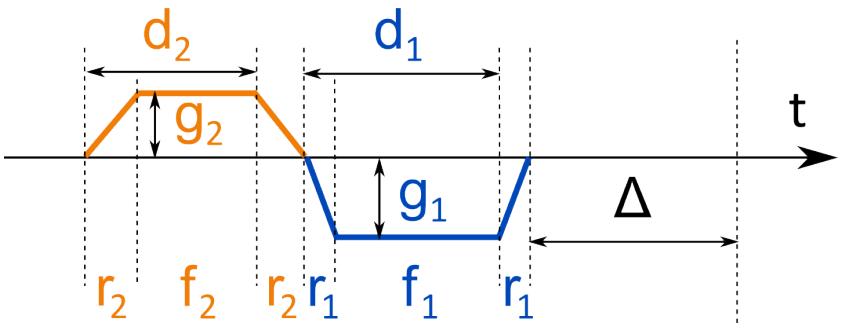

Figure 3.9: Illustration of the basic flow compensation problem. Two gradients labeled 1 and 2 need to be tuned regarding their amplitude g_i, duration d_i and ramp time r_i such that at a time Δ after the last gradient the moments m_0 and $\tilde{m}_1$ are created.

gradients in MRI have a trapezoidal profile, which can be characterized by the amplitude g, the ramp time r and the duration d, which is the sum of ramp time and flat top time f. With a pair of such gradients it is basically possible to create any combination of m_0 and m_1 at a time Δ after the second gradient is applied. Recalling eq. (3.3) the temporal shift can be included into $\tilde{m}_1$. However, since the gradient durations are not known *a priori*, eq. (3.3) cannot be applied directly. Since the desired m_0 is unaffected by Δ, the moment created at a time $\tilde{m}_1(t-\Delta)$ is given by $\tilde{m}_1(t)+m_0\Delta$. The equations that need to be fulfilled can thus be stated as follows (eq. (3.9a) and (3.9b)).

$$m_0 = g_1 d_1 + g_2 d_2 \tag{3.9a}$$

$$\tilde{m}_1 + m_0\Delta = -\left(r_1 + d_1 + \frac{r_2 + d_2}{2}\right) g_2 d_2 - \frac{r_1 + d_1}{2} g_1 d_1 \tag{3.9b}$$

The parameter range is thus limited by the gradient system. Typically a maximum gradient amplitude $g_{\max}$ is possible and a maximum slew rate respectively minimum gradient rise time $r_{\min}$ can be realized, thus $g_i r_{\min} < r_i$. For the used MRI scanner (Siemens Magnetom Avanto), the specified limits were $g_{\max} = 40$ mT/m and $r_{\min} = 5.88$ us/(mT/m), where each gradient timing must be on a time raster of width 10 μs. While a gradient pair fulfilling eq. (3.9a) and (3.9b) is not unique, it is desired to achieve the compensation in the shortest possible time. The basic version of the algorithm thus varies d_i and r_i to find the solution with the shortest total gradient time $d_1 + d_2 + r_1 + r_2$. The algorithm is used in the sequence to solve the arising flow compensation problems for slice selection gradients, phase encoding gradients and readout gradients. Details on the exact implementations can be found in [9], p. 331ff. While it is possible to achieve flow compensation along the slice encoding direction, for the readout axis it is strictly possible only for a single point in each line. The gradient reversal of the readout train however ensures that the first gradient moments, which were built up during the acquisition of the previous line are canceled out again by the acquisition of the current line. For the phase encoding direction, it is strictly speaking only possible to achieve flow compensation for the k-space center, since the hardware limitations do not allow to include full compensation gradients in the time the small time frame available for phase encoding between the acquisition of two succeeding lines. The gradient shape that was used for the phase blips was designed such that the build up of a first moment (which is inevitable due to the existence of non-zero first moments in every line except for the center line) is counteracted best.

3.3.2 Validation of pulse sequence

The sequence was tested using a straight flow phantom consisting of a tube of diameter 1.0 cm. Measurements were performed with resting and flowing water, where the measured flow velocity was $v = 0.8$ cm/s. While the signal attenuation curves for flow compensated diffusion gradients in Fig. 3.10 were essentially identical for flowing and resting water, the bipolar signal was already decayed at b-values less than 5 s/mm^2. The flow compensated pulse sequence was applied in vivo and different signal attenuations for flow compensated and bipolar diffusion gradients were reported [38]. Since the study is similar to the one presented in full detail in chapter 5, only the impact of the measurem

3.4 Compensation for concomitant fields

An algorithm to reduce the influence of concomitant fields was described by Zwanger *et al.* [39]. Since the concomitant fields cause an additional gradient field of parabolic spatial dependence, the best possible correction that can be performed using linear magnetic fields is to apply an offset to the diffusion gradients, which compensates the

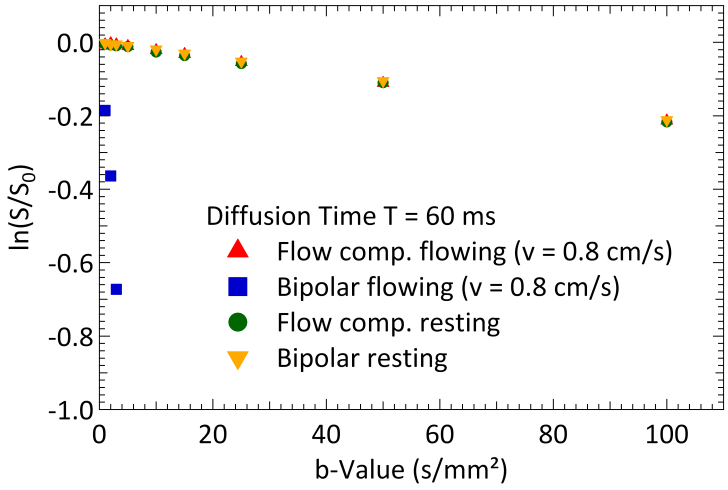

Figure 3.10: Signal attenuation measured in a straight water flow phantom. While in case of flow and bipolar diffusion gradients, the signal already decays at very small *b*-values, the signal attenuation curves for flow compensated gradients are unaffected.

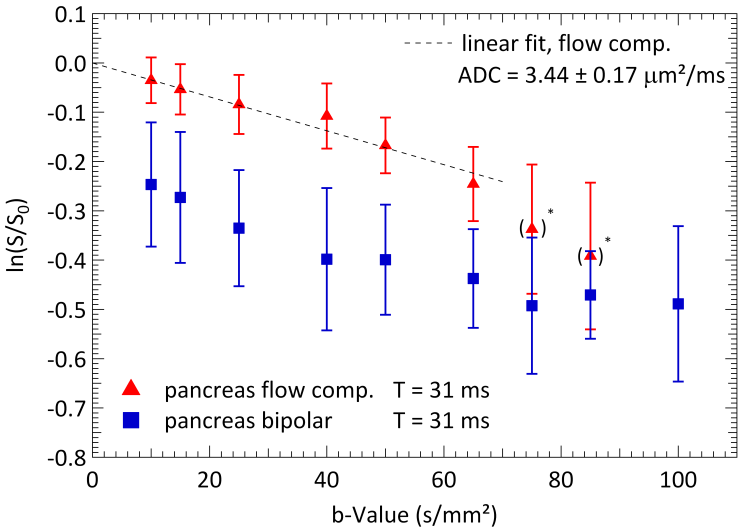

Figure 3.11: Experimental pancreas data. While different signal attenuation for flow compensated and bipolar diffusion gradients was shown, the flow compensated data at higher *b*-values suffered from dephasing effects that caused signal voids (*) and deviations from a monoexponential signal behavior.

parabolic concomitant field for the center of the slice. This algorithm was implemented into the diffusion sequence and the influence of signal voids reduced. Another design problem however led to a change in the diffusion gradient timing. Due to the fact that the diffusion gradients were inserted between two refocussing pulses only half of the echo time was available for the diffusion experiment. With the sequence shown in Fig. 3.8 diffusion times larger than 60 ms needed an increased echo time and caused loss of SNR. To be able to use the same echo time for all diffusion times, the sequence scheme shown in Fig. 3.12 was employed. The sequence design shown in Fig. 3.12 has a second

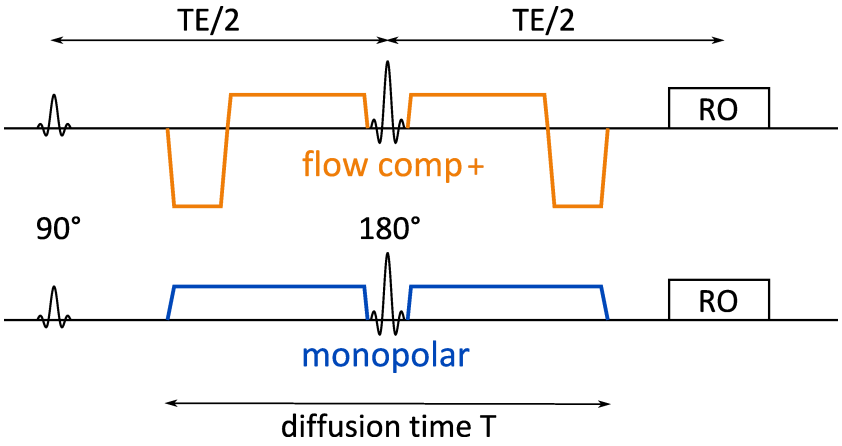

Figure 3.12: New diffusion sequence design. Except for a small time needed for the imaging gradients, the whole echo time can be used for diffusion gradients. Temporally symmetric gradient schemes are intrinsically compensated for dephasing caused by concomitant fields.

advantage. If a symmetric diffusion gradient scheme, such as the monopolar or the flow comp+ scheme, the dephasing caused by concomitant fields before and after the refocusing pulse cancels out. The sequence design shown in Fig. 3.12 is used for the experiments presented in chapter 5.

4 Methods: Signal attenuation in the intravoxel incoherent motion model

In this chapter, the intravoxel incoherent motion (IVIM) model, which was originally suggested by Denis Le Bihan [4], will be introduced. According to his follow-up publication [5], the signal attenuation in case of IVIM depends on the timescale of the incoherent motion. If the timescale is much shorter than the time in which diffusion sensitizing gradients are applied, the resulting signal can be described by a biexponential decay. While current IVIM research applications [40–42] exclusively assume this limit, our experimental results (see chapter 5) indicate that use of this limit might not be appropriate to describe the signal attenuation in strongly perfused organs. As will be worked out in the course of this chapter, the signal attenuation in the biexponential limit would only depend on the b-value (defined by eq. (2.51a)), but not on the exact timing of the applied gradients. However, we observed a strong dependence on both duration and temporal profile of the diffusion sensitizing gradients [43].

After a short presentation of the IVIM model and its underlying assumptions in section 4.1, an approach to calculate the signal attenuation of the perfusion fraction is described in section 4.2. This allows one to examine the influence of different gradient profiles and variable timescales. The necessary equations that allow to generate those phase distributions and the results for the typically used gradient schemes will be described in section 4.3, while the phase distributions for different gradient profiles are compared in 4.4. This not only bridges the gap between the corner cases already described in [5], but also allows to describe the experimentally observed signal attenuation curves and derive microscopic IVIM parameters from fitting the model to acquired diffusion MRI data in chapters 5and 6.

While in the case of the biexponential model the diffusion coefficient of blood is typically neglected, it becomes apparent that it needs to be taken into account for flow compensated gradient schemes. In section 4.5 the work of Henkelman *et al.* [44, 45] will be followed, revealing that the apparent diffusion coefficient of blood must be described by a heavily exchanging multi-compartment system and not only changes with b-value, but also depends on the diffusion gradient profile and sequence parameters such as echo time.

4.1 Intravoxel incoherent motion model

The term "Intravoxel Incoherent Motion" (IVIM) introduced by Le Bihan [4] refers to a two-compartment model which takes into account the contributions of both diffusion and perfusion to the signal decay observed in diffusion weighted MRI. While the perfusion compartment contributes the perfusion fraction f to the unweighted MRI signal S_0, the tissue compartment yields the remaining fraction 1-f. Signals from both compartments are attenuated according to their respective apparent diffusion coefficients, which are D for the tissue fraction and D_b for the perfusion fraction, where the latter experiences additional dephasing and thus a resulting signal decay F due to perfusive motion during the applied magnetic field gradients [5]. In the pancreas, which is one of the abdominal organs which show an attenuation curve that is very different from a monoexponential decay, the perfusion fraction in the pancreas was identified as blood [46], which is denoted by the index of its apparent diffusion coefficient D_b (only accounting for the diffusive part of motion of water molecules in blood). The basic IVIM signal equation (4.1) can thus be stated as follows:

$$S(b) = S_0 \left((1-f)\mathrm{e}^{-bD} + f\mathrm{e}^{-bD_b} \cdot F \right), \tag{4.1}$$

where the signal attenuation caused by dephasing is given by the expectation value $F = |\left\langle \mathrm{e}^{\mathrm{i}\phi} \right\rangle| = \left| \int \rho(\phi)\mathrm{e}^{\mathrm{i}\phi}\mathrm{d}\phi \right|$, where $\rho(\phi)$ denotes the distribution of phases that water molecules in blood obtained due to diffusive motion during the diffusion sensitizing gradients. Note that the only difference between eq. (4.1) and the version stated in the original work [5] is, that the diffusion of the perfusion fraction is described by a separate diffusion coefficient D_b, which will in detail be discussed in section 4.5. To derive the exact dependencies of F, the underlying assumptions of the IVIM model regarding blood motion need to be formulated.

Assumptions in the IVIM model

- Blood particles move with velocity $\mathbf{v}$ during the total duration T of the diffusion gradients. The movement speed $v = |\mathbf{v}|$ is either the same for all particles – which will be assumed in the remainder of this chapter – or follows a distribution, which will be examined in section 5.2.

- After a characteristic time τ passed, a particle changes its movement direction (keeping constant speed v).

- The first directional change occurs after a time $t_1 = r\tau$, where r is a random real number between 0 and 1. r is homogeneously distributed and different for each particle.

- Velocity directions are randomly distributed. The distribution of velocities is isotropic and the velocity directions before and after a change are uncorrelated.

We will now examine the two corner cases regarding the characteristic time τ, which are illustrated in Fig. 4.1.

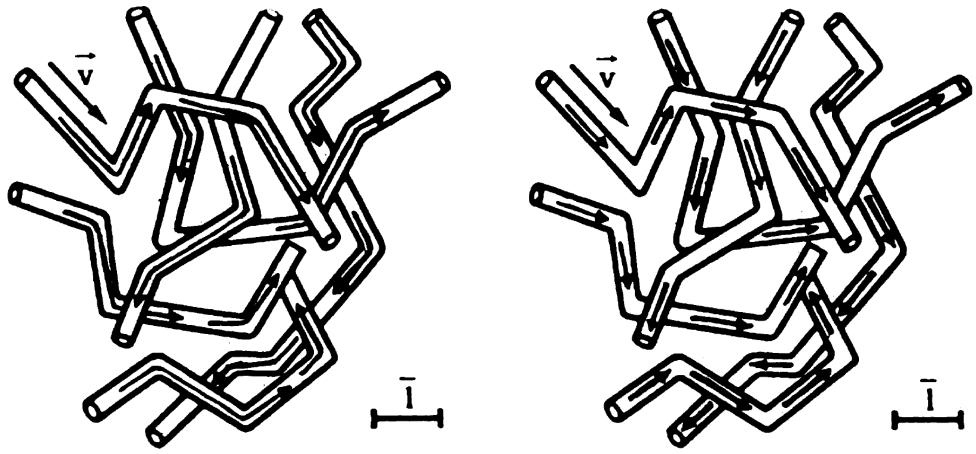

(a) first model **(b)** second model

Figure 4.1: According to Le Bihan [5], attenuation of the blood signal is a function of blood velocity $\bar{v}$ and characteristic lengthscale $\bar{l}$ of the network. (a) When blood flow changes its direction several times during the diffusion experiment, $F = \mathrm{e}^{-bD^*}$ can be described by a pseudo-diffusion coefficient D^*. (b) In the other extreme case, velocity doesn't change during the diffusion gradients with velocity encoding c and $F = |\mathrm{sinc}(c \cdot v)|$.[1]

Pseudo-diffusion limit The case, which was named *first model* by Le Bihan [5] is depicted in Fig. 4.1(a). If τ is several times smaller (Le Bihan states $\frac{T}{\tau} \gtrsim 7$) than the diffusion time T, phase distributions become approximately Gaussian, as it is the case for free diffusion. The signal attenuation can in this case be described by a pseudo-diffusion coefficient $D^* = \frac{v^2\tau}{6}$, namely $F = \mathrm{e}^{-bD^*}$.

Straight flow limit When on the other hand τ becomes much larger than T, only a very small fraction of the particles changes its movement during the applications of the diffusion gradients, which is depicted in Fig. 4.1(b). Each particle acquires a phase, which is proportional to the cosine of the angle α between its movement direction and the axis of the diffusion gradients. Those angles are distributed between 0 and π with

[1] Reprinted from [5] with permission, Copyright 1988 by the Radiological Society of North America.

$\rho(\alpha) = \frac{1}{2}\sin\alpha$. Signal attenuation is then given by $F = \left|\frac{1}{2}\int_0^\pi \sin\alpha e^{icv\cos\alpha}\mathrm{d}\alpha\right|$, which evaluates to $F = |\mathrm{sinc}(c \cdot v)|$, where the velocity encoding c of the diffusion gradients is given by the first moment of the temporal diffusion gradient profile $c = \gamma\int_0^T tg^*(t)\mathrm{d}t$.

A few remarks can already be made from the two limits that have just been discussed. If the experimentally observed IVIM would be in the pseudo-diffusion limit, we would expect not to see a dependence of the attenuation F on the diffusion gradient scheme, if the b-value is kept constant. However, signal attenuation in the straight flow limit would strongly depend on the gradient scheme, in case of flow compensation ($c = 0$), no additional signal attenuation due to the blood flow would be expected. To be able to calculate the signal attenuation for the parameter range between those limits, it is necessary to have access to the distributions of particle phases, which will be the topic of the next section.

4.2 Obtaining the IVIM signal from normalized phase distributions

The basic equation to calculate the signal attenuation F of the perfusion fraction has been stated before, but is stated again to motivate this section:

$$F = \left|\left\langle e^{i\phi}\right\rangle\right| = \left|\int_{-\infty}^{\infty}\rho(\phi)e^{i\phi}\mathrm{d}\phi\right| \tag{4.2}$$

The phase ϕ which is acquired by a spin packet traveling along the path, which is given by $\mathbf{x}(t) = \mathbf{x}_0 + \int_0^t \mathbf{v}(t')\mathrm{d}t'$ in an effective magnetic field gradient $\mathbf{g}^*(t)$ during diffusion time T is given by eq. (4.3), where γ denotes the gyromagnetic ratio. Due to the rephasing condition $\int_0^T \mathbf{g}^*(t)\mathrm{d}t = 0$, which needs to be fulfilled by every diffusion weighting scheme to allow image formation (see chap. 2.2) the acquired phase is independent of the starting location $\mathbf{x_0}$ and partial integration leads to:

$$\phi = \gamma\int_0^T \mathbf{x}(t)\cdot\mathbf{g}^*(t)\mathrm{d}t = \gamma\int_0^T \mathbf{v}(t)\cdot\int_0^t \mathbf{g}^*(t')\mathrm{d}t'\mathrm{d}t. \tag{4.3}$$

In a typical diffusion experiment the diffusion sensitizing gradients are applied along a fixed direction $\mathbf{e}_g$ and have a normalized temporal profile $h(s)$ such that $\mathbf{g}^*(t) = gh(\frac{t}{T})\mathbf{e}_g$, where g is the maximum gradient amplitude. It is directly related to b via eq. (4.4), where the accumulated 0^{th} gradient moment $m_0(s) = \int_0^s h(s')\mathrm{d}s'$ was introduced:

$$b = \int_0^T\left[\gamma\int_0^t \mathbf{g}^*(t')\mathrm{d}t'\right]^2\mathrm{d}t = \gamma^2g^2T^3\int_0^1 m_0^2(s)\mathrm{d}s = a_h^2\gamma^2g^2T^3 \tag{4.4}$$

Using the abbreviation $a_h := \sqrt{\int_0^1 m_0^2(s)\mathrm{d}s}$, which summarizes the contributions of the particular shape of the temporal gradient profile $h(s)$ and relates b to the parameters γ,

T and g, which can be chosen independently of $h(s)$, we can now substitute the gradient amplitude in eq. (4.3) by b:

$$\phi = \gamma\ g\ \mathbf{e}_g \cdot \int_0^T \mathbf{v}(t) \int_0^t h\left(\frac{t'}{T}\right) \mathrm{d}t'\mathrm{d}t = \frac{\sqrt{b}}{a_h\sqrt{T}}\ \mathbf{e}_g \cdot \int_0^T \mathbf{v}(t)\ m_0\left(\frac{t}{T}\right) \mathrm{d}t. \tag{4.5}$$

We now apply the described model for particle movement, namely that the particle travels with constant speed $v = |\mathbf{v}(t)|$ and changes its direction $\mathbf{e}_v(t)$ each time the characteristic time τ passed, where the first change occurs at $t_1 = r\tau$ with $r \in (0, 1)$. We can thus split the integration in eq. (4.5) into the $M = \lceil \frac{T}{\tau} + 1 - r \rceil$ time intervals of constant movement, where $\lceil \cdots \rceil$ denotes the ceiling function, which returns the smallest integer greater or equal to the value between the brackets. The times at which the k^{th} directional change occurs are thus given by $t_k = (r + k - 1)\tau$ for $0 < k < M$, we further define $t_0 = 0$ and $t_M = T$. The velocity in this model is given by $\mathbf{v}(t) = v\ \mathbf{e}_{k(t)}$ where $\mathbf{e}_k$ is the movement direction after the k^{th} change, thus $k(t) = \lfloor |\frac{t}{\tau} - r| \rfloor$, where $\lfloor \cdots \rfloor$ denotes the floor function, which returns the largest integer smaller or equal to the value in brackets. Eq.(4.5) transforms into:

$$\phi = \frac{v\sqrt{b}}{a_h\sqrt{T}} \sum_{k=0}^{M-1} \mathbf{e_g} \cdot \mathbf{e_k} \int_{t_k}^{t_{k+1}} m_0\left(\frac{t}{T}\right) \mathrm{d}t = \frac{v\sqrt{bT}}{a_h} \sum_{k=0}^{M-1} \mathbf{e_g} \cdot \mathbf{e_k} \int_{s_k}^{s_{k+1}} m_0(s)\mathrm{d}s. \tag{4.6}$$

In the last step of eq. (4.6) the normalized times $s_k = \frac{t_k}{T}$ were introduced. The dependence of ϕ on the parameters can now be anticipated. It is possible to introduce a normalized phase ϑ which is only dependent on the temporal profile h of the diffusion gradients (denoted by the index), r and the ratio $N = \frac{T}{\tau}$:

$$\phi_h(b, v, T, \tau, r) = v\sqrt{bT}\vartheta_h(\frac{T}{\tau}, r). \tag{4.7}$$

Based on this equation the following chapter is motivated. If the distribution $\rho_{\vartheta_h}(\vartheta, N)$ of normalized phases ϑ is known for a certain gradient scheme $h(s)$ and average number of directional changes N, the distribution $\rho_{\phi_h}(\phi, N)$ of particle phases ϕ is given by

$$\rho_{\phi_h}(\phi, N) = \rho_{\vartheta_h}\left(\frac{\phi}{v\sqrt{bT}}, N\right) \cdot \frac{1}{v\sqrt{bT}}, \tag{4.8}$$

where the last factor can be omitted again, if the integration variable is changed. The signal attenuation of the perfusion fraction can thus be calculated using normalized phase distributions:

$$F_h(b, v, T, \tau) = \left| \int_{-\infty}^{\infty} \rho_{\phi_h}\left(\phi, \frac{T}{\tau}\right) \mathrm{e}^{\mathrm{i}\phi} \mathrm{d}\phi \right| = \left| \int_{-\infty}^{\infty} \rho_{\vartheta_h}\left(\vartheta, \frac{T}{\tau}\right) \mathrm{e}^{\mathrm{i}v\sqrt{bT}\vartheta} \mathrm{d}\vartheta \right| \tag{4.9}$$

The use of normalized phase distributions has the advantage that they have to be created only once for a certain diffusion gradient scheme and can then be scaled according to the sequence parameters to calculate the signal attenuation F.

4.3 Equations for generating normalized phase distributions

Motivated by eq. (4.6), we define the weighting $c_h(r+k,N)$ of the k^{th} part of particle movement. It can be shown that $c_h(r+k,N)$ does only depend on the sum of r and k:

$$c_h(r+k,N) := \frac{1}{a_h}\int_{s_k}^{s_{k+1}} m_0(s)\mathrm{d}s = \frac{1}{a_h}\int_{\min(1,\max(0,\frac{k+r-1}{N}))}^{\min(1,\frac{k+r}{N})} m_0(s)\mathrm{d}s. \tag{4.10}$$

The minimum and maximum operators in the integration limits in eq. (4.10) serve the purpose of obtaining a closed expression for c_h, which can be used also for the first and last segment of the movement. Our aim is now to derive an expression for ϑ_h, which allows one to obtain the distribution $\rho_{\vartheta_h}(\vartheta,N)$ for different N and temporal profiles $h(s)$. For isotropic distribution of velocity directions, the diffusion gradient direction can without loss of generality set to be the z-direction, thus $\mathbf{e}_g \cdot \mathbf{e}_k = z_k$, where $z_k = \cos\theta$ is the z-component of the kth velocity direction. Since the distribution of angles $\theta \in (0,\pi)$ is proportional to $\sin\theta$, the normalized distribution $\rho_\theta(\theta)$ is given by $\rho_\theta(\theta) = \frac{1}{2}\sin\theta$. We show now, that z_k is homogeneously distributed by calculating the transformation equation, which allows one to generate a random variable θ following the distribution $\rho_\theta(\theta)$ from a homogeneously distributed random variable $w \in (-1,1)$. To accomplish this goal, eq.(4.11), which allows to relate the two probability distributions, needs to be solved for θ:

$$P(\theta' < \theta) = \int_0^\theta \rho(\theta')\mathrm{d}\theta' = \int_{-1}^{w} \rho_w(w')\mathrm{d}w' = P(w' < w). \tag{4.11}$$

Since $\rho_w(w) = \frac{1}{2}$ for $w \in (-1,1)$, eq. (4.11) yields $w = -\cos\theta = -z_k$, leading to the conclusion that $z_k \in (-1,1)$ is homogeneously distributed for isotropically distributed directions $\mathbf{e}_k$. $\vartheta_h(N,r)$ can thus be identified as a weighted sum of homogeneously distributed random variables z_k:

$$\vartheta_h(N,r) = \sum_{k=0}^{\lceil N\rceil} z_k c_h(r+k,N). \tag{4.12}$$

Eq. (4.12) was used to create the normalized phase distributions. For 1024 values of N, $64\cdot 10^6$ tuples of random variables $(r, z_0, \ldots, z_{\lceil N\rceil})$ were generated and the phase distributions obtained as a histogram of the phases ϑ_h resulting from the tuples. From eq. (4.12) it becomes also clear, that the maximum phase a particle could acquire with a particular r is given by $\vartheta_{\max} = \sum_{k=0}^{\lceil N\rceil} |c_h(r+k,N)|$ and that the distribution of normalized phases is symmetric: $\rho_{\vartheta_h}(\vartheta,N) = \rho_{\vartheta_h}(-\vartheta,N)$. We can further deduce the distribution of normalized phases for large N. Since $\rho_{\vartheta_h}(\vartheta,N)$ can be considered a weighted sum of many random variables z_k, each of which is distributed homogeneously with zero mean and standard deviation $\sigma_k = \sqrt{\frac{1}{3}}$, the central limit theorem can be applied and the

distribution $\rho_{\vartheta_h}(\vartheta, N)$ can for large N be approximated by a Gaussian distribution with zero mean and $\sigma = \frac{\sigma_k}{\sqrt{N}}$:

$$\lim_{N\to\infty} \rho_{\vartheta_h}(\vartheta, N) = \sqrt{\frac{3N}{2\pi}} \cdot \mathrm{e}^{-\frac{3N}{2}\vartheta^2} \tag{4.13}$$

In the following it is shown that only phase distributions for $N \geq 1$ need to be generated, since those for $N < 1$ can be calculated as a linear combination of $\rho_{\vartheta_h}(\vartheta, 0)$ and $\rho_{\vartheta_h}(\vartheta, 1)$, for which analytic formulas can be derived. Since the random variables z_k (corresponding to the z-component of the k^{th} velocity direction) are independent of each other, an analytical expression could eventually be obtained by integration over all random variables and their respective distributions (where δ denotes the δ-distribution):

$$\rho_{\vartheta_h}(\vartheta, N) = \int_0^1 \int_{-1}^1 \cdots \int_{-1}^1 \rho_r(r)\rho_{z_0}(z_0) \cdots \rho_{z_{\lceil N\rceil}}(z_{\lceil N\rceil}) \\ \delta(\vartheta - \sum_{k=0}^{\lceil N\rceil} z_k c_h(r+k, N))\ \mathrm{d}z_{\lceil N\rceil} \cdots \mathrm{d}z_0\ \mathrm{d}r. \tag{4.14}$$

In the above equation the distributions of the random variables are given by $\rho_r(r) = 1$ and $\rho_{z_0}(z_0) = \cdots \rho_{z_{\lceil N\rceil}} = \frac{1}{2}$. While the efforts required to obtain analytic expressions from eq. (4.14) strongly increase with N, the just described process of generating normalized phase distributions from simulations facilitates with increasing N. Therefore in the remainder of this section, only the case of $N \leq 1$ is discussed.

The case $N \leq 1$: Eq. (4.14) simplifies to:

$$\rho_{\vartheta_h}(\vartheta, N) = \frac{1}{4} \int_0^1 \int_{-1}^1 \int_{-1}^1 \delta\left[\vartheta - z_0 c_h(r, N) - z_1 c_h(r+1, N)\right]\ \mathrm{d}z_1 \mathrm{d}z_0\ \mathrm{d}r. \tag{4.15}$$

For $N \leq 1$ a particle changes its direction at most once during the diffusion experiment. The parameter r indicates whether this is the case ($r < N$) or not. If there is no directional change ($r \geq N$), eq. (4.10) yields $c_h(r+1, N) = 0$ and $c_h(r, N) =: d$ becomes independent of r and N. This is used to evaluate eq. (4.15). The integration over r is splitted into two parts, where the first term in eq. (4.16) corresponds to $r \geq N$. For the second term integration over z_1 is performed, where the δ-distribution is eliminated with the help of the heaviside function $\Theta(x)$:

$$\rho_{\vartheta_h}(\vartheta, N) = \frac{1-N}{2} \int_{-1}^1 \delta(\vartheta - z_0 d)\ \mathrm{d}z_0 \\ + \frac{1}{4} \int_0^N \frac{1}{|c_h(r+1, N)|} \int_{-1}^1 \Theta\left(1 - \left|\frac{\vartheta - z_0 c_h(r, N)}{c_h(r+1, N)}\right|\right) \mathrm{d}z_0\ \mathrm{d}r. \tag{4.16}$$

For flow compensated gradients the 1st moment of the temporal gradient profile is zero, which is equivalent to $d = 0$:

$$\int_0^1 sh(s)\mathrm{d}s = -\int_0^1 \int_0^s h(s')\mathrm{d}s'\mathrm{d}s = -d \tag{4.17}$$

In this case the first integral in eq. (4.16) evaluates to $2\delta(\vartheta)$, whereas for a not flow compensated gradient profile ($|d| > 0$) we obtain a constant offset to the phase distribution: $\frac{1}{|d|}\Theta\left(1 - \left|\frac{\vartheta}{d}\right|\right)$. The second part in eq. (4.16) can be rewritten by replacing the integral over the heaviside function with the help of minimum operators:

$$\rho_{\vartheta_h}(\vartheta, N) = \frac{1-N}{2}\int_{-1}^{1}\delta(\vartheta - z_0 d)\ \mathrm{d}z_0 + \int_0^N \Theta(|c_h(r,N)| + |c_h(r+1,N)| - |\vartheta|) \cdot \frac{\min(|c_h(r,N)|, |c_h(r+1,N)| + |\vartheta|) + \min(|c_h(r,N)|, |c_h(r+1,N)| - |\vartheta|)}{4|c_h(r,N)c_h(r+1,N)|}\ \mathrm{d}r. \tag{4.18}$$

The weights $c_h(r+k, N)$ for the second term (where $r \leq N$) can be shown to depend only on the ratio $\frac{r}{N}$ and we rewrite $c_0(\frac{r}{N}) := c_h(r,N) = \frac{1}{a_h}\int_0^{r/N} m_0(s)\mathrm{d}s$ and $c_h(r+1,N) = \frac{1}{a_h}\int_{r/N}^1 m_0(s)\mathrm{d}s = d - c_0(\frac{r}{N})$. Substitution of $r = \frac{r}{N}$ leads to eq. (4.19):

$$\rho_{\vartheta_h}(\vartheta, N) = \frac{1-N}{2}\int_{-1}^{1}\delta(\vartheta - z_0 d)\ \mathrm{d}z_0 + \frac{N}{4}\int_0^1 \Theta(|c_0(r)| + |d - c_0(r)| - |\vartheta|) \cdot \frac{\min(|c_0(r)|, |d - c_0(r)| + |\vartheta|) + \min(|c_0(r)|, |d - c_0(r)| - |\vartheta|)}{|c_0(r)(d - c_0(r))|}\ \mathrm{d}r. \tag{4.19}$$

The fact that the second integral in eq. (4.19) doesn't depend on N anymore, allow us to rewrite any phase distribution for $N \leq 1$ as follows:

$$\rho_{\vartheta_h}(\vartheta, N) = (1-N)\rho_{\vartheta_h}(\vartheta, 0) + N\rho_{\vartheta_h}(\vartheta, 1). \tag{4.20}$$

Depending on whether (FC) or not (NFC) the gradient profile h is flow compensated, $\rho_{\vartheta_h}(\vartheta, 0)$ is given by:

$$^{FC}\rho_{\vartheta_h}(\vartheta, 0) = \delta(\vartheta) \tag{4.21a}$$

$$^{NFC}\rho_{\vartheta_h}(\vartheta, 0) = \frac{1}{2|d|}\Theta\left(1 - \left|\frac{\vartheta}{d}\right|\right) \tag{4.21b}$$

From eq. (4.21) it becomes apparent, that in the straight flow limit without directional changes $\rho_{\vartheta_h}(\vartheta, 0)$ is given by a δ-distribution for flow compensated gradients and by a constant distribution for non-flow compensated gradients, where the minimum and maximum attainable phases are given by $-|d|$ and $|d|$ respectively. The equations for

$\rho_{\vartheta_h}(\vartheta, 1)$ are more complicated, since they depend on the exact timing of the diffusion gradient scheme:

$$^{FC}\rho_{\vartheta_h}(\vartheta, 1) = \int_0^1 \Theta(2|c_0(r)| - |\vartheta|)\frac{2|c_0(r)| - |\vartheta|}{4c_0^2(r)}\mathrm{d}r \tag{4.22a}$$

$$^{NFC}\rho_{\vartheta_h}(\vartheta, 1) = \int_0^1 \Theta(|c_0(r)| + |d - c_0(r)| - |\vartheta|) \cdot \frac{\min(|c_0(r)|, |d - c_0(r)| + |\vartheta|) + \min(|c_0(r)|, |d - c_0(r)| - |\vartheta|)}{4|c_0(r)(d - c_0(r))|}\,\mathrm{d}r \tag{4.22b}$$

4.4 Normalized phase distributions for different gradient profiles

In this section phase distributions $\rho_{\vartheta_h}(\vartheta, N)$ for different diffusion weighting profiles are compared and some analytic results presented. While the focus will be on bipolar and flow compensated profiles first (4.4.1), findings for oscillating gradients are presented at the end of the section (4.4.2).

To achieve a diffusion weighting, a variety of different gradient profiles can be inserted into the MRI sequence. The most commonly used profile is the 'bipolar' scheme, which has already been employed by Stejskal and Tanner in 1965 [47]. It has the advantage, that it achieves the highest b-values for a given diffusion time T and maximum gradient amplitude $g_{\max}$. There are two typical implementations of this gradient profile: The monopolar profile, where the two gradient lobes are placed before and after a refocussing pulse, where they must have the same sign to fulfill the rephasing condition and the bipolar profile, where typically two refocussing pulses are employed. The latter one has the advantage, that it is possible to adjust the sequence timing to strongly suppress eddy currents [31] and is therefore the most widely employed one. For the application studied in the work at hand it was however found, that concomitant fields had a much larger impact on image quality (see 3.4). Since the concomitant field effect of a diffusion weighting scheme, which is symmetrically placed around a refocussing pulse, cancel out [9], p. 292ff., all experimental results shown in chapters 5 - 6 were obtained using symmetric diffusion profiles, such as the monopolar one. The use of flow compensated diffusion gradients was first suggested by Maki [48] to separate diffusion and microcirculatory flow. The most simple gradient waveform which achieves nulling of the first gradient moment is the one shown in Fig. 4.2 labeled 'flow compensated'. It is sometimes referenced as field even echo refocussing (FEER) waveform [49]. While it allows one to achieve the highest b-value for given T and $g_{\max}$ while keeping the first gradient moment nulled, it is prone to concomitant field artifacts (see 3.4). This can be account for by using the 'flowcomp+' profile, shown in Fig. 4.2.

Another group of diffusion weighting profiles, which is widely used, is the group of oscillating gradient profiles. These have first been suggested by Stepišnik [36] and allow

one to probe the spectrum of the diffusion tensor. For that reason, measuring diffusion using oscillating gradients is sometimes referred to as *Temporal diffusion spectroscopy*. Since the coils used for applying magnetic field gradients are affected by the electromagnetic law of induction, ramping from 0 to $g_{\max}$ can not be done arbitrary fast. Therefore the first and last halves of the cosine lobes are usually replaced by a sine lobe of twice the frequency, yielding the 'cosine+' gradient scheme shown in Fig. 4.2.

The equations defining the normalized gradient profiles used in this work are stated below (eq. (4.23a) - (4.23f), where the letter Q specifies the number of oscillations for sine and cosine gradients:

$$\text{bipolar}: \quad h(s) = \begin{cases} -1 & s < \frac{1}{2} \\ 1 & \text{else} \end{cases} \tag{4.23a}$$

$$\text{flowcomp}: \quad h(s) = \begin{cases} 1 & s < \frac{1}{4} \\ -1 & \frac{1}{4} \leq s < \frac{3}{4} \\ 1 & \text{else} \end{cases} \tag{4.23b}$$

$$\text{flowcomp+}: \quad h(s) = \begin{cases} -1 & s < \frac{1}{2} - \frac{\sqrt{2}}{4} \\ 1 & \frac{1}{2} - \frac{\sqrt{2}}{4} \leq s < \frac{1}{2} \\ -1 & \frac{1}{2} \leq s < \frac{1}{2} + \frac{\sqrt{2}}{4} \\ 1 & \text{else} \end{cases} \tag{4.23c}$$

$$\text{sine}: \quad h(s, Q) = -\sin(2\pi Q s) \tag{4.23d}$$

$$\text{cosine}: \quad h(s, Q) = \cos(2\pi Q s) \tag{4.23e}$$

$$\text{cosine+}: \quad h(s, Q) = \begin{cases} -\sin(4\pi Q s) & x < \frac{1}{4Q} \\ -\cos(2\pi Q s) & \frac{1}{4Q} \leq x < \frac{1}{2} - \frac{1}{4Q} \\ \sin(4\pi Q s) & \frac{1}{2} - \frac{1}{4Q} \leq x < \frac{1}{2} + \frac{1}{4Q} \\ \cos(2\pi Q s) & \frac{1}{2} + \frac{1}{4Q} \leq x < 1 - \frac{1}{4Q} \\ -\sin(4\pi Q s) & \text{else} \end{cases} \tag{4.23f}$$

4.4.1 Bipolar and flow compensated gradients

Normalized phase distributions for bipolar and flowcomp+ gradient profiles are shown in Fig. 4.3. While for large N, phase distributions become similar and approach the diffusion limit (eq. (4.13)), the distributions differ clearly for small N. Note that the maximum phase that a particle can accumulate for $N = 0$ in the bipolar case is given by $|d| = \frac{\sqrt{3}}{2}$. A normalized apparent diffusion coefficient $\frac{\mathrm{ADC}}{Tv^2}$ can be defined for normalized phase distributions as the limit for small b-values, where we recall how the signal attenuation of the perfusion fraction can be calculated from the phase distributions (eq.

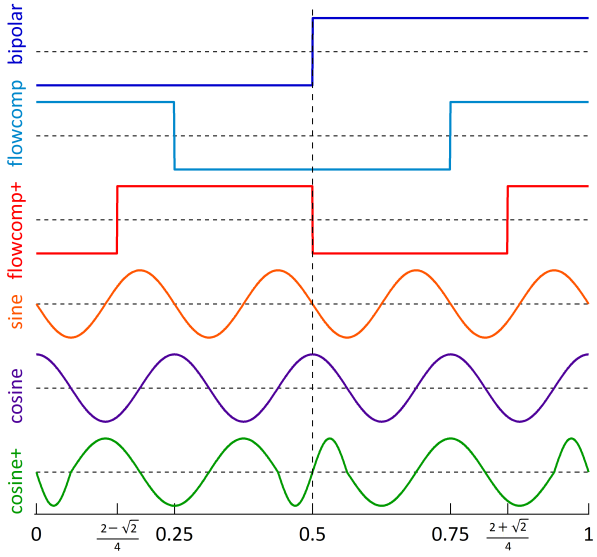

Figure 4.2: Gradient profiles for which normalized phase distributions were generated. While the bipolar and sine profile are not flow compensated, the flowcomp and cosine profile are. The symmetry of the '+'-profiles allows implementation into a MRI sequence with full compensation for concomitant fields (see 3.4).

(4.9)):

$$\mathrm{ADC} := \lim_{b\to 0} \frac{-1}{b} \ln(F(b,v,T,\tau)) = \lim_{b\to 0} \frac{-1}{b} \ln \left| \langle \mathrm{e}^{iv\sqrt{bT}\vartheta_h} \rangle \right| \tag{4.24}$$

Using the symmetry of the phase distributions we can replace the exponential by a cosine function. The absolute value function can also be omitted in the limit of small b. Applying l'Hôpital's rule yields:

$$\mathrm{ADC} = \langle - \lim_{b\to 0} \frac{\ln(\cos(v\sqrt{bT}\vartheta_h))}{b} \rangle = \frac{v\sqrt{T}}{2} \langle \lim_{b\to 0} \frac{\sin(v\sqrt{bT}\vartheta_h)}{\sqrt{b}} \vartheta_h \rangle = Tv^2 \langle \frac{\vartheta_h^2}{2} \rangle \tag{4.25}$$

The normalized ADC for monopolar and flow compensated profiles is shown as a function of N in Fig. 4.4. As one could already expect from the normalized phase distributions shown in Fig. 4.3, two regimes can be distinguished: For $N \gg 1$, the signal attenuation and thus the apparent diffusion coefficients become similar as phase distributions approach the Gaussian distribution. For $N \lesssim 1$ signal attenuation for flow compensated and bipolar gradients can be expected to be different. Also a dependence on N, which can be changed by varying the diffusion time T should be observable, especially for the flow compensated gradient profiles.

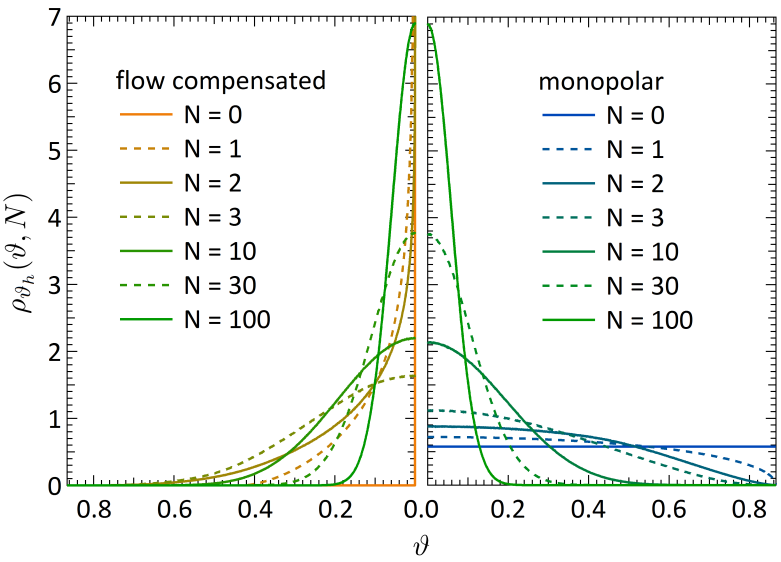

Figure 4.3: Normalized phase distributions for bipolar and flowcomp+ gradient profiles. While for large N, phase distributions approach the Gaussian limit for both gradient profiles, phase distributions differ strongly for small N.

4.4.2 Oscillating gradients

Analogous to the bipolar / flow compensated gradients, phase distributions can also be obtained for oscillating gradient profiles. Normalized phase distributions are shown for both sine and cosine profiles in Fig. 4.5 (4 oscillations) and Fig. 4.6 (16 oscillations). The phase distributions for sine gradients appear very similar to the bipolar distributions except for the maximum phase being $|d| = \sqrt{\frac{2}{3}} < \frac{\sqrt{3}}{2}$, also the change in oscillation number does not reflect in the shape of the phase distributions. In contrast, the phase distributions for cosine gradients become narrower with increasing number of oscillations Q. Also for larger Q, the sine and cosine distributions for larger N are less similar, which can e.g. be anticipated, if the distributions for $N = 10$ are compared in Fig. 4.5 and 4.6. The difference in phase distributions for $N = 10$ is not as pronounced for bipolar and flow compensated gradients in Fig. 4.3, which can be explained as follows: While the 1$^{\text{st}}$ moment is nulled for flow compensated gradients on timescale T, this timescale reduces for cosine gradients to $\frac{T}{Q}$, yielding an effective ratio $N_{\text{eff}} = \frac{N}{Q}$. Therefore the phase distributions for $N = 100$ have still not fully reached the Gaussian limit for the cosine gradients with 16 oscillations in Fig. 4.6. Based on the obtained phase distributions, normalized apparent diffusion coefficients can also be calculated for oscillating gradients. The results are shown in Fig. 4.7. For large N, normalized sine and cosine ADCs are similar, although no dependence on the number of oscillations is visible. While sine ADCs

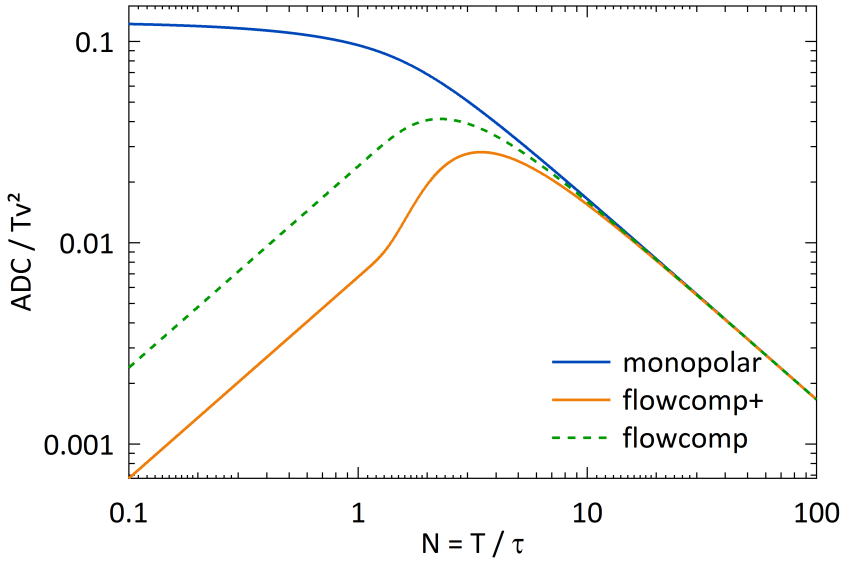

Figure 4.4: Normalized ADC for monopolar and flow compensated gradient profiles as a function of N. If the timescale of the incoherent motion is much smaller than the duration of the diffusion experiment ($N \gg 1$), the attenuation becomes independent of the profile, whereas differences are to be expected for $N \lesssim 1$.

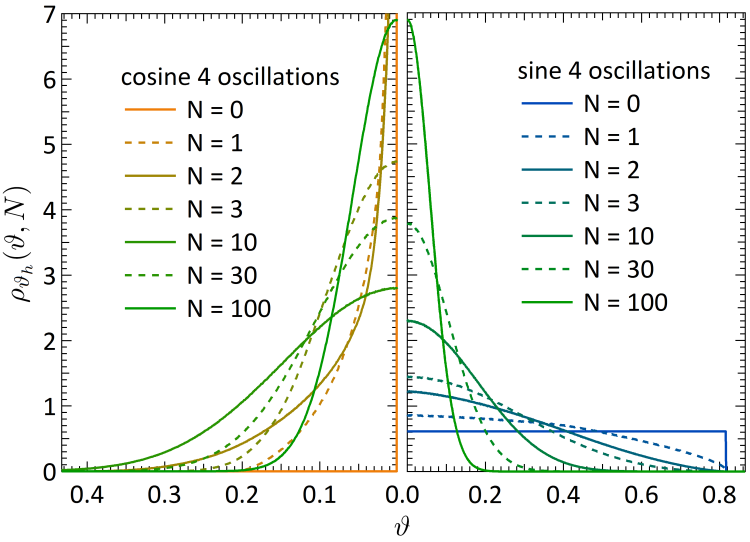

Figure 4.5: Normalized phase distributions for sine and cosine gradient profiles with 4 oscillations. The horizontal axis is stretched for cosine gradients, since distributions are much narrower. Cosine distributions appear similar to flow compensated ones, while sine distributions appear similar to bipolar ones.

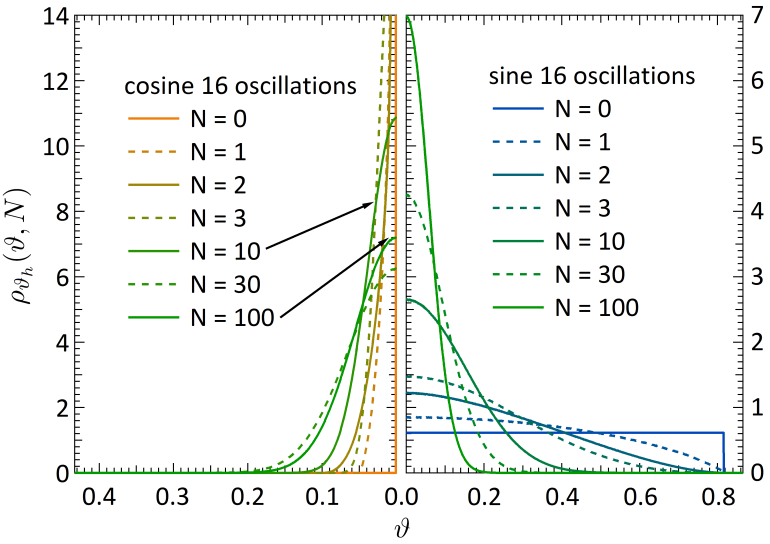

Figure 4.6: Normalized phase distributions for sine and cosine gradient profiles with 16 oscillations. While the sine distributions do not show large changes with oscillation number, the cosine distributions are much narrower than those for 4 oscillations shown in Fig. 4.5. Both cosine axis are stretched.

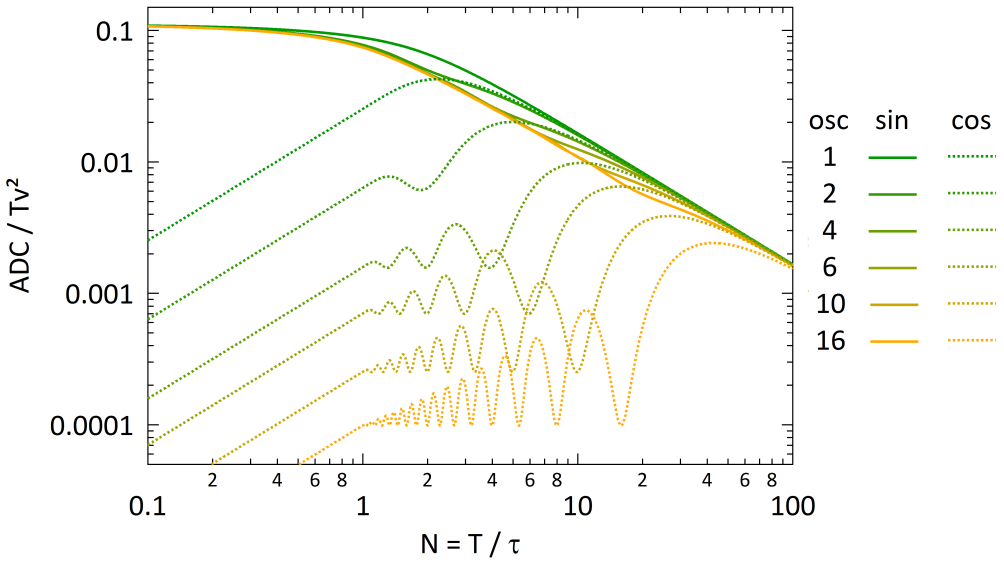

Figure 4.7: Normalized ADC for sine and cosine gradient profiles with varying number of oscillations. While the ADC for sine gradients is largely independent of oscillation number, the cosine ADC decreases with oscillation number. Also oscillations in N are visible for the cosine ADC.

do not differ very much with oscillation number and resemble the behaviour which was found for the bipolar profile in Fig. 4.4, cosine ADCs differ substantially. For $Q = 1$ and $Q = 2$, curves resemble the flowcomp, respectively flowcomp+ profiles, whereas the ADC curves also show oscillations in N where the number of minima is given by $Q - 1$, which are located at $N_k = \frac{Q}{k}$ where $k = 1, 2, ..., Q-1$. Those oscillations can be explained from the spectrum of the velocity autocorrelation function for intra-voxel incoherent motion (Fig. 3.4). The cosine profile probes the spectrum essentially at $\omega = \frac{2\pi Q}{T}$ [33] and from Fig. 3.4, minima of the normalized ADC would be expected if $\frac{\tau\omega}{2\pi}$ is an integer k. This yields $\frac{Q}{T} = \frac{k}{\tau}$, from which the relation of the minima at $N_k = \frac{Q}{k}$ becomes apparent.

4.5 Modeling the diffusion coefficient of blood

With the phase distributions for different gradient profiles at our disposal, the only missing ingredient to calculate the signal attenuation in the IVIM model according to eq. (4.1) is the diffusion coefficient of blood D_b. Here we follow the approach of Henkelman *et.al*. [44,45] to describe the water dynamics of blood by a three compartment model. As depicted in Fig. 4.8, water molecules can be diffusing inside red blood cells (pool B), in plasma (P) or part of macromolecules (M). Each pool is associated with a characteristic

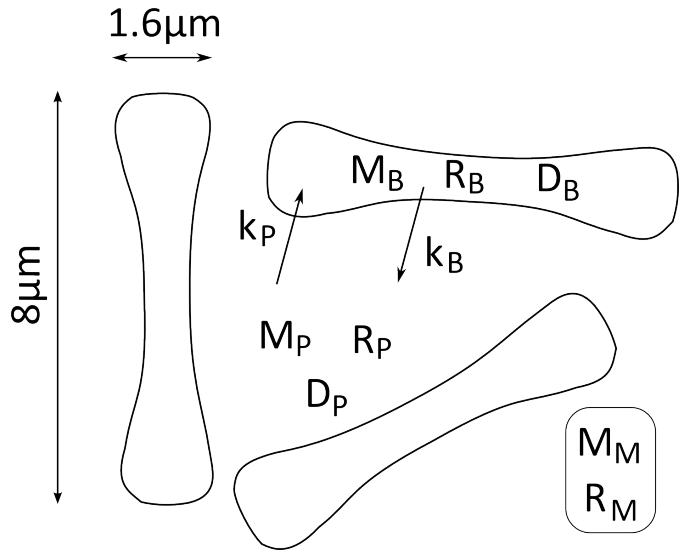

Figure 4.8: Blood as a three-compartment model. While exchange and diffusion in the macromolecular pool (M) can be neglected, water in red blood cells (B) heavily exchanges with plasma (P). Magnetization is distributed according to the fractions M_i (after [44]).

diffusion coefficient D_i and relaxation rate R_i, whereas M_i denotes the total fraction of the equilibrium magnetization. The exchange between the pools is governed by the exchange rates k_B and k_P For the initial state of the system, the equilibrium condition (eq. (4.26a)) and the normalization (eq. (4.26b)) hold.

$$k_B M_B(0) = k_P M_P(0) \tag{4.26a}$$

$$M_B(0) + M_P(0) + M_M(0) = 1 \tag{4.26b}$$

The time-evolution of the magnetization is described by eq. (4.27a) - (4.27c) [44].

$$\frac{\mathrm{d}M_B}{\mathrm{d}t} = -\frac{\mathrm{d}b}{\mathrm{d}t} D_B^{\mathrm{APP}} M_B - R_B M_B - k_B M_B + k_P M_P \tag{4.27a}$$

$$\frac{\mathrm{d}M_P}{\mathrm{d}t} = -\frac{\mathrm{d}b}{\mathrm{d}t} D_P^{\mathrm{APP}} M_P - R_P M_P - k_P M_P + k_B M_B \tag{4.27b}$$

$$\frac{\mathrm{d}M_M}{\mathrm{d}t} = -R_M M_M \tag{4.27c}$$

$$\tag{4.27d}$$

According to [44], exchange with the macromolecular pool can be neglected. The typical diffusion coefficients of macromolecules, such as fat, are due to the larger molecular size several orders of magnitude smaller [50] than those for protons in water, such that diffusion can also be omitted for the macromolecules. For calculating the apparent diffusion coefficient of blood, we use the values specified in [45] for body temperature (37°C): $R_B = 7.1\ \mathrm{s}^{-1}$, $R_P = 1.3\ \mathrm{s}^{-1}$, $R_M = 286\ \mathrm{s}^{-1}$, $k_B = 82\ \mathrm{s}^{-1}$, $M_B = 0.34$, $M_M = 0.14$ and $D_P^{\mathrm{APP}} = 2.3\ \mu\mathrm{m}^2/\mathrm{s}^{-1}$. Those values were a result of the model fit to experimental CPMG data acquired from heparinized human blood [45].The remaining necessary parameter, the apparent diffusion coefficient for red blood cells D_B^{APP}, however, is more intricate to determine.

Using the multiple correlation function (MCF) tool, which was developed in the diffusion group at the German Cancer Research center, the apparent diffusion coefficient in red blood cells was calculated for several gradient schemes. The multiple correlation functions approach was worked out in great detail by Grebenkov [51–53]. It allows to compute the diffusion weighted signal in the presence of a restricting boundary, if the eigenfunctions of the Laplace operator are known for the confining geometry. Its huge advantage is, that it can achieve a given precision much faster than other algorithms, e.g. Monte-Carlo simulations.

To calculate D_B^{APP}, free diffusion coefficient $D_b = 0.76\ \mu\mathrm{m}^2/ms$ and dimension $a = 7.6\mu\mathrm{m}$ of the confining geometry were used from [44]. The confining geometry 'slab' was chosen and number of data points and eigenvalues in the MCF tool was set to 1000. Setting the diffusion time $T = 0.12$ s yields the results shown in Fig. 4.9.

To obtain a value for D_b, the time-evolution of the magnetization in the different pools (eq. (4.27a) - (4.27c)) was evaluated stepwise using MATLAB. For each of the $N_s = 1000$ steps during the diffusion experiment, a particle would either change the pool with the respective probabilities given by eq. (4.28a) and (4.28b) or stay.

$$w_B = 1 - \mathrm{e}^{-\frac{k_B T}{N_s}} \tag{4.28a}$$

$$w_P = 1 - \mathrm{e}^{-\frac{k_P T}{N_s}} \tag{4.28b}$$

In this calculation, the time where no diffusion gradients were active was also considered. Between time $t = 0$ and $t = \frac{\mathrm{TE}-T}{2}$ no diffusion gradients are active and the system

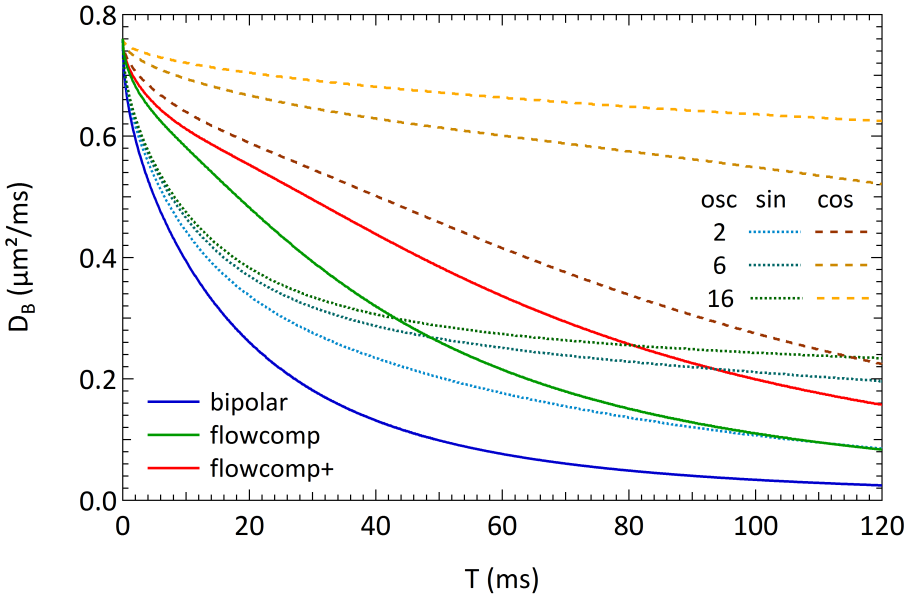

Figure 4.9: Apparent diffusion coefficient of water in red blood cells as a function of gradient profile and diffusion time T. Results were obtained using the MCF tool, where $D_b = 0.76\ \mu\mathrm{m}^2/ms$, $T = 0.12$ s and the parameters *data points* and *eigenvalues* set to 1000.

undergoes only relaxation and exchange. The same is the case for the time between $t = \frac{\mathrm{TE}+T}{2}$ and $t = \mathrm{TE}$. In case a particle would change its pool, the signal attenuation by both diffusion and T_2-relaxation, that it would have accumulated during the residence time in that pool, is noted. The attenuation due to diffusion is calculated using $\frac{\mathrm{d}b}{\mathrm{d}t} = b\frac{r_s}{N_s}$, where r_s is the number of steps the particle resided in the pool before leaving it. For D_B^{APP} the values obtained from the MCF tool (Fig. 4.9) are used. The resulting apparent diffusion coefficients of blood, which are dependent on both gradient profile and b-value are shown in Fig. 4.10. D_b is slightly higher for the flowcomp+ profile than for the

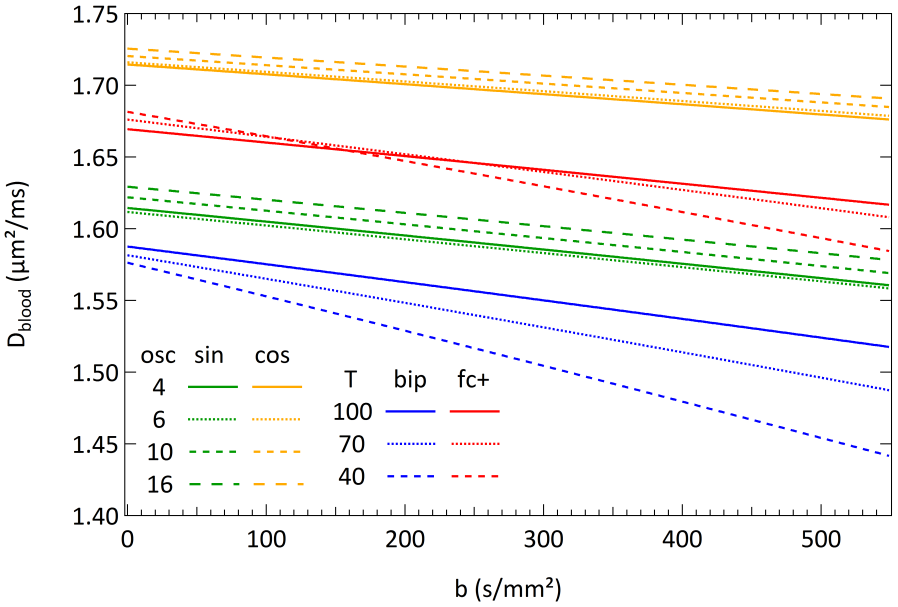

Figure 4.10: Apparent diffusion coefficient of water in blood as a function of gradient profile and b-value for the combinations used in the experiments. Diffusion time T for the oscillating schemes was 120 ms. Echo time was TE = 120 ms of bipolar and flowcomp+ schemes and 140 ms for oscillating gradients

bipolar gradients. Also a T-dependence is visible, which is for the flow compensated gradients presumably suppressed by the additional time without diffusion gradients in case of smaller T. The simulated apparent diffusion coefficient of blood is higher for cosine gradients than for sine gradients, while a small dependence on the oscillation number Q is visible.

5 Results: Bipolar vs. flow compensated gradients

In this chapter experimental data is presented, which was acquired using the Maxwell-compensated diffusion sequence introduced in section 3.4. After a description of the data acquisition protocol, a region-of-interest (ROI) based evaluation of the diffusion weighted signal in strongly perfused abdominal organs is performed (section 5.2.1). The IVIM model, which was in detail explained in chapter 4 is used to describe the measured data and extract information on microscopic parameters. It is found that assuming a single microscopic velocity v (basic model) leads to oscillations in the model attenuation curves for bipolar gradients. Since these oscillations are not found *in vivo*, suggestions for velocity distributions are discussed (section 5.2.3 - 5.2.5) and tested based on the obtained liver and pancreas data. A parabolic velocity distribution such as the laminar flow profile is found most suited (section 5.2.6) and used in the remainder of the presented work. Parameter maps of the IVIM model parameters are obtained by pixel-wise fitting and shown in section 5.3.

5.1 Data acquisition protocol

Abdominal diffusion weighted MRI of 6 healthy volunteers (age 19-31) at a magnetic field strength of $B_0 = 1.5$ T (Siemens Magnetom Avanto) using body and spine matrix. Acquisition parameters were TR = 2.1 s, TE = 120 ms, in plane resolution 3.5×3.5 mm^2 with a matrix size of 100×78. All images were acquired using the diffusion weighting sequence described in 3.4, where the EPI readout bandwidth was 2000 Hz/px. During each TR, images for 9 non-overlapping slices were obtained in interleaved order, where slice thickness was 5 mm and spacing between slices was 1 mm. Images were acquired in expirational breath hold such that after an initial dummy scan, which was performed to allow the magnetization reach equilibrium state, a prescan to adjust the GRAPPA [30] factors for reconstruction was performed. Acquisition was accelerated by a factor of 2 in phase encoding direction and a partial Fourier factor of 6/8 was used. During each breath hold, 3 unweighted (b_0) images and 12 diffusion weighted images (2 different b-values and 6 different diffusion gradient directions) were acquired, yielding a total breath hold duration of $(2 + 3 + 12) \cdot 2.1$ s = 35.7 s. For each volunteer, one slice was selected, for which the obtained images showed intersections of the abdominal organs pancreas, liver, kidney and spleen. Fig. 5.1 shows typical unweighted (Fig. 5.1(a))

and diffusion weighted (Fig. 5.1(b)) images. In Fig. 5.1(a) the evaluated ROIs for liver (yellow), pancreas (red), renal cortex (blue) and spleen (green) are displayed. In addition to the b-values, both diffusion time T and gradient profile were varied. Monopolar and flowcomp+ profiles were used at diffusion times $T = 40$ ms, 70 ms and 100 ms. Measured b-values for each profile / time combination were 10, 25, 50 and 100 s/mm^2. For the two larger diffusion times, images at $b = 200$, 300, 400 and 500 s/mm^2 could additionally be obtained.

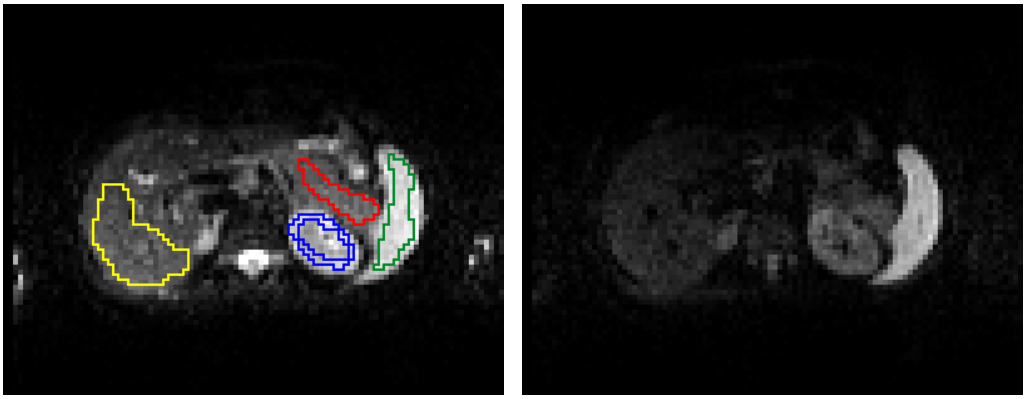

(a) $b = 0$ s/mm^2 **(b)** $b = 300$ s/mm^2

Figure 5.1: Example images for 2 different b-values. Rois for liver (yellow), pancreas (red), renal cortex (blue ring) and spleen (green) are shown. The in-plane resolution is 3.5×3.5 mm^2 at a matrix size of 100×78. Gradient profile was flowcomp+ at $T = 70$ ms. Images were acquired using TE = 120 ms and TR = 2.1 s in expirational breath hold and are using the same intensity scaling.

5.2 ROI-wise evaluation

In this section, the results based on ROI-wise evaluation for the different abdominal organs are presented. After a short description of the averaging process and display of the experimentally obtained data (section 5.2.1), the IVIM model as described in chapter 4 (basic model) is then fitted to the data to obtain estimates for the microscopic parameters v and τ. To eliminate the oscillations in the bipolar model attenuation curves, which were found to be a consequence of assuming only one velocity for the incoherent motion, different velocity distributions are discussed, which are motivated by literature [54].

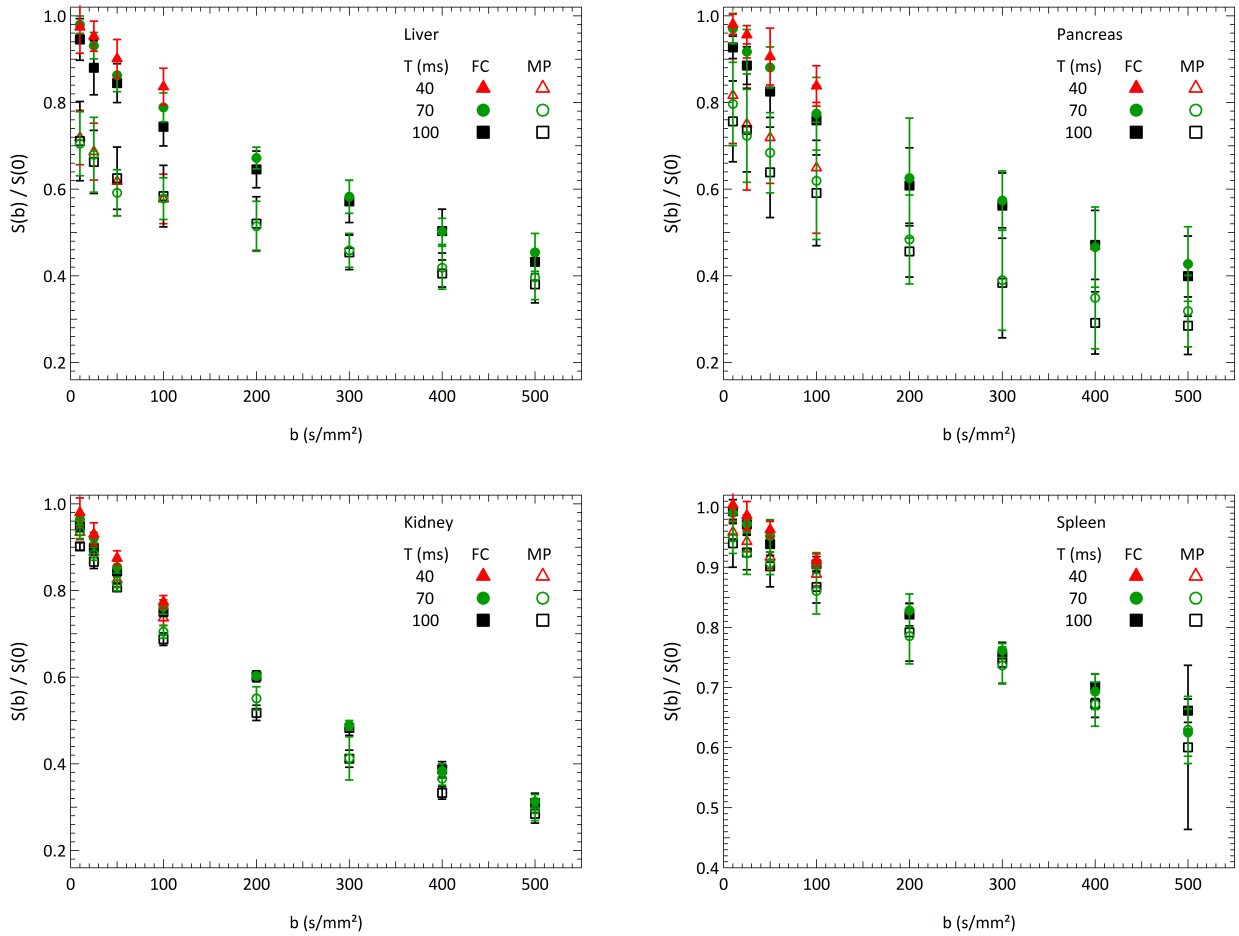

Figure 5.2: Flow compensated (FC) and monopolar (MP) signal attenuation for different abdominal organs. FC and MP curves show huge differences for liver and pancreas (top), also a dependence on the diffusion time T is observable. For kidney and spleen (bottom), effects are much less pronounced, but can still be noticed.

5.2.1 Measured signal for different abdominal organs

As a first step, trace-weighted images were obtained by taking the geometric mean of the signal intensities for different diffusion directions for each pixel. Then averaging of the signal intensities within a region of interest was performed. Figure 5.2 shows the obtained data for different abdominal organs, where the error bars denote the standard deviation of the values of the different subjects. The signal is normalized to the ROI intensity of the mean b_0 image. For liver and pancreas (top row in Fig. 5.2), signal attenuation is much larger for monopolar gradients than for flow compensated gradients. Moreover an increase in signal attenuation with diffusion time T can be observed for the flow compensated profile at low b-values. Those two effects are to some extent also present in kidney and spleen (bottom row in 5.2), but are obscured by signal variance and thus cannot be as readily perceived as for liver and pancreas. In the following sections, the attempt will be made to extract information on the microscopic parameters τ and v by fitting the model described in chapter 4 to the experimentally obtained liver and pancreas data.

5.2.2 Basic model

The normalized phase distributions, which were generated as described in 4.3 allow to calculate the signal attenuation F of the perfusion compartment for flow compensated and monopolar gradients for a given set of parameters T, b, τ and v using eq. (4.9). Together with the precalculated apparent diffusion coefficient of blood D_{blood} (see Fig. 4.10 and section 4.5 for details), the diffusion coefficient D of the tissue fraction and the perfusion fraction f, this allows to calculate the signal attenuation in the IVIM model according to eq. (5.1) where S_0 denotes the unweighted signal and D_{blood} and F are dependent on the gradient profile:

$$\frac{S(b,T,f,D,\tau,v)}{S_0} = (1-f)\mathrm{e}^{-bD} + f\mathrm{e}^{-bD_{\text{blood}}(b,T)}F(b,T,\tau,v), \tag{5.1}$$

Using MATLAB's *lsqnonlin*, a least-squares fitting of eq. (5.1) to the experimentally obtained signal intensities was performed. For the 40 different measured combinations of b, T and gradient profile, the 4 free fit parameters are D, f, τ and D^*, which is related to v by $D^* = \frac{v^2\tau}{6}$. Fig. 5.3 shows the results for liver and pancreas. The fit errors stated for the free parameters correspond to the 95% confidence intervals that were obtained from the Jacobian matrix of the residual function for the best fit using MATLAB's built-in function *nlsparci*. Several important aspects can be identified from the fitting results shown in Fig. 5.3

- The model can well describe the different signal attenuation for flow compensated and monopolar gradients and also resolve the dependence of the flow compensated signal attenuation on T (see liver data, bottom left).

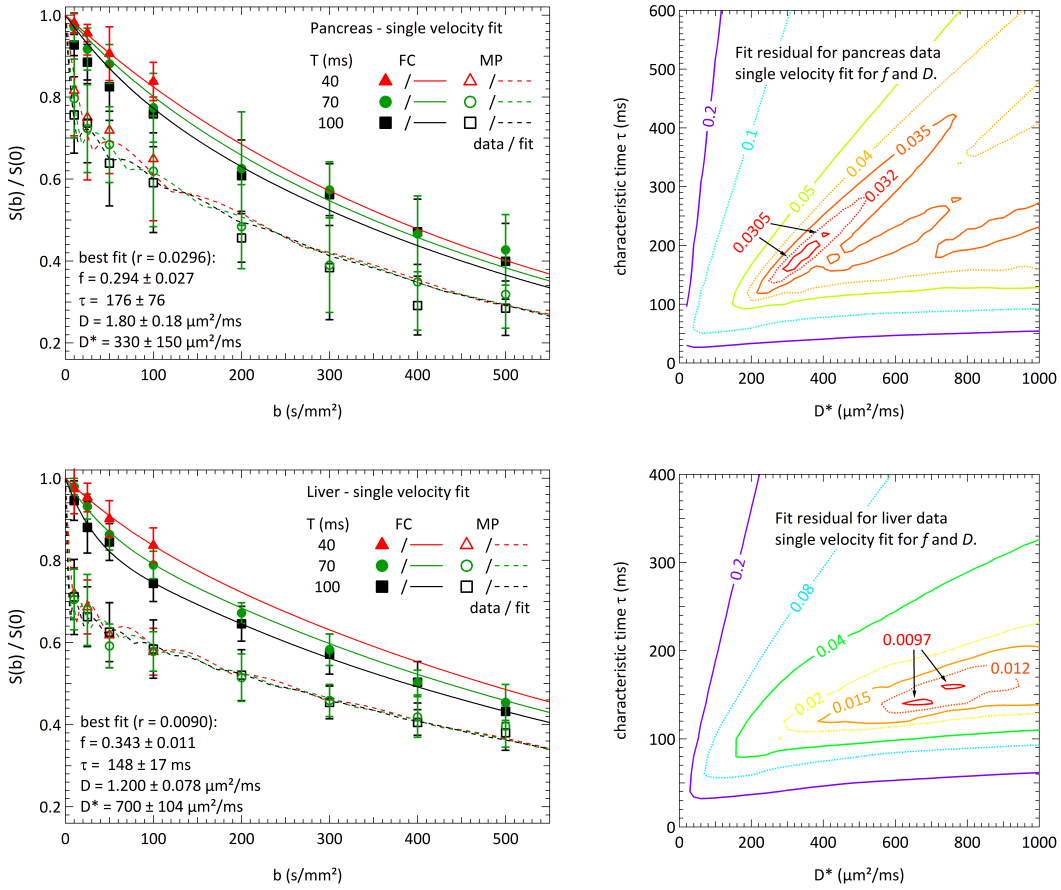

Figure 5.3: Results from fitting the basic IVIM model to pancreas (top) and liver data (bottom). While the model can well describe the observed signal attenuation in the liver, it partly fails for low b-values and flow compensated gradients for the pancreas. The oscillations observed for a single velocity fit in the monopolar model lead to a non-convex residual function with local minima (shown on right side). As a consequence the result of the fitting was found to depend on the chosen initial values.

- The fit works better for the liver data set (bottom) than for the pancreas data (top). This is not only reflected in the uncertainties of the fit parameters, but can also be perceived from the accordance of the fit with flow compensated data acquired at low b-values.
- The monopolar model curves show oscillations, which have never been reported *in vivo*. Due to those oscillations, the fit function becomes non-convex (see contour plots for residuals) and the result is likely to correspond to a local minimum. In addition the fit result becomes dependent on the initial parameters.

While the model can reproduce the experimentally obtained results, the initial version, which was described in chapter 4 seems unsuited to obtain information on the microscopic parameters τ and v (D^*), due to the oscillations of the monopolar model signal. Therefore instead of calculating the signal attenuation assuming only a single velocity, different velocity distribution will be examined in the following sections. The arterial / venous model presented in 5.2.3 and the logarithmic velocity distribution (section 5.2.4) are inspired by the work of Henkelman *et al.* [54]. The parabolic velocity distribution corresponds to the laminar flow profile (section 5.2.5).

5.2.3 Arterial / venous model

The arterial / venous model account for the fact that approximately 80% [54] of the blood circulates in the venous system, where it travels with a velocity v_v, which is approximately given by $v_v \approx 0.35\ v_a$ [55], where v_a is the velocity of blood in corresponding vessels in the arterial system. The average velocity v is then given by $v = 0.2\ v_a + 0.8\ v_v$, yielding $v_a = \frac{25}{12}\ v$ and $v_v = \frac{35}{48}\ v$. Assuming that the vessel dimensions do not differ in arterial and venous branch, the characteristic time τ and thus N have to be scaled by the respective factor. The described model can simply be included into the normalized phase distributions. For calculation of the new phase distributions $\rho'_h(\vartheta, N)$ the influence of the velocity on the accumulated phase has to be taken into account, leading to a broader distribution for arterial blood and a more narrow distribution for venous blood:

$$\rho'_h(\vartheta, N) = 0.2 \cdot \frac{12}{25}\rho_h\left(\frac{12}{25}\vartheta, \frac{25}{12}N\right) + 0.8 \cdot \frac{48}{35}\rho_h\left(\frac{48}{35}\vartheta, \frac{35}{48}N\right). \tag{5.2}$$

The results from fitting the phase distributions are shown in Fig. 5.4. The oscillations are still present in the model signal attenuation curves, which are found to be very similar to those shown in Fig. 5.3. If the velocities v_{single} and the average velocity in the arterial / venous model v are calculated from fit parameters, the ratio is found to be $v_{\text{single}}/v \approx 0.743$, which is close to the factor between the velocity in the venous vessels and the average velocity $v_v/v = \frac{35}{48} = 0.729$. This finding implies that the impact of the properties of arterial fraction on the diffusion weighted signal is very small and the arterial / venous model is basically identical to the basic model, which assumes only a single velocity.

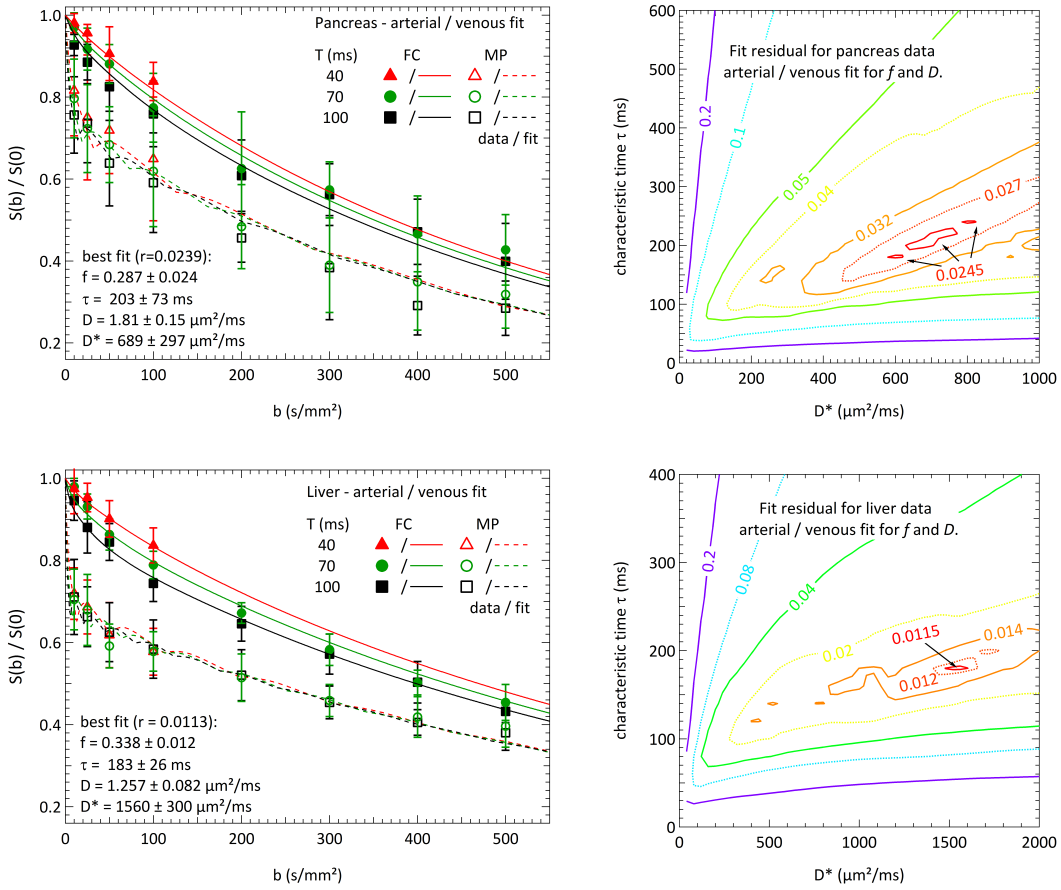

Figure 5.4: Results from fitting the arterial / venous IVIM model. The oscillations are still present in the monopolar model. The attenuation curves are very similar to those of the basic model, shown in Fig. 5.3. The fit parameters D^* and τ are larger than those obtained with the basic model, indicating that the arterial fraction only has a very small impact on the signal attenuation curves in the arterial / venous IVIM model.

5.2.4 Logarithmic velocity distribution

The logarithmic velocity distribution introduced in this section originates is the result if a self similar vascular structure is assumed. According to Henkelman [54] self similarity implies not only that the average length of a vessel segment is proportional to its diameter, but also that a cubic relationship for the parent and daughter vessel diameters at bifurcations (eq. (5.3)) can be derived.

$$d^3 = d_1^3 + d_2^3 \tag{5.3}$$

From this relation follows that the volumetric distribution of blood in vessels of diameter d between minimum $d_{\min}$ and maximum diameter $d_{\max}$ is uniform on a logarithmic scale, further implying that the number of vessels N with a certain diameter d is proportional to d^{-3} as was it was confirmed for the canine vascular system [56]. Conservation of blood flow leads to the relation given in eq. (5.4) from which the proportionality of flow velocity to vessel diameter $v \propto d$ can be deduced.

$$\frac{\pi}{4} d^2 N v = const \tag{5.4}$$

The distribution ρ_v of velocities v between $v_{\min}$ and $v_{\max}$ is because of the proportionality to d given by eq. (5.5), where the ratio of minimum and maximum diameter $r_d = \frac{d_{\max}}{d_{\min}} = \frac{v_{\max}}{v_{\min}}$ was introduced.

$$\rho_v(v, r_d) = \rho_v(\ln(v), r_d) \cdot \frac{\mathrm{d}(\ln(v))}{\mathrm{d}v} = \frac{1}{v \ln(r_d)} \tag{5.5}$$

The mean velocity is thus given by $\bar{v} = \frac{v_{\max} - v_{\min}}{\ln(r_d)}$, so that minimum and maximum velocity are related to the mean velocity by eq. (5.6a) and (5.6b).

$$v_{\min} = \bar{v} \cdot \frac{\ln(r_d)}{r_d - 1} \tag{5.6a}$$

$$v_{\max} = \bar{v} \cdot \frac{r_d \ln(r_d)}{r_d - 1} \tag{5.6b}$$

As stated above, the length of vessel segments is proportional to the diameter, such that the characteristic time τ and thus the ration $N = \frac{T}{\tau}$ is the same for all vessel diameters, which allows us to formulate the equation for calculating the normalized phase distributions in the logarithmic model (eq. (5.7)) from the phase distributions of the basic model, which were created as described in chapter 4.

$$\rho_h'(\vartheta, N) = \int_{v_{\min}}^{v_{\max}} \frac{1}{v \ln(r_d)} \cdot \frac{\bar{v}}{v} \rho_h \left(\frac{\bar{v}}{v} \vartheta, N \right) \mathrm{d}v = \frac{r_d - 1}{\ln(r_d)^2} \int_1^{r_d} \frac{1}{r'^2} \rho_h \left(\frac{r_d - 1}{r' \ln(r_d)} \cdot \vartheta, N \right) \mathrm{d}r' \tag{5.7}$$

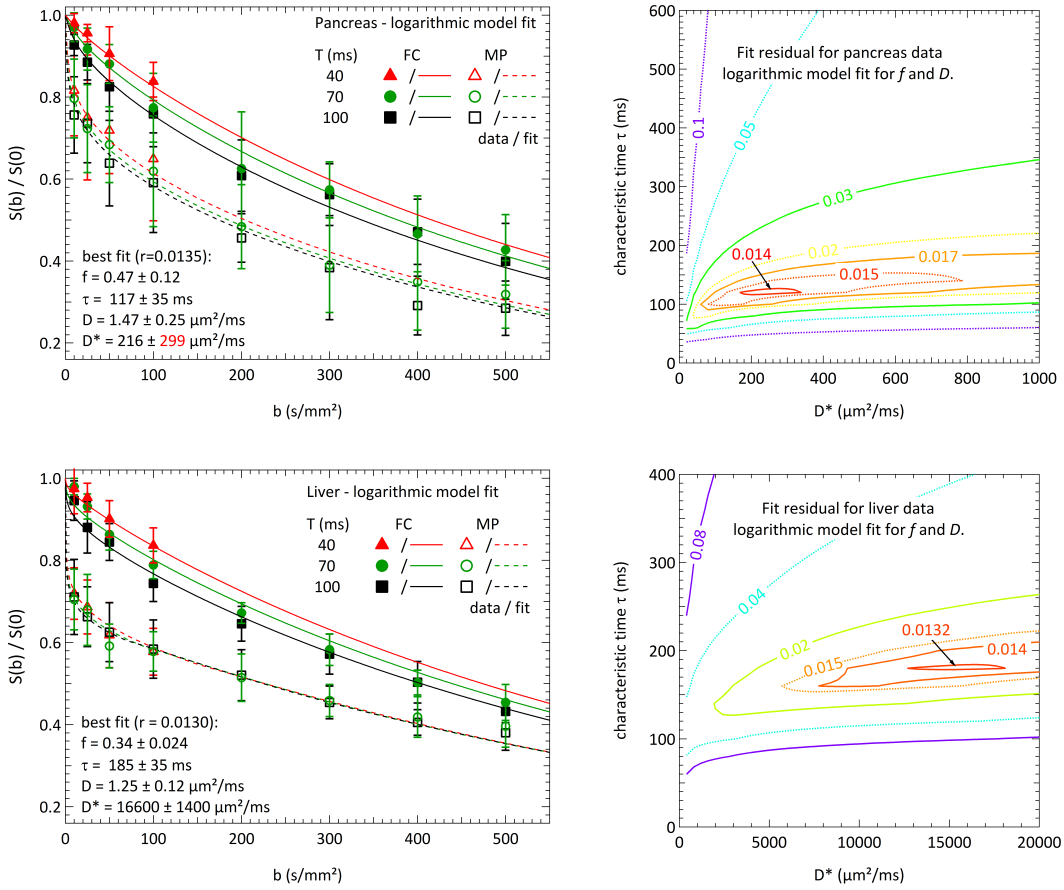

Figure 5.5: Results from fitting the logarithmic IVIM model with $r_d = 100$. The oscillations in the bipolar model attenuation curves are not visible anymore. T-dependence in the low b-value region for flow compensated pancreas (top left) is well resolved. The contour maps of the residual function do not show local minima anymore. The error in the fitted value of D^* and its absolute value for the liver are very large.

While the normalized phase distributions in the logarithmic model do not depend on the exact value of minimum and maximum vessel diameter, they however are different for each ratio r_d. The influence on r_d will be discussed in section 5.2.6, where the different velocity distributions are compared. The result for fitting the logarithmic model with $r_d = 100$ are shown in Fig. 5.5. The assumption of a logarithmic velocity distribution eliminates the oscillations in the monopolar attenuation curves. As a result of this, the existence of local minima is greatly reduced and the fitting process was found to converge independently on the initial values. The T-dependence in the flow compensated pancreas data is well reproduced by the logarithmic IVIM model. The necessity to specify the ratior_d of smallest and largest vessel diameter introduces however a new parameter, the choice of which also influences the meaning of the fitted D^* values. For the chosen $r_d = 100$ the relative fit error of D^* for the pancreas data is very large, while for the liver data the absolute value is almost two orders of magnitude higher than for the pancreas. This discrepancy is most likely due to the fact that the monopolar data dies show a small dependence on T for the pancreas, but not for the liver. Since the model apparently predicts a small T-dependence, as can be inferred from the fitted curves for the pancreas, the effect gets less pronounced for larger flow velocities. To reduce the least squares error, the value of D^* is adjusted during the fitting process to a value corresponding to an average blood flow velocity of $v \approx 23.2$ mm/s. This value is out of the range of physiological findings [57]. Another anomaly is the high value of the perfusion fraction f in the pancreas, which can be explained by the fact that the large ratio r_d corresponds to a large fraction of the blood which travels with very small velocities and thus does not exhibit a very pronounced bi-exponential signal decay.

5.2.5 Parabolic velocity distribution

Another possible velocity distribution is the laminar flow profile, in which the blood flow velocity in a vessel of circular cross section with diameter d is given as a function of the radial coordinate r by eq. (5.8a), where $\bar{v}$ denotes the average velocity. The distribution of radial positions is given by eq. (5.8b).

$$v(r) = 2\bar{v}\left(1 - \frac{2r}{d}\right) \tag{5.8a}$$

$$\rho_r(r, d) = \frac{8r}{d^2} \tag{5.8b}$$

While in the self similar model presented in the last section τ was the same for each velocity, in the laminar flow model τ becomes larger for particles with smaller velocities, such that for the ration $N = \frac{T}{\tau}$ we get $N(v) = N(\bar{v}) \cdot \frac{v}{\bar{v}}$. Putting it all together we can calculate the normalized phase distributions for a laminar flow profile as given by eq.

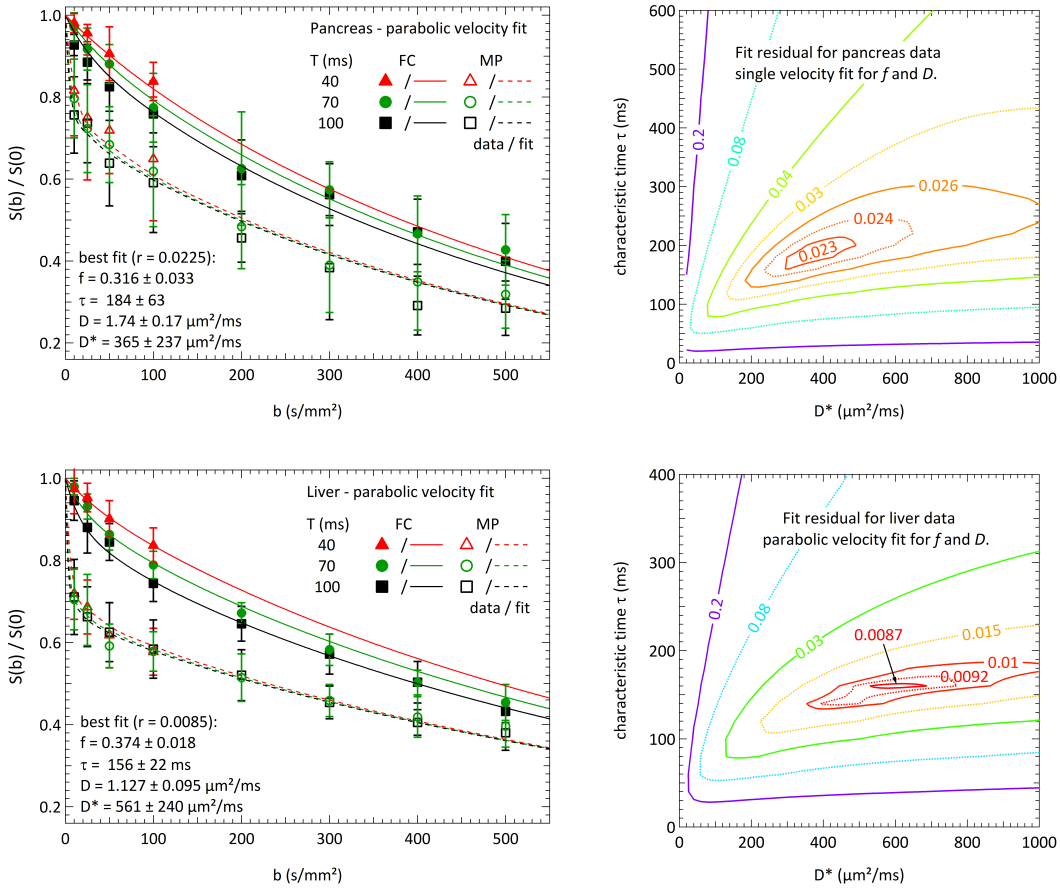

Figure 5.6: Results from fitting the parabolic IVIM model to pancreas (top) and liver data (bottom). Monopolar oscillations are suppressed. The model can well resolve all features of the experimentally obtained liver data set. The pancreas signal attenuation is reproduced for small b-values better than in the basic IVIM model, but not as good as in the logarithmic model. For high b-values the pancreas data shows more inter-subject variance and is less good approximated than the liver data.

(5.9), where in the last step the substitution $r' = 1 - \frac{2r}{d}$ was used.

$$\rho'_h(\vartheta, N) = \int_0^{d/2} \frac{8r}{d^2} \cdot \frac{\bar{v}}{v(r)} \rho_h \left(\frac{\bar{v}}{v(r)}\vartheta, \frac{v(r)}{\bar{v}} N \right) \mathrm{d}r = \int_0^1 \frac{1-r'}{r'} \rho_h \left(\frac{\vartheta}{2r'}, 2r'N \right) \mathrm{d}r' \quad (5.9)$$

The normalized phase distributions for the parabolic IVIM model are thus independent of the vessel diameter. The results from fitting the parabolic model to the experimentally obtained data is shown in Fig. (5.6). The oscillations in the monopolar signal attenuation curves are not present anymore int the parabolic IVIM model. As a result, local minima are largely suppressed as well. While the liver data is very well described by the parabolic model, the pancreas data, especially the data at high b-values, does not always match the experimental data. However the larger inter-subject variance in the pancreas high b-value data might explain this.

5.2.6 Comparison of the velocity distributions

After the different models have been introduced, the obtained fit parameters are compared in this section. Tab. 5.1 shows the parameter estimates resulting from fitting the IVIM models with different velocity distributions to the experimentally obtained data. The basic IVIM model and the arterial/venous model yield very similar parameter esti-

Pancreas	basic	arterial/venous	logarithmic	parabolic
D (μm^2/ms)	1.80 ± 0.18	1.81 ± 0.15	1.47 ± 0.25	1.74 ± 0.17
f	0.294 ± 0.027	0.287 ± 0.024	0.47 ± 0.12	0.316 ± 0.33
τ (ms)	176 ± 76	203 ± 73	117 ± 35	184 ± 63
D^* (μm^2/ms)	330 ± 150	689 ± 297	216 ± 299	365 ± 237
residual	0.0296	0.0239	0.0135	0.0225

Liver	basic	arterial/venous	logarithmic	parabolic
D (μm^2/ms)	1.200 ± 0.078	1.257 ± 0.082	1.25 ± 0.12	1.127 ± 0.095
f	0.343 ± 0.011	0.338 ± 0.012	0.34 ± 0.024	0.374 ± 0.018
τ (ms)	148 ± 17	183 ± 26	185 ± 35	156 ± 22
D^* (μm^2/ms)	700 ± 104	1560 ± 300	16600 ± 1400	561 ± 240
residual	0.0296	0.0113	0.0130	0.0085

Table 5.1: Parameter estimates obtained by fitting variations of the IVIM model to the experimentally obtained pancreas (top) and liver data (bottom).

mates for f and D. They both suffer from local minima of the residual function and thus are susceptible to variations in the initial fit values. The microscopic parameters τ and D^* are increased in the arterial/venous model, which is due to the stronger weighting

of the venous fraction. The ratio of flow velocities obtained from the fit parameters is $\frac{v_{\text{basic}}}{v_{\text{a/v}}} = 0.743$ for the pancreas data and 0.745 for the liver data, which is very close to the ratio $\frac{35}{48} \approx 0.729$ between the assumed venous and the average velocity in the arterial/venous model. The oscillations in the monopolar signal attenuation curves are not present in the logarithmic and parabolic model which causes the fit result to be independent of the initial values. The logarithmic model predicts a stronger T-dependence of the monopolar data at low b-values, which is found in the pancreas data. Due to the fact that this dependence is not visible in the liver data, a very large D^* is fitted, resulting in an unphysiologicly high flow velocity of 23.2 mm/s. While the pancreas data can be well described by the logarithmic model, the perfusion fraction found for the pancreas data is very large and the diffusion coefficient D also differs from the one found using the other models. This is due to the fact that a large fraction of the blood fraction in the logarithmic model travels with very slow velocities thus not contributing to the biexponential decay. The perfusion fraction f furthermore becomes dependent on the ratio between largest and smallest vessel diameters, which is another independent parameter. For those reasons the parabolic IVIM model was chosen to work with. Its macroscopic parameters f and D are in accordance with the basic and arterial/venous model, but it has the advantage that its estimates for τ and D^* are not dependent on the initial guess. It also best reproduces the liver signal attenuation curves. The uncertainties of the fit parameters are in general higher than in the basic model because no trapping in local minimas is present, since monopolar oscillations are suppressed.

5.3 Parameter maps

Using the parabolic model the parameter maps shown in Fig. 5.7 where obtained by pixel-wise fitting of the parabolic IVIM model. In addition to the estimates obtained for the fit parameters D, f, τ and D^*, the averaged unweighted (b_0) image, the velocity obtained via $v = \sqrt{\frac{6D^*}{\tau}}$ and the fit residual are displayed for the 6 different test subjects.

The organ structure shown in the b_0 images can easily be identified in the D and f maps again. The maps for τ and D^* however appear for some of the test subjects (1, 2 and 5 counted from top) very noisy. Since this is to be expected for D^* due to the large dynamic range that can be anticipated from its definition the information might be better represented using v-maps. In certain regions of the image it cannot be expected to obtain meaningful information on the microscopic parameters. Examples for those regions are very low SNR (around the spine), motion (stomach), large arteries and low f - regions such as the spleen. A possibility to quantify the quality of the pixel-wise fitting (fitting before averaging) is to compare the ROI-averaged parameter estimates to those obtained from ROI-wise fitting (averaging before fitting), which is done in Tab. 5.2. The stated values are averaged over test subjects and the stated error corresponds to the standard deviation of the mean. While the values for the

Liver	ROI-wise	pixel-wise
D (μm^2/ms)	1.211 ± 0.026	1.179 ± 0.037
f	0.352 ± 0.026	0.349 ± 0.025
τ (ms)	162 ± 15	339 ± 66
D^* (μm^2/ms)	619 ± 91	3640 ± 990

Table 5.2: Comparison of parameter estimates obtained from fitting the parabolic IVIM model to liver data. For the ROI-wise column fitting was performed after averaging of the signal in a ROI, while for the pixel-wise column the IVIM model was fitted for each pixel and the resulting parameter estimates averaged over the ROI. Values given are averaged over test subjects, the error corresponds to the standard deviation of the mean.

macroscopic parameters f and D are in accordance for ROI-wise and pixel-wise fitting, the microscopic parameters τ and D^* are much larger for pixel-wise fitting. A possible explanation for this is that the diffusion weighted signal is overlaid by pseudo-random contributions due to noise and pulsation which make it delicate task to resolve the T-dependence of the flow compensated attenuation curves. If no such T-dependence is apparent in the data, the consequence would be that the timescale τ of the incoherent motion is much different from T. It can however not be much smaller, because then no difference in signal attenuation between monopolar and flow compensated gradients

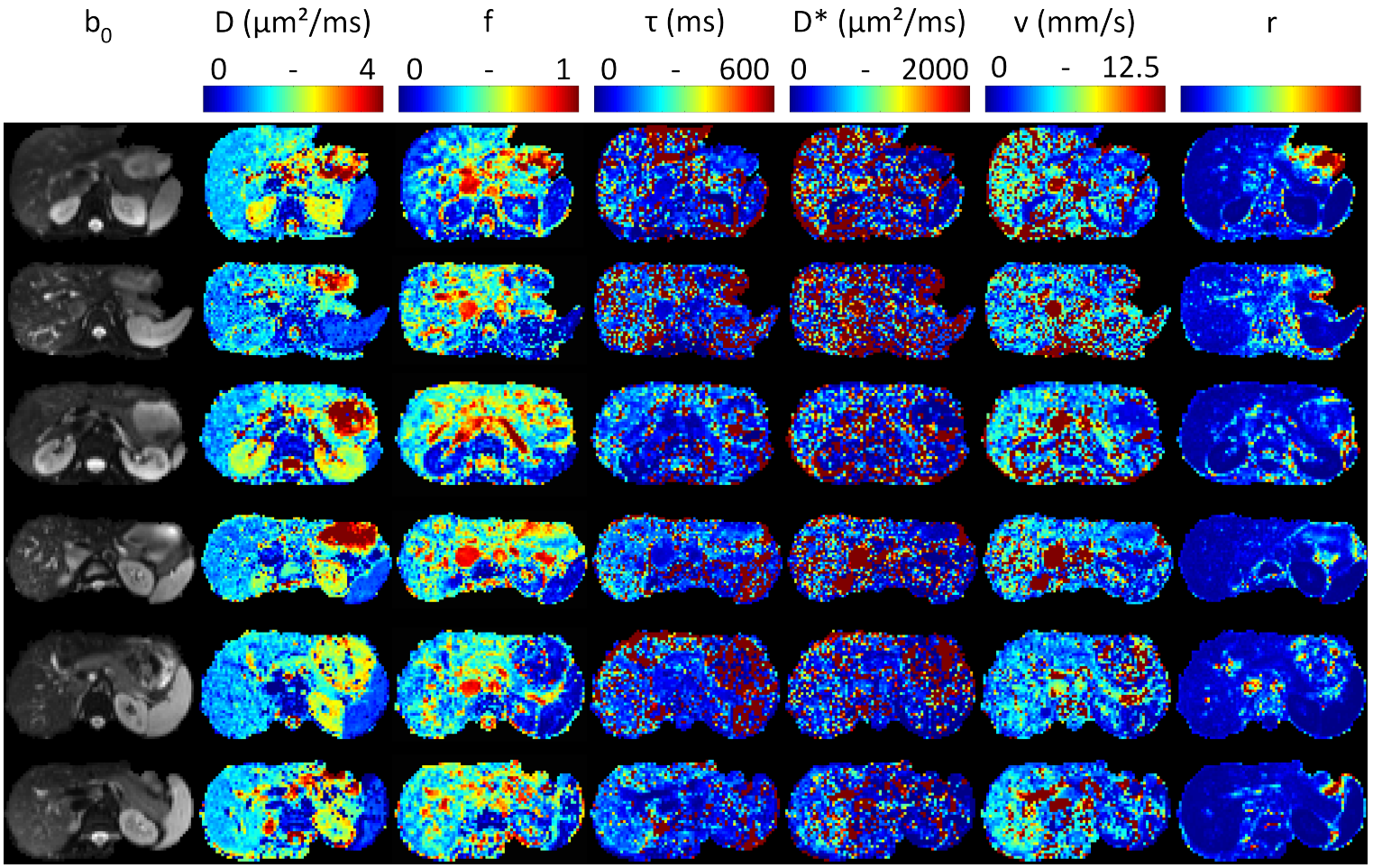

Figure 5.7: Parameter maps obtained from a pixel-wise fit of the parabolic IVIM model. Abdominal organs can be easily identified in the maps for unweighted (b_0) signal, D and f. The maps for τ and D^* appear very noisy and for a large percentage of pixels the fitting fails, yielding very high τ-values. Since the large dynamic range for D^* values can be expected, the data can be more conveniently presented using maps of the velocity v.

would be found. Therefore the characteristic time τ is overestimated in the pixel-wise fitting. Similar arguments can be made for the velocity v. Since larger velocities reduce the amount of remaining signal and thus the absolute T-dependence, the values of D^* are also overestimated by pixel-wise fitting. To overcome these issues in order to obtain parameter maps which are less affected by noise and pseudo-random signal contributions, it would be desirable to increase the number of averages. The total duration of the measurement protocol used in this chapter, however, was already too long (20 breath holds of 37 seconds duration) to be easily incorporated into a clinical study. The results from implementing a denoising algorithm based on principal component analysis to overcome those difficulties are presented in the following chapter.

6 Results: Denoising using principal component analysis

In this chapter a denoising algorithm based on principal component analysis (PCA) is applied to the data acquired as described in section (5.1), to address two competing issues. On the one hand it would be desirable to increase the number of signal averages to reduce the influence of pseudo-random contributions from pulsation and noise, while on the other hand the number of 300 images acquired per slice to perform a fit with 4 free parameters appears already very large. For liver and pancreas, where diffusion properties are isotropic, the acquisition of 6 different diffusion directions only contributes to increasing the SNR such that only 40 different diffusion weightings remain, if the unweighted images (of which 3 were acquired during each breath hold) are subtracted. The idea behind the algorithm described in this chapter is that if the signal for different diffusion weightings could be described by a model that has less free parameters (such as e.g. the IVIM model introduced in chapter 4), it is compressible and there is a way to transform it into a domain in which it is sparse (only having very few non-zero coefficients). In this chapter, principal component analysis is used to estimate a sparse transform for each pixel based on the pixel values in its local environment and those measured for different diffusion gradient directions (section 6.1). The obtained transformation is then used to reduce the amount of pseudo-random signal contributions by performing a minimization of the L_1-norm in the supposedly sparse domain, while maintaining data consistency in k-space (section 6.2). The parabolic IVIM model is then fitted to the fully sampled data set and to one with reduced SNR (only 2 diffusion directions) and results are compared to those obtained after application of PCA-denoising and to those where a simple median filter was used (section 6.3).

6.1 Principal component analysis

Principal component analysis was first described by Karl Pearson [58] and is often named Karhunen-Loève transform (KLT) when applied in the field of image processing. From a mathematical point of view, it is an orthogonal linear transformation which transforms the data such that the projection of greatest variance corresponds to the first (principal) component of the data's representation in the new domain. If the data set consists of n variables, the first principal component is defined as the direction in n-dimensional space that minimizes the distance to the mean-corrected data points. The second principal

component can be defined the same way after the correlations with the first principal component are subtracted from the mean-corrected data. The principal components can be obtained from the eigenvectors of the covariance matrix of the data.

In the following the application of PCA tailored to the acquired diffusion data set is formulated. The data set consists of 300 images per slice of which 60 are unweighted. The other 240 images correspond to diffusion weighted signals for 40 different combinations of diffusion time T, b-value and gradient profile, which were acquired for 6 different diffusion directions. Since isotropy is assumed, the signal of interest consist of 40 *variables*, for which the acquired diffusion directions represent different *observations*. To be able to apply the denoising algorithm to the whole data set, the unweighted images are also included, yielding a total of $n = 50$ variables, which are combined into the signal vector $\boldsymbol{\sigma}$, defined via eq. (6.1a). The observation matrix $\underline{\underline{\boldsymbol{\sigma}}}$ consists of the signal vectors σ_k measured for a given diffusion direction, respectively observation k as specified by eq. (6.1b).

$$\boldsymbol{\sigma} = \begin{pmatrix} d_1 \\ \vdots \\ d_n \end{pmatrix} \tag{6.1a}$$

$$\underline{\underline{\boldsymbol{\sigma}}} = \begin{pmatrix} \boldsymbol{\sigma_1} & \cdots & \boldsymbol{\sigma_m} \end{pmatrix} = \begin{pmatrix} (d_1)_1 & \cdots & (d_1)_m \\ \vdots & & \vdots \\ (d_n)_1 & \cdots & (d_n)_m \end{pmatrix} \tag{6.1b}$$

Each row of the matrix $\underline{\underline{\boldsymbol{\sigma}}}$ thus corresponds to a different signal variable, respectively diffusion contrast, while each column addresses an observation, respectively diffusion gradient direction. The entries of the covariance matrix of the observation matrix are defined by eq. (6.2), where the brackets $\langle \cdots \rangle$ denote the expectation value, respectively the average over observations.

$$\Big(\mathrm{cov}(\underline{\underline{\boldsymbol{\sigma}}})\Big)_{ij} = \langle (d_i - \langle d_i \rangle)(d_j - \langle d_j \rangle) \rangle = \langle d_i d_j \rangle - \langle d_i \rangle \langle d_j \rangle \tag{6.2}$$

The principal components are given by the eigenvectors $\boldsymbol{\Psi_l}$ of the covariance matrix of the observations. The covariance matrix of $\underline{\underline{\boldsymbol{\sigma}}}$ can thus be expressed by eq. (6.3), where λ_l denotes the corresponding eigenvalues.

$$\mathrm{cov}(\underline{\underline{\boldsymbol{\sigma}}}) = \sum_{l=1}^{n} \lambda_l \boldsymbol{\Psi_l} \boldsymbol{\Psi_l^T} \tag{6.3}$$

We define the matrix of the eigenvalues of the covariance matrix as denoted in eq. (6.4).

$$\underline{\underline{\boldsymbol{\Psi}}} = \begin{pmatrix} \boldsymbol{\Psi_1} \cdots \boldsymbol{\Psi_n} \end{pmatrix} \tag{6.4}$$

The relation between an observed signal vector $\boldsymbol{\sigma}$ and its representation $\boldsymbol{x}$ in the sparse domain is thus given by eq. (6.5).

$$\boldsymbol{\sigma} - \langle \boldsymbol{\sigma} \rangle = \underline{\underline{\boldsymbol{\Psi}}}\, \boldsymbol{x} \tag{6.5}$$

A Karhunen-Loève transform is thus defined by the eigenvalue matrix $\underline{\underline{\boldsymbol{\Psi}}}$ and the mean signal vector $\langle \boldsymbol{\sigma} \rangle$, which can both be estimated based on a given set of m observations. $\mathrm{cov}(\underline{\boldsymbol{\sigma}})$ however has at most rank $n-1$, due to the intrinsic subtraction of the variable mean in the calculation process of the covariance matrix. If $m < n-1$ the rank of the covariance matrix further reduces to $m-1$. While the information, respectively the signal variance is concentrated in the principal components (corresponding to the largest eigenvalues) of $\boldsymbol{x}$ it is thus however necessary to have a sufficiently large number m of observations to be able to identify the principal components. Since the number of different diffusion directions which were acquired is only 6 (respectively 2 for the data set with reduced acquisition time / SNR), the 8 surrounding pixels are additionally used as observations, yielding a total of 54 observations for the full data set and 18 observations for the reduced one.

In the ideal case, all information on the actual signal is contained in the eigenvectors, respectively the matrix $\underline{\underline{\boldsymbol{\Psi}}}$, while the pseudo-random contributions get absorbed into $\boldsymbol{x}$. Therefore an L_1-norm minimization of the signal $\boldsymbol{x}$ in the transformed domain should reduce the amount of noise and pseudo-random signal contributions caused by pulsation.

6.2 Denoising procedure

To be able to perform denoising, a data consistency criterion needs to be applied simultaneously while minimizing the L_1-norm of $\boldsymbol{x}$. Since the distribution of noise in the image is non-homogeneous and generally described by an asymmetric Rician distribution [59], it is difficult to formulate such a data consistency criterion in image space. The Rician distribution of noise is based on the assumption that noise in k-space is homogeneously distributed, uncorrelated in time and can be modeled Gaussian-distributed for each point in k-space. Using the noise parameter ε, which is estimated from the mean absolute signal in a small region in a corner of k-space averaged over all images, the denoising problem can thus be formulated as given by eq. (6.6), where W^{-1} denotes the two-dimensional inverse Fourier transform from image space to k-space.

$$\min_{\boldsymbol{x}} |\boldsymbol{x}| \quad \text{s.t.} \quad \| W^{-1} \underline{\underline{\boldsymbol{\Psi}}}\, \boldsymbol{x} - W^{-1} \left(\boldsymbol{\sigma} - \langle \boldsymbol{\sigma} \rangle \right) \|_2 < \varepsilon \tag{6.6}$$

This equation must however be read slightly different from eq. (6.5), which is defined point-wise. To be able to formulate the data consistency criterion in k-space, however, whole images must be used. The signal vector $\boldsymbol{\sigma}$ in eq. (6.6) is basically a three-dimensional data set consisting of two-dimensional images for each diffusion weighting,

where $\langle \boldsymbol{\sigma} \rangle$ denotes the signal for each combination of pixel position and diffusion weighting averaged over observations. Accordingly $\underline{\underline{\boldsymbol{\Psi}}}$ cannot be thought of as a mere matrix, but denotes a pixel-wise multiplication with the pixel-wise defined eigenvalue matrix. The noise parameter in eq. (6.6) corresponds to the noise parameter obtained for a single k-space point multiplied by the square root of the total number of elements in $\boldsymbol{\sigma}$. Fig. 6.1 tries to explain the effects of the different operators. The operators were

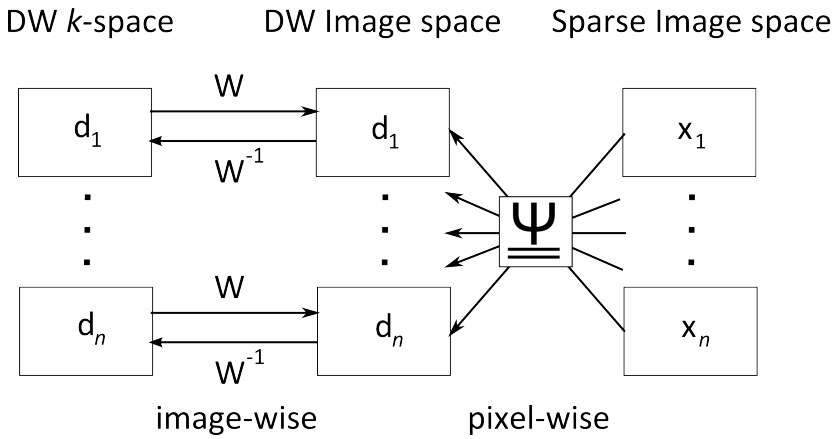

Figure 6.1: Schematic view of the effect of the operators used in eq. (6.6). The data set consists of images belonging to different diffusion contrasts $d_1, \ldots, d_n$. While the two dimensional Fourier transform connects image space and k-space, the pixel-wise KLT connects image space and sparse domain. In particular, the matrix $\underline{\underline{\boldsymbol{\Psi}}}$, which is determined separately for each pixel, defines the transformation back from the sparse domain into image space.

implemented into MATLAB using the TFOCS package [60]. The problem stated in eq. (6.6) is of the form of a basic pursuit denoising problem, which can be solved by a variety of different methods. In this work the SPGL1 solver, which is based on the algorithm described in [61, 62] was used to find the solution to eq. (6.6).

6.3 Comparison of original and denoised data sets

In this section the results obtained by fitting the parabolic IVIM model (as described in chapter 4 and section 5.2.5) to various data sets are compared. The labels and differences of the six data sets are explained in the following. The aim of this study was, to investigate whether it is possible to reduce the amount of diffusion directions, respectively averages and to characterize the impact of denoising prior to fitting on the resulting parameter maps. The following labels are used to distinguish between the data sets:

full The full data set corresponds to the acquisition protocol described in section 5.1. It consists of 300 images per slice, which are splitted into 60 unweighted images and 40 different diffusion contrasts, which were obtained for 6 different diffusion gradient directions.

denoised The denoised data set is obtained by applying the denoising procedure as described in section 6.2 to the full data set. The necessary KLT is estimated as described in section 6.1, where the 6 diffusion directions and 8 surrounding pixel give a total of 54 observations.

median The median data set is obtained by simply applying a 3×3 median filter in image space to the full data set.

undersampled (us) The undersampled data is obtained from the full data set by randomly choosing only one of the three unweighted images for each breath hold and only two out of six diffusion directions for each diffusion contrast.

denoised+us The denoised and undersampled data set is obtained by applying the KLT-denoising procedure to the undersampled dataset. The necessary KLT however is only based on the two diffusion directions remaining in the undersampled data set and not on the full six directions of the full data set. Taking the surrounding pixels into account, this gives a total of 18 observations per diffusion contrast.

median+us This data set is obtained by applying a 3×3 median filter in image space to the undersampled data set.

After a qualitative evaluation of the parameter maps obtained for the six different data sets for two of the test subjects (section 6.3.1), an evaluation of a ROI placed in the liver is performed to quantitatively assess the effect of denoising on the parameter estimates obtained from fitting the IVIM model.

6.3.1 Qualitative evaluation based on parameter maps

The parameter maps obtained by fitting the parabolic IVIM model to the different data sets are shown in Fig. 6.2 and 6.3. The results shown in Fig. 6.2 are very promising. The grizzly structure of the parameter maps, which is especially perceivable for the microscopic parameters τ, D^* and the corresponding v is largely reduced by applying either KLT-denoising or the median filter. This effect is visible for both the fully sampled data sets (top rows) and the undersampled (lesser SNR) data sets (bottom rows). The noise reduction however comes at a the price of resolution. While smoothing is hardly visible in the KLT-denoised average b_0 images, it is very prominent in the median filtered

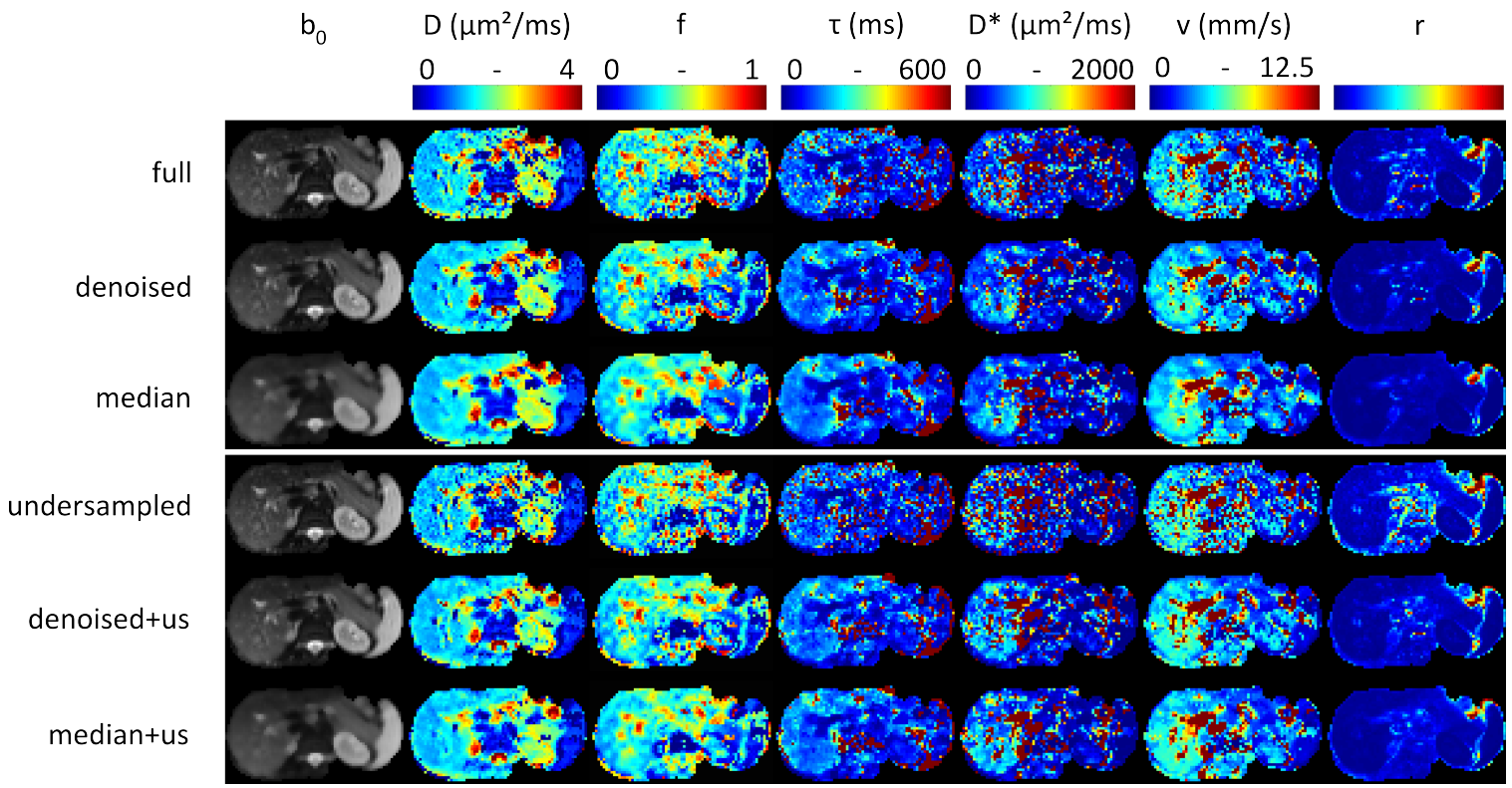

Figure 6.2: Exemplary parameter maps for one of the test subjects from a pixel-wise fit of the parabolic IVIM model to differently prepared data sets. While the amount of pseudo-random contributions, which is especially visible in the τ-, D^*- and v-maps in the unprocessed data (full and undersampled), is largely reduced by all post-processing methods, the denoising parameter maps appear to be less washed out than the median maps, which can be best perceived for b_0, D and f. Also the amount of pixels for which the fitted IVIM model cannot describe the experimental data well is reduced by post-processing, which can be inferred from the residual maps.

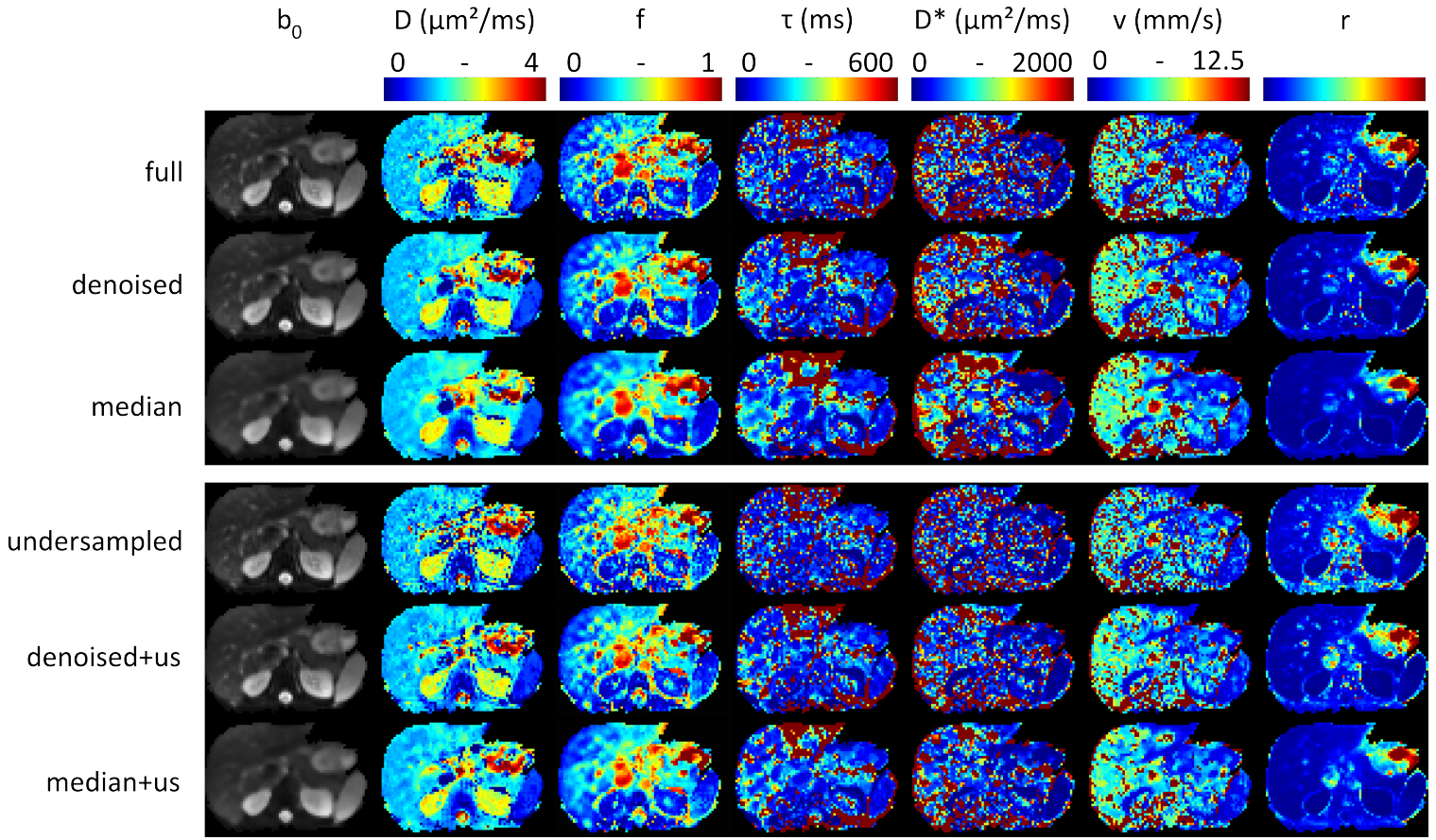

Figure 6.3: Similar conclusions to those made for Fig. 6.2 can be made for a second test subject. The red borders in the D^*-maps however indicate, that the test subject might have moved slightly during the duration of the MRI experiment. This might be the reason why the denoised (pixel-wise KLT) τ and D^*-maps in this case appear less affected, than the smoothed median maps.

maps, which makes the pixel-wise KLT the preferable denoising algorithm for the data shown in Fig. 6.2. The elimination of pseudo-random signal contributions also reduces the number of pixels, where the fit cannot describe the data well, which results in less regions with a high fit residual (last column). While for the data set shown in Fig. 6.2 the reduction in SNR resulting from reducing the number of diffusion directions by a factor of 3 is hardly visible, circumstances are less favorable for the data set shown in Fig. 6.3. In addition to the perceivable noise in the parameter maps, the subject might have moved slightly during the time of the diffusion experiment, which can be inferred from the high D^* and v values at the edges of the abdominal section. Based on the τ-maps, the parameter maps obtained from the fully sampled median filtered data set appear to resolve the liver structure in the bottom left corner of the abdominal section best. It is possible that the pixel-wise KLT denoising cannot overcome the small movements and the resulting parameter maps are in the case depicted in 6.3 inferior to those obtained by median-filtering.

6.3.2 Quantitative evaluation based on ROI data

To quantify the effects of denoising on the parameters in the IVIM model, evaluation of a ROI placed in the liver is performed similar to section 5.3. Fig. 6.4 shows the parameter estimates averaged over test subjects, where error bars correspond to the standard deviation of the mean value for different subjects. For each data set values obtained by pixel-wise fitting of the model (and subsequent averaging over ROI) and by ROI-wise fitting (averaging over ROI before fitting) are compared. The macroscopic parameters f and D are found to be largely independent of the applied preprocessing algorithm and also do not differ very much for pixel-wise and ROI-wise fitting, when compared to the microscopic parameters τ and D^*. While these results indicate that the parameter estimates for τ and D^* obtained ROI-wise are relatively unaffected by the tested preprocessing algorithms, they are smaller than the pixel-wise obtained parameter estimates. The absolute value and thus the difference between to the ROI-wise parameter estimates is reduced for τ and D^*, if a preprocessing algorithm is applied. This supports the theory, that pseudo-random contributions due to pulsation and noise, which are filtered by the preprocessing algorithms, overlay the T-dependence of the flow compensated signal at low b-values, resulting in large values of the fitted τ and D^*. While denoising can improve the quality of the obtained fit parameters by reducing pseudo-random contributions to the diffusion weighted signal, the pixel-wise estimates of the microscopic parameters are still by a factor 2 larger than the ROI-wise obtained ones. This could in theory be a remnant of tissue inhomogeneity in the ROI, but is more likely to be caused by the fact that not all contributions from noise and pulsation can be removed by the tested preprocessing algorithms. Movements of the test subject could also have an impact on the signal, which cannot be corrected for. This however is an inherent problem of long total acquisition time and the use of breath holds.

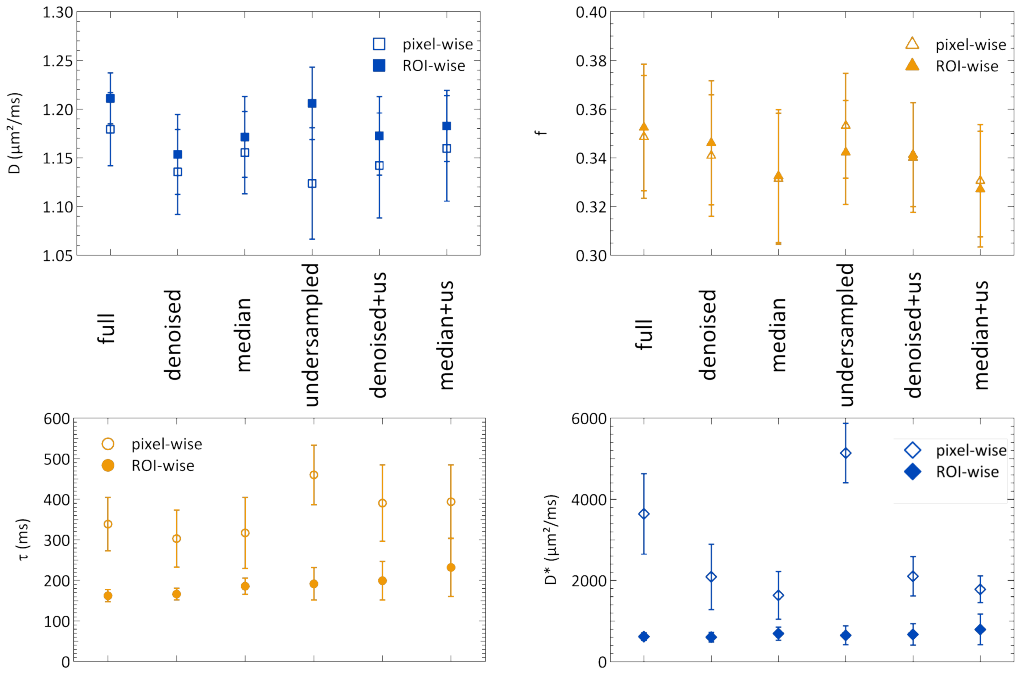

Figure 6.4: Comparison of pixel-wise and ROI-wise obtained parameter estimates for a ROI placed in the liver. Parameter estimates are averaged over test subjects, where error bars correspond to the standard deviation of the mean. While the pixel- and ROI-wise macroscopic parameters D and f (top row) are very similar and appear relatively unaffected by the applied preprocessing, the parameter estimates for τ and D^* (bottom row) show a different behavior. Not only differ pixel- and ROI-wise values (as in section 5.3), but also is this difference reduced, if a denoising algorithm is applied. However only the pixel-wise parameter estimates for τ and D^* are affected by preprocessing, whereas changes in the ROI-wise obtained parameter estimates are hardly noticeable.

7 Discussion

The aim of the work at hand was to investigate the biexponential signal attenuation, which is found in strongly perfused organs, by means of diffusion weighted magnetic resonance imaging (MRI). The biexponential signal decay originates from the additional presence of incoherent blood motion in the tissue. To achieve this goal, a pulse sequence was developed, that enables the use of flow compensated and monopolar diffusion gradients, while also allowing for flow compensation of the imaging gradients. While in section 7.1, the developed pulse sequence is compared to existing ones, the experimental results that were obtained using the pulse sequence are discussed in section 7.2. Abdominal diffusion weighted MRI data from both monopolar and flow compensated diffusion gradients of varying total duration was acquired. An experimentally observed dependence of the diffusion weighted signal on the gradient profile was reported [38]. To explain the observed signal attenuation curves, a method was developed, which allowed to calculate the signal attenuation for incoherent blood motion using precalculated phase distributions. Using this model the observed signal attenuation curves could be explained and the characteristic timescale of the incoherent motion determined, as was presented in [43]. Developing a denoising algorithm allowed to reduce the amount of pseudo-random signal contributions, such that maps of the model parameters could be obtained [63].

7.1 Developed pulse sequence

Pulse sequences for diffusion imaging, which are delivered by the manufacturers of MRI scanners, are optimized in terms of eddy currents [32] and off-isocenter correction for concomitant fields [39, 64], but offer only very limited possibility for the user to adjust the diffusion experiment except for diffusion gradient directions and applied b-value. Typically the whole available echo time is used for the diffusion gradients, which does reduce the necessary gradient amplitude and thus possible artifacts, but also prevents the user from changing echo time and diffusion time independently. This is however critical, if a dependence on the diffusion time is investigated, since it is well known that the different relaxation times of blood and tissue cause IVIM model parameters to correlate with the echo time [46].

The sequence developed in this work was thus designed modular such that the diffusion experiment can be configured almost completely independent of the imaging part of the sequence. Not only is it possible to choose diffusion time and b-value within the hardware limits of the gradient coils, but it is also possible to select different diffusion

gradient profiles. While the use of different gradient profiles to characterize restricted diffusion is well studied [33, 51], its possibility to investigate the effects of incoherent blood motion in abdominal organs was first investigated in this work [38]. Since our initial experiments (section 3.2) showed an increase in the diffusion weighted signal due to destructive interference of velocity encoding of diffusion and imaging gradients, flow compensation for each axis can be switched on or off. The developed diffusion EPI sequence has the additional advantage, that each imaging gradient object is directly accessible and can be modified, while in manufacturer sequences those are often hidden in building blocks with no available source code. The diffusion sequence serves as a template based on which diffusion sequences for other applications, such as fat diffusion imaging [65] or the measurement of exchange rates in yeast diffusion phantoms [66].

Ahn *et al.* [67] first reported the successful acquisition of both flow compensated and non-flow compensated *in vivo* images. The sequence design used in their work allowed to obtain a measure of the capillary density, which could possibly be related to f. They did however not provide quantitative information on the *in vivo* data, which was critically acclaimed [68], and did not vary the diffusion time.

The use of flow compensated diffusion gradients to separate diffusion and microcirculatory flow was suggested by Maki *et. al.* [48, 69], who presented the first study comparing flow compensated and non-flow compensated diffusion gradients. His sequence design also allowed to change the diffusion gradient timing independently of the echo time. The aim of the study [69] was however different from the work at hand. Maki *et. al.* were imaging the rat brain, where the perfusion fraction is very small. Their aim was to maximize the contrast to noise ratio, more specifically increase the sensitivity to microcirculatory flow, while decreasing the sensitivity to diffusion. The gradient profile, which does fulfill this characterization is the monopolar profile of maximum duration. If the b-value is adjusted to the changed duration, our abdominal results do however not show an impact on the diffusion time T on the monopolar signal attenuation, since already for very small b-values most of the monopolar signal has decayed.

Recently Cho *et al.* applied a flow compensated turbo spin echo sequence as an additional tool to characterize a flow phantom [70]. In this study the comparison between flow compensated and bipolar diffusion gradients reveals that for slow flow velocities the signal attenuation for bipolar gradients at high b-values is still affected by the flow. However their bipolar gradient scheme was twice refocused, while the flow compensated profile was only refocused once before the turbo spin echo readout. In the work at hand a monopolar gradient profile is chosen, such that timing for the different diffusion profiles can be chosen identically. The additional flow compensation of imaging gradients is however mentioned in neither of the mentioned publications.

7.2 Flow compensated IVIM

The question on the timescale of the incoherent motion was already raised in one of the first publications by Le Bihan [5]. While Le Bihan derives the substantially different signal attenuation curves for the limiting cases of very short and very long characteristic times, studies that use the IVIM model almost exclusively use the biexponential model, which is the limit of very short characteristic times.

Yamada et al. where the first to apply the biexponential model to abdominal diffusion weighted data. They did however not state any values for the obtained pseudo-diffusion coefficient D^* and state several values for D and f that differ from both out values, but also from other literature. For example the small diffusion coefficient of $D = 0.76 \pm 0.33$ for the pancreas is not in accordance with [46] and our value of 1.74 ± 0.17.

Luciani *et al.* found a decrease in D^* and in the apparent diffusion coefficient obtained by a monoexponential fit in cirrhotic liver. When comparing the stated values to our results for the healthy liver, we find our obtained value for $D = 1.211 \pm 0.064$ μm^2/ms in relative accordance with the stated $D = 1.10 \pm 0.7$. Our value for $f = 0.352 \pm 0.064$ is slightly higher, which might be explained by the flow-compensation of the imaging gradients, but might also be due to the longer echo times and the associated relaxation time effects [71]. The value of the pseudo-diffusion coefficient of $D^* = 79.1 \pm 18.1$ μm^2/ms stated in [6] is however, as expected much smaller than our value of 619 ± 91 μm^2/ms.

In another study by Lemke *et al.* [71] it was found that the perfusion fraction f could be used to distinguish healthy tissue from pancreatic cancer, furthermore Klauß *et al.* showed that the perfusion fraction could be used to distinguish between pancreatitis and pancreatic carcinoma [7]. Despite using the IVIM model, those two studies do not state any values for D^*. The stated values for D for healthy pancreas in [71] is given by $D = 1.13 \pm 0.15$ μm^2/ms, which is much smaller than the value obtained in this work by fitting the parabolic IVIM model, which yields $D = 1.74 \pm 0.17$ μm^2/ms. While the difference could be due to the different echo times, which were 60 ms in [71] and 120 ms in this work, it is possible that it also is a remnant of the use of the biexponential model in [71] .

A recent study by Andreou *et al.* [8] found poor measurement reproducibility of f and D^* in normal liver and metastases and comes to the conclusion that *efforts should be made to improve the measurement reproducibility of perfusion-sensitive IVIM parameters.* While there have been suggestions to use a fixed value for D^* [72], another approach is a bootstrapping algorithm to improve the quality of incoherent motion parameter maps [73].

Our findings that signal attenuation curves are different for flow compensated and monopolar gradients [38] is very important in this context, since it highlights, that the pseudo-diffusion limit of a very short characteristic timescale of the incoherent motion is not reached in typical diffusion experiments. The signal attenuation of the perfusion compartment can therefore not be described solely by D^*, but also needs to take into

account the characteristic timescale τ of the incoherent motion. While the D^* used in this work is defined identical to the original $D^* = \frac{\tau v^2}{6}$ [5], it is substantially different to the D^*-values, which are obtained from a biexponential fit. The finding that the pseudo-diffusion limit is not reached can explain the large variation of D^* values reported in literature [8], since the measured value depends on the chosen b-values and the exact sequence timing. Using the definition of D^* presented in this work has the advantage that the influence of the imaging parameters can be taken into account and that it is directly related to physiological parameters. The presented method allows furthermore to estimate the characteristic timescale of the incoherent motion.

For the *meandering* flow through packet spheres, Callaghan *et al.* investigated the timescale using a repetitive train of radio frequency pulses and interspersed gradient pulses of variable spacing [74]. Their approach to analyze flow and dispersion in porous media [75] can however not be translated to the IVIM problem. Based on our theoretical findings (section 4.4), the expected signal attenuation for a repetitive scheme, such as e.g. cosine gradients, would not only allow for lesser b-values than the flow compensated gradient scheme, but the signal attenuation due to incoherent flow would also be reduced. While the use of oscillating gradients to measure the incoherent motion was also considered in this work, it was found less suitable than flow compensated gradients, since the timescale of the incoherent motion found to be 184 ± 63 ms in pancreas and 156 ± 22 ms in liver is larger than the typical time of a diffusion experiment.

The oscillations predicted by our IVIM model for bipolar gradients and were reported in phantom experiments [76, 77], have however to the extent of our knowledge never been reported *in vivo*. The use of a parabolic velocity distribution as described in section 5.2.5 is necessary to reduce the existence of local minima in the residual of the used fit function and thus is an important step towards the creation of the parameter maps shown in [63]. The therein displayed maps for the microscopic IVIM parameters τ and D^* and the resulting velocity of the incoherent blood motion are the first maps of directly physiology-related IVIM parameters.

7.3 Denoising

The parameter maps obtained from pixel-wise fitting of the developed IVIM model appeared polluted by pseudo-random contributions. The influence on noise is a topic present in many areas of diffusion imaging, it is e.g. known to shift eigenvectors and increase eigenvalues in diffusion tensor imaging [78]. In the work at hand in particular the T-dependence of the flow compensated signal at very small b-values was found to be susceptible to noise and pulsation. The T-dependence of the flow compensated signal is however at the very core of the presented method and D^* and τ values cannot be determined meaningfully, if it cannot be resolved.

Therefore it was important to find a method to reduce those signal contributions.

Similar difficulties to estimate parameters in the biexponential IVIM model lead to the investigation of the effects of gradient polarity and breathing acquisition [42]. Also the reliability was assessed using fusion bootstrap moves [73]. To increase the SNR a joint reconstruction, estimating diffusion properties directly from the acquired k-space data was proposed [79].

The research related to signal recovery was boosted by the compressed sensing theory [80, 81] and in particular its applicability to MRI [82]. In the area of diffusion weighted MRI the use of a compressed sensing reconstruction allowed for accelerated diffusion spectrum imaging [83] and for a reliable reconstruction of high angular resolution diffusion imaging (HARDI) from only 16 diffusion-encoded scans using the sparsity of HARDI signals in the domain of spherical ridgelets [84].

To apply a compressed sensing reconstruction it is however necessary to find a sparse domain. Since no such domain was known *a priori* for the flow compensated and bipolar diffusion weighted signals, principal component analysis was performed. The IVIM parameter maps that were obtained from a data set to which a compressed sensing reconstruction was applied, were lesser impacted by noise (section 6.3.1). While the denoising properties of the applied algorithm is comparable to that of a 3×3 median filter, the smoothing effects are much less pronounced, since the used Karhunen-Loève transform is a pixel-wise operation. The obtained results could possibly be improved by choosing a more robust method to estimate the principal components [85]. Another possibility is the use of a dictionary based approach for magnetic resonance parameter mapping, as suggested by [86] which might not only allow one to tailor a sparsity transform to the model of incoherent motion, but also adjust the measurement protocol accordingly.

7.4 Summary

In the work at hand flow compensated intravoxel incoherent motion (IVIM) imaging is identified as a well-suited tool to probe the timescale of the microvasculature. A flow-compensated pulse sequence was developed, which has basically the same functionality as any diffusion sequence in clinical use, but allows to customize the diffusion gradients. The IVIM signal was found to depend on both the applied diffusion gradient profile and the total time T of the diffusion experiment. By developing a model to calculate the signal attenuation in case of incoherent motion it was possible to describe the experimental data and obtain parameter estimates for the characteristic timescale and velocity of the incoherent blood flow. A denoising algorithm based on principal component analysis was developed to reduce the amount of noise in the signal and obtain IVIM parameter maps from only 33% of the originally acquired data. This devopement makes the use of the flow compensated IVIM method in clinical trials feasible. By measuring the timescale of the incoherent motion, it is possible to reveal changes in microvasculature. Since the blood vessel supply of a tumor is critical to the admission of chemotherapeutics, flow compensated IVIM imaging is a new promising tool for oncologic imaging.

Bibliography

[1] D. Ma, V. Gulani, N. Seiberlich, K. Liu, J. L. Sunshine, J. L. Duerk and M. A. Griswold. Magnetic resonance fingerprinting. *Nature*, **495**, 187–192 (2013).

[2] M. E. Moseley, Y. Cohen, J. Mintorovitch, L. Chileuitt, H. Shimizu, J. Kucharczyk, M. F. Wndland and P. R. Weinstein. Early detection of regional cerebral-ischemia in cats - comparison of diffusion-weighted and T_2-weighted MRI and spectroscopy. *Magnetic Resonance in Medicine*, **14**, 330–346 (1990).

[3] A. R. Padhani, D.-M. Koh and D. J. Collins. Whole-Body Diffusion-weighted MR Imaging in Cancer: Current Status and Research Directions. *Radiology*, **261**, 700–718 (2011).

[4] D. Le Bihan, E. Breton, D. Lallemand, P. Grenier, E. Cabanis and M. Laval-Jeantet. MR Imaging of Intravoxel Incoherent Motions: Application to Diffusion and Perfusion in Neurologic Disorders. *Radiology*, **161**, 401–407 (1986).

[5] D. L. Bihan, E. Breton, D. Lallemand, M.-L. Aubin, J. Vignaud and M. Laval-Jeantet. Separation of Diffusion and Perfusion in Intravoxel Incoherent Motion MR Imaging. *Radiology*, **168**, 497–505 (1988).

[6] A. Luciani, A. Vignaud, M. Cavel, J. T. van Nhieu, A. Mallat, L. Ruel, A. Laurent, J.-F. Deux, P. Brugieres and A. Rahmouni. Liver Cirrhosis: Intravoxel Incoherent Motion MR Imaging-Pilot Study. *Radiology*, **249**, 891–899 (2008).

[7] M. Klauß, A. Lemke, K. Grünberg, D. Simon, T. J. Re, M. N. Wente, F. B. Laun, H.-U. Kauczor, S. Delorme, L. Grenacher and B. Stieltjes. Intravoxel Incoherent Motion MRI for the Differentiation Between Mass Forming Chronic Pancreatitis and Pancreatic Carcinoma. *Investigative Radiology*, **46**, 57–63 (2011).

[8] A. Andreou, D. M. Koh, D. J. Collins, M. Blackledge, T. Wallace, M. O. Leach and M. R. Orton. Measurement reproducibility of perfusion fraction and pseudodiffusion coefficient derived by intravoxel incoherent motion diffusion-weighted MR imaging in normal liver and metastases. *European Radiology*, **23**, 428–434 (2013).

[9] M. Bernstein, K. King and X. Zhou. *Handbook of MRI Pulse Sequences*, (Academic Press, 2004).

[10] F. Bloch. Nuclear induction. *Physical Review*, **70**, 460–474 (1946).

[11] P. M. Joseph, L. Axel and M. O'Donnell. Potential problems with selective pulses in NMR imaging systems. *Medical Physics*, **11**, 772–777 (1984).

[12] E. M. Haacke, R. W. Brown, M. R. Thompson and R. Venkatesan. *Magnetic resonance imaging physical principles and sequence design*, (Wiley-Liss, 1999).

[13] C. E. Shannon. Communication in the presence of Noise. *Proceedings of The Institute of Radio Engineers*, **37**, 10–21 (1949).

[14] M. Shinnar, S. Eleff, H. Subramanian and J. S. Leigh. The Synthesis of Pulse Sequences Yielding Arbitrary Magnetization Vectors. *Magnetic Resonance in Medicine*, **12**, 74–80 (1989).

[15] J. Pauly, P. L. Roux, D. Nishimura and A. Macovski. Parameter Relations for The Shinnar-Le Roux Selective Excitation Pulse Design Algorithm. *IEEE Transactions on Medical Imaging*, **10**, 53–65 (1991).

[16] E. L. Hahn. Spin echoes. *Physical Review*, **80**, 580–594 (1950).

[17] J. C. Maxwell. A dynamical theory of the electromagnetic field. *Philosophical Transactions of the Royal Society of London*, **155**, 459–512 (1865).

[18] M. A. Bernstein, X. J. Zhou, J. A. Polzin, K. F. King, A. Ganin, N. J. Pelc and G. H. Glover. Concomitant Gradient Terms in Phase Contrast MR: Analysis and Correction. *Magnetic Resonance in Medicine*.

[19] A. E. Fick. Ueber Diffusion. *Annalen der Physik*, **94**, 59–86 (1855).

[20] F. B. Laun. *Diffusionstensor - Magnetresonanztomographie: Phantomentwicklung und Optimierung der Messtechnik für Anwendungen am Rückenmark*. Ph.D. thesis, Ruprecht-Karls-Universität Heidelberg (2008).

[21] A. Einstein. Über die von der molekularkinetischen Theorie der Wärme geforderte Bewegung von in ruhenden Flüssigkeiten suspendierten Teilchen. *Annalen der Physik*, **322**, 549–560 (1905).

[22] H. C. Torrey. Bloch Equations with Diffusion Terms. *Physical Review*, **104**, 563–565 (1956).

[23] D. Le Bihan and P. J. Basser. *Diffusion and Perfusion Magnetic Resonance Imaging - Applications to Functional MRI*, chapter Molecular Diffusion and Nuclear Magnetic Resonance, pp. 8–9, (Raven Press 1995).

[24] M. E. Moseley, Y. Cohen, J. Kucharczyk, J. Mintorovitch, H. S. Asgari, M. F. Wndland, J. Tsuruda and D. Norman. Diffusion-weighted MR imaging of anisotropic water diffusion in cat central-nervous-system. *Radiology*, **176**, 439–445 (1990).

[25] A. Haase, J. Frahm, D. Matthaei, W. Hänicke and K.-D. Merboldt. FLASH Imaging. Rapid NMR Imaging Using Low Flip-Angle Pulses. *Journal of Magnetic Resonance*, **67**, 258–266 (1986).

[26] J. Frahm, A. Haase, D. Matthaei, W. Hänicke and K.-D. Merboldt. Method and device for rapid acquisition of spin resonance data for a space-resolved examination of an object. Patent DE3504734 (1986).

[27] O. Bieri, C. Ganter and K. Scheffler. On the Fluid-Tissue Contrast Behavior of High-Resolution Steady-State Sequences. *Magnetic Resonance in Medicine*, **68**, 1586–1592 (2012).

[28] P. Mansfield. Multi-planar image formation using NMR spin echoes. *Journal of Physics C-Solid State Physics*, **10**, L55–L58 (1977).

[29] C. Rank. *Entwicklung eines Flussphantoms zur Messung von Geschwindigkeits-Autokorrelationsfunktionen mit diffusionsgewichteter MRT*, bachelor thesis, Ruprecht-Karls-Universität Heidelberg.

[30] M. A. Griswold, P. M. Jakob, R. M. Heidemann, M. Nittka, V. Jellus, J. Wang, B. Kiefer and A. Haase. Generalized Autocalibrating Partially Parallel Aquisitions (GRAPPA). *Magnetic Resonance in Medicine*, **47**, 1202–1210 (2002).

[31] O. Heid. Eddy Current-Nulled Diffusion Weighting. In *8th Annual ISMRM Scientific Meeting and Exhibition*, p. 799 (2000).

[32] T. G. Reese, O. Heid, R. M. Weisskoff and V. J. Wedeen. Reduction of Eddy-Current-Induced Distortion in Diffusion MRI Using a Twice-Refocused Spin Echo. *Magnetic Resonance in Medicine*, **49**, 177–182 (2003).

[33] J. C. Gore, J. Xu, D. C. Colvin, T. E. Yankeelov, E. C. Parsons and M. D. Does. Characterization of tissue structure at varying length scales using temporal diffusion spectroscopy. *NMR in Biomedicine*, **23**, 745–756 (2010).

[34] J. Xu, M. D. Does and J. C. Gore. Sensitivity of MR Diffusion Measurements to Variations in Intracellular Structure: Effects of Nuclear Size. *Magnetic Resonance in Medicine*, **61**, 823–833 (2009).

[35] J. Xu, M. D. Does and J. C. Gore. Quantitative characterization of tissue microstructure with temporal diffusion spectroscopy. *Journal of Magnetic Resonance*, **200**, 189–197 (2009).

[36] J. Stepišnik. Analysis of NMR Self-Diffusion Measurements by a Density Matrix Calculation. *Physica*, **104B**, 350–364 (1981).

[37] R. P. Kennan, J.-H. Gao, J. Zhong and J. C. Gore. A general model of microcirculatory blood flow effects in gradient sensitized MRI. *Medical Physics*, **21**, 539–545 (1994).

[38] A. Wetscherek, B. Stieltjes, W. Semmler and F. B. Laun. Investigation of the Theoretical Background of the IVIM Model using Flow Compensated DWI. In *19th Annual ISMRM Scientific Meeting and Exhibition*, p. 2991 (2011).

[39] M. S. Zwanger, D. Porter, T. Feiweier, P. Heubes, T. G. Reese, T. Benner and J. E. Kirsch. Compensation for Maxwell Cross-Terms in Diffusion-Weighted Imaging. In *12th Annual ISMRM Scientific Meeting and Exhibition* (2004).

[40] M. Klauß, M. M. Gaida, A. Lemke, K. Grünberg, D. Simon, M. N. Wente, S. Delorme, H.-U. Kauczor, L. Grenacher and B. Stieltjes. Fibrosis and Pancreatic Lesions Counterintuitive Behavior of the Diffusion Imaging-Derived Structural Diffusion Coefficient D. *Investigative Radiology*, **48**, 129–133 (2013).

[41] T. Bäuerle, L. Seyler, M. Münter, A. Jensen, K. Brand, K. H. Fritzsche, A. Kopp-Schneider, M. Schüssler, H. P. Schlemmer, B. Stieltjes and M. Ganten. Diffusion-weighted imaging in rectal carcinoma patients without and after chemoradiotherapy: A comparative study with histology. *European Journal of Radiology*, **82**, 444–452 (2013).

[42] H. A. Dyvorne, N. Galea, T. Nevers, M. I. Fiel, D. Carpenter, E. Wong, M. Orton, A. de Oliveira, T. Feiweier, M.-L. Vachon, J. S. Babb and B. Taouli. Diffusion-weighted Imaging of the Liver with Multiple b Values: Effect of Diffusion Gradient Polarity and Breathin Acquisition on Image Quality and Intravoxel Incoherent Motion Parameters – A Pilot Study. *Radiology*, **266**, 920–929 (2013).

[43] A. Wetscherek, B. Stieltjes, W. Semmler and F. B. Laun. Flow Compensated IVIM as a Tool to Probe Microvasculature. In *20th Annual ISMRM Scientific Meeting and Exhibition*, p. 2012 (2012).

[44] G. J. Stanisz, J. G. Li, G. A. Wright and R. M. Henkelman. Water Dynamics in Human Blood via Combined Measurements of T_2 Relaxation and Diffusion in the Presence of Gadolinium. *Magnetic Resonance in Medicine*, **39**, 223–233 (1998).

[45] J. G. Li, G. J. Stanisz and R. M. Henkelman. Integrated Analysis of Diffusion and Relaxation of Water in Blood. *Magnetic Resonance in Medicine*, **40**, 79–88 (1998).

[46] A. Lemke, F. B. Laun, D. Simon, B. Stieltjes and L. R. Schad. An In Vivo Verification of the Intravoxel Incoherent Motion Effect in Diffusion-Weighted Imaging of the Abdomen. *Magnetic Resonance in Medicine*, **64**, 1580–1585 (2010).

[47] E. O. Stejskal and J. E. Tanner. Spin Diffusion Measurements: Spin Echoes in the Presence of a Time-Dependent Field Gradient. *The Journal of Chemical Physics*, **42**, 288–292 (1965).

[48] J. H. Maki, J. R. MacFall and G. A. Johnson. The Use of Gradient Flow Compensation to Separate Diffusion and Microcirculatory Flow in MRI. *Magnetic Resonance in Medicine*, **17**, 95–107 (1991).

[49] O. P. Simonetti, R. E. Wendt and J. L. Duerk. Significance of the Point of Expansion in Interpretation of Gradient Moments and Motion Sensitivity. *Journal of Magnetic Resonance Imaging*, **1**, 569–577 (1991).

[50] G. Steidle, F. Eibofner and F. Schick. Quantitative Diffusion Imaging of Adipose Tissue in the Human Lower Leg at 1.5 T. *Magnetic Resonance in Medicine*, **65**, 1119–1125 (2011).

[51] D. S. Grebenkov. NMR survey of reflected Brownian motion. *Reviews of Modern Physics*, **79**, 1077–1137 (2007).

[52] D. S. Grebenkov. Laplacian Eigenfunctions in NMR. I. A Numerical Tool. *Concepts in Magnetic Resonance Part A*, **32A**, 277–301 (2008).

[53] D. S. Grebenkov. Laplacian Eigenfunctions in NMR. II. Theoretical Advances. *Concepts in Magnetic Resonance Part A*, **34A**, 264–296 (2009).

[54] R. M. Henkelman, J. J. Neil and Q.-S. Xiang. A Quantitative Interpretation of IVIM Measurements of Vascular Perfusion in the Rat Brain. *Magnetic Resonance in Medicine*, **32**, 464–469 (1994).

[55] B. M. Fenton and B. W. Zweifach. Microcirculatory model relating geometrical variation to changes in pressure and flow rate. *Annals of Biomedical Engineering*, **9**, 303–321 (1981).

[56] D. A. McDonald. *Blood Flow in Arteries*, (Edward Arnold Publishers Ltd, 1960).

[57] J. J. Bishop, P. R. Nance, A. S. Popel, M. INtaglietta and P. C. Johnson. Effect of erythrocyte aggregation on velocity profiles in venules. *American Journal of Physiology-Heart and Circulatory Physiology*, **280**, H222–H236 (2001).

[58] K. Pearson. On lines and planes of closest fit to systems of points in space. *Philosophical Magazine*, **2**, 559–572 (1901).

[59] H. Gudbjartsson and S. Patz. The Rician Distribution of Noisy MRI Data. *Magnetic Resonance in Medicine*, **34**, 910–914 (1995).

[60] S. Becker, E. J. Candès and M. Grant. Templates for Convex Cone Problems with Applications to Sparse Signal Recovery. *Mathematical Programming Computation*, **3**, 165–218 (2010).

[61] E. van den Berg and M. P. Friedlander. Probing the Pareto Frontier For Basis Pursuit Solutions. *SIAM Journal on Scientific Computing*, **31**, 890–912 (2008).

[62] E. van den Berg and M. P. Friedlander. SPGL1: A solver for large-scale sparse reconstruction (2007). http://www.cs.ubc.ca/labs/scl/spgl1.

[63] A. Wetscherek, F. B. Laun, C. Prieto and C. Tejos. Compressed Sensing for Flow-Compensated Intra-Voxel Incoherent Motion Modeling. In *21th Annual ISMRM Scientific Meeting and Exhibition*, p. 3111 (2013).

[64] Y. P. Du, X. J. Zhou and M. A. Bernstein. Correction of Concomitant Magnetic Field-Induced Image Artifacts in Nonaxial Echo-Planar Imaging. *Magnetic Resonance in Medicine*, **48**, 509–515 (2002).

[65] J. Janke, A. Wetscherek, B. Stieltjes and F. B. Laun. Compressed Sensing for Flow-Compensated Intra-Voxel Incoherent Motion Modeling. In *21th Annual ISMRM Scientific Meeting and Exhibition*, p. 3079 (2013).

[66] L. Müller, J. Janke, A. Wetscherek, M. Bach, B. Stieltjes and F. B. Laun. Gemessene Austauschraten in zellulären Lösungen mittels doppelt diffusionsgewichteter MR-Bildgebung, *submitted for presentation at 44. Jahrestagung der Deutschen Gesellschaft für Medizinische Physik* (2013).

[67] C. B. Ahn, S. Y. Lee, O. Nalcioglu and Z. H. Cho. The effects of random directional distributed flow in nuclear magnetic resonance imaging. *Medical Physics*, **14**, 43–48 (1987).

[68] D. Harpen. Comments on "The effects of random directional distributed flow in nuclear magnetic resonance imaging". *Medical Physics*, **14**, 1092 (1987).

[69] J. H. Maki, H. Benveniste, J. R. MacFall and G. A. Johnson. Maximization of Contrast-to-Noise Ratio to Distinguish Diffusion and Microcirculatory Flow. *Journal of Magnetic Resonance Imaging*, **1**, 39–46 (1991).

[70] G. Y. Cho, S. Kim, J. H. Jensen, P. Storey, D. K. Sodickson and E. E. Sigmund. A Versatile Flow Phantom for Intravoxel Incoherent Motion MRI. *Magnetic Resonance in Medicine*, **67**, 1710–1720 (2012).

[71] A. Lemke, F. B. Laun, M. Klauß, T. J. Re, D. Simon, S. Delorme, L. R. Schad and B. Stieltjes. Differentiation of Pancreas Carcinoma From Healthy Pancreatic tissue Using Multiple *b*-Values. *Investigative Radiology*, **44**, 769–775 (2009).

[72] A. Lemke, F. B. Laun, L. R. Schad and B. Stieltjes. Towards an Optimal Distribution of B-Values for IVIM Imaging. In *18th Annual ISMRM Scientific Meeting and Exhibition*, p. 1750 (2010).

[73] M. Freiman, J. M. Perez-Rossello, M. J. Callahan, S. D. Voss, K. Ecklund, R. V. Mulkern and S. K. Warfield. Reliable estimation of incoherent motion parametric maps from diffusion-weighted MRI using fusion bootstrap moves. *Medical Image Analysis*, **17**, 325–336 (2013).

[74] P. T. Callaghan and S. L. Codd. Flow coherence in a bead pack observed using frequency domain modulated gradient nuclear magnetic resonance. *Physics of Fluids*, **13**, 421–427 (2001).

[75] J. D. Seymour and P. T. Callaghan. Generalized approach to NMR analysis of flow and dispersion in porous media. *AIChE Journal*, **43**, 2096–2111 (1997).

[76] J. D. Seymour and P. T. Callaghan. "Flow-Diffraction" Structural Characterization and Measurement of Hydrodynamic Dispersion in Porous Media by PGSE NMR. *Journal of Magnetic Resonance, Series A*, **122**, 90–93 (1996).

[77] G. Y. Cho, D. K. Sodickson and E. E. Sigmund. Characterization of the TE Dependence of IVIM Biomarkers in a Flow Phantom and *In Vivo*. In *20th Annual ISMRM Scientific Meeting and Exhibition*, p. 3977 (2012).

[78] F. B. Laun, L. R. Schad, J. Klein and B. Stieltjes. How background noise shifts eigenvectors and increases eigenvalues in DTI. *Magnetic Resonance Materials in Physics Biology and Medicine*, **22**, 151–158 (2009).

[79] J. P. Haldar, V. J. Wedeen, M. Nezanmzadeh, G. Dai, M. W. Weiner, N. Schuff and Z.-P. Liang. Improved Diffusion Imaging Through SNR-Enhancing Joint Reconstruction. *Magnetic Resonance in Medicine*, **69**, 277–289 (2013).

[80] E. J. Candès, J. Romberg and T. Tao. Robust uncertainty principles: Exact signal reconstruction from highly incomplete frequency information. *IEEE Transactions on information Theory*, **52**, 489–509 (2006).

[81] D. Donoho. Compressed sensing. *IEEE Transactions on Information Theory*, **52**, 1289–1306 (2006).

[82] M. Lustig, D. Donoho and J. M. Pauly. Sparse MRI: The application of compressed sensing for rapid MR imaging. *Magnetic Resonance in Medicine*, **58**, 1182–1195 (2007).

[83] M. I. Menzel, E. T. Tan, K. Khare, J. I. Sperl, K. F. King, X. Tao, C. J. Hardy and L. Marinelli. Accelerated diffusion spectrum imaging in the human brain using compressed sensing. *Magnetic Resonance in Medicine*, **66**, 1226–1233 (2011).

[84] O. Michailovich, Y. Rathi and S. Dolui. Spatially Regularized Compressed Sensing for High Angular Resolution Diffuion Imaging. *IEEE Transactions on Medical Imaging*, **30**, 1100–1115 (2011).

[85] E. J. Candès, X. Li, Y. Ma and J. Wright. Robust Principal Component Analysis? *Journal of the ACM*, **58**, 11:1–11:37 (2011).

[86] M. Doneva, P. Börnert, H. Eggers, C. Stehning, J. Sénégas and A. Mertins. Compressed Sensing reconstruction for Magnetic resonance Parameter Mapping. *Magnetic Resonance in Medicine*, **64**, 1114–1120 (2010).

Danksagung

Ich danke Prof. Semmler für die Möglichkeit, in der Abteilung Medizinische Physik in der Radiologie mein Promotionsvorhaben durchführen zu können.

Außerdem sei Prof. Oelfke zu nennen, bei dem ich mich für die Vertretung der Arbeit gegenüber der Fakultät und die Betreuung im Thesis Advisory Comittee bedanken möchte. Im Nachbarzimmer war er stets eine Anlaufstelle bei aufkommenden Fragen.

Bei Prof. Schad möchte ich mich für die Möglichkeit bedanken, am Tierscanner Messungen durchführen zu können.

Frau Prof. Heiland danke ich für die wertvollen Diskussionen, die sich bei den regelmäßigen Projekttreffen ergaben.

Ein besonders großer Dank geht an Dr. Frederik Laun für die Betreuung der Arbeit. Er war stets ein kompetenter Ansprechpartner bei wissenschaftlichen Fragestellungen, auf den man auch in Extremsituationen zählen konnte. Ihm und Tine danke ich auch für die Unterstützung bei der Wohnungssuche kurz vor Weihnachten.

I would like to thank the group of the Centro des Imágenes Biomedicas for the warm welcome during my stay in Santiago. Apart from Prof. Cristián Tejos who supervised the work on the denoising algorithm, I would like to thank Prof. Claudia Prieto from King's College London for the fruitful Skype discussions and Michael Santoro, who shared my fate of neither understanding the Chilean people, nor their language.

Auch bei unserer Sekretärin Frau Fritz möchte ich mich bedanken. Sie weiß bei fast allen Fragen fast immer eine Lösung.

Meinen Bürokollegen Michael, Jessica, Jutta, Lars, Armir, Christian und Boris danke ich für die gute Atmosphäre und die hilfreichen Diskussionen bei spontan auftretenden Fragen und den unermüdlichen Einsatz bei spontan auftretenden Probandenmessungen jeder Art. Bezüglich letzterem Punkt seien auch Tristan, Anja und Dione zu nennen.

Außerdem danke ich See, Betti und Agatha dafür, dass sie die Anreise aus dem schönen Würzburg auf sich genommen haben, um eine Ganzkörpermassage mit Diffusionsgradienten über sich ergehen zu lassen.

Zuletzt möchte ich mich bei meinen Eltern bedanken, die immer eine große Hilfestellung waren und mich, wo es Ihnen möglich war, unterstützt haben. Gleiches gibt für meine Schwester Kerstin und den And. Fettes Dankeschön!